Downloaded from orbit.dtu.dk on: May 05, 2023

DTU Library

Technology for Polymer Optical Fiber Bragg Grating Fabrication and Interrogation.

Ganziy, Denis

Publication date:
2017

Document Version
Publisher's PDF, also known as Version of record

Link back to DTU Orbit

Citation (APA):
Ganziy, D. (2017). *Technology for Polymer Optical Fiber Bragg Grating Fabrication and Interrogation.* DTU Fotonik.

General rights
Copyright and moral rights for the publications made accessible in the public portal are retained by the authors and/or other copyright owners and it is a condition of accessing publications that users recognise and abide by the legal requirements associated with these rights.

- Users may download and print one copy of any publication from the public portal for the purpose of private study or research.
- You may not further distribute the material or use it for any profit-making activity or commercial gain
- You may freely distribute the URL identifying the publication in the public portal

If you believe that this document breaches copyright please contact us providing details, and we will remove access to the work immediately and investigate your claim.

Technology for Polymer Optical Fiber Bragg Grating Fabrication and Interrogation

Denis Ganziy

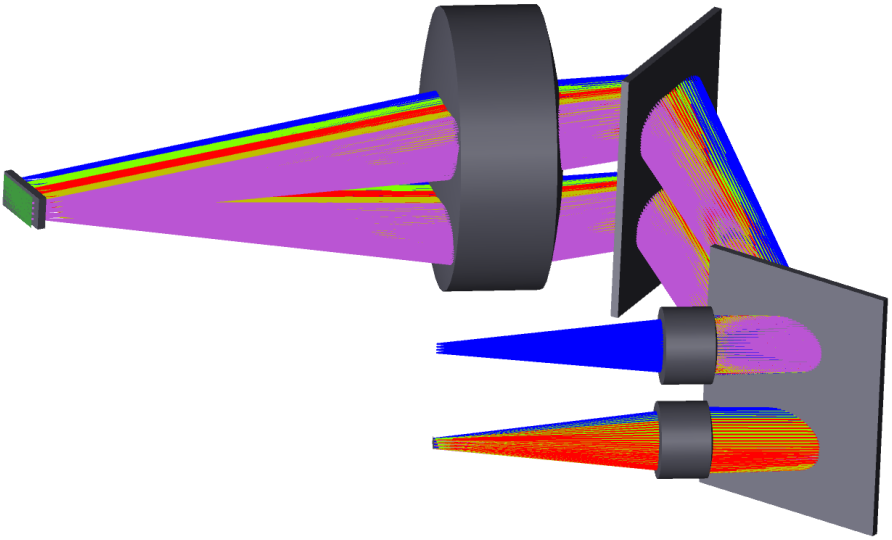

Ph.D. Thesis

February 2017

DTU Fotonik
Department of Photonics Engineering

TRIPOD

DTU

Ibsen photonics

Preface

This thesis is submitted for the degree of Doctor of Philosophy to the Technical University of Denmark. This PhD-project was prepared by the author between March 2014 and February 2017. The project received funding from the People Programme (Marie Curie Actions) of the European Union's Seventh Framework Programme FP7/2007-2013/under REA grant agreement n° 608382.

The supervisors were:

- Prof. Dr. Ole Bang, Department of Photonics Engineering, Technical University of Denmark, Kgs. Lyngby, Denmark
- Dr. Bjarke Rose, Ibsen Photonics A/S, Ryttermarken 15-21, Farum, Denmark

The PhD-project also included two weeks of external research stays, one week each at Cyprus University of Technology, Limassol, Cyprus, and Aston Institute of Photonic Technology, Birmingham, UK, respectively.

The goal of the project was to advance the technology of POFBG sensing. More precisely, the project was to develop a new interrogator for POFBG sensing, which combines cost-effectiveness with high performance and resolution. The majority of the work was carried out at Ibsen Photonics A/S in Farum in period between March 2014 and February 2017, where the work was focused on developing and testing a new interrogator.

Zemax Optic Studio has been used to develop optical design of the interrogator and analyze the performance. The evaluation software has been written in LabView, which has also been used for the analysis and

data processing. Microsoft Visual Studio has been used for C++ code compiling and building Hadamard decoding dll. Citations are indicated by number and the full list of citations is positioned in the last section of the thesis. All Figures are made by the author unless otherwise stated. Furthermore, a list of abbreviations is located after the conclusion.

February 28th, 2017
Denis Ganziy

Acknowledgments

I would like to thank all my supervisors and colleagues for the support, guidance and knowledge sharing: without you this work would have been impossible. Special thanks to my supervisor Dr. Bjarke Rose from Ibsen Photonics for accepting me to this project and dealing with me daily. His advice and sharp eyes significantly influenced this work and my professional skills. He has also been a role model all these three years.

I would like to give my deep thanks to my academic supervisor Prof. Dr. Ole Bang for his scientific approach and great advice. He showed me how a research paper should be written. This helped me a lot when I wrote the thesis.

I wish to thanks all my colleagues and friends at Ibsen Photonics. It was a great pleasure to work with them all these years and I am happy that I will have future in this exciting environment. I am especially grateful to Henrik Skov Andersen for his care and support when I needed it, he always had time in his very busy schedule to answer my questions and helped me in difficult work and private situations. I would also like to thank my colleagues from the “Spectro R&D” team. Thanks to Ole Jespersen for teaching me LabView and for all these fruitful talks about science and technology we have had. Special thanks to Poul Hansen for making the mechanical design of the interrogator. Many thanks to Michael Rasmussen for showing and teaching me Zemax, now I have one more professional passion in my life! Thanks to

Nikolai Herholdt-Rasmussen for his advice and help in the prototype assembling and testing.

I also would like to thank all the people from the TRIPOD project for making this research became true. I will definitely miss our meetings and the great time we had together. Special thanks to Hafeez Ul Hassan for his sarcastic sense of humor and establishing the Danish branch of Leffe Fan Club.

I would like to thank my family, my mother Galina and my father Alexandr. Without their support during these years I was not able to finish my project. Finally, I would like to thank my beautiful wife Elena for existing in my life, I am enjoying every single moment being with you!

Abstract

The aim of this project is to develop a new, high-quality interrogator for FBG sensor systems, which combines high performance with cost-effectiveness. The work includes the fields of optical system design, signal processing, and algorithm investigation. We present an efficient and fast peak detection algorithm for FBGs, which avoids sudden shifts in the fitted wavelength and improves the wavelength fit resolution. We evaluate how detrimental the influence of higher-order modes is to the polarization stability and linearity of the strain and temperature response of a few-mode FBG sensor. We analyze and investigate errors and drawbacks, which are typical for spectrometer-based interrogators: undersampling, grating internal reflection, photo response non-uniformity, pixel crosstalk and temperature and long term drift. We propose a novel type of multichannel Digital Micromirror Device (DMD) based interrogator, where the linear detector is replaced with a commercially available DMD, which leads to cost reduction and better performance. Original optical design, which utilizes advantages of a retro-reflect optical scheme, has been developed in Zemax. We test the presented interrogator by measuring optical resolution, wavelength fit resolution, accuracy, temperature and polarization dependable wavelength shift and use it to measure the strain response of a few-mode and a highly multimode FBG in a polymer fiber.

Résumé (In Danish)

Formålet med dette projekt er at udvikle en ny, høj- kvalitets interrogator for FBG sensorsystemer, som kombinerer høj ydeevne med omkostningseffektivitet. Arbejdet omfatter områderne optisk system design, signalbehandling, og algoritme udvikling. Vi præsenterer en effektiv og hurtig detektionsalgoritme for FBGere, som undgår pludselige skift i den fittede bølgelængde og forbedrer bølgelængde-fit opløsningen. Vi vurderer den begrænsende effekt som højere orden modes har på polarisations-stabiliteten og på linearitetet af strain- og temperatur-responset af en few-mode FBG sensor. Vi analyserer og undersøger fejl og ulemper, som er typiske for spektrometer-baserede interrogatorer: undersampling, interne grating refleksioner, fotoresponse ikke-uniformitet, pixel krydstale og temperatur- og langtidsdrift. Vi foreslår en ny type multikanals Digital Micromirror Device (DMD) baseret interrogator med reduceret omkostning og forbedret ydeevne, hvor den lineære detektor er erstattet med en kommercielt tilgængelig DMD. Et originalt optisk design, der udnytter fordelene ved en retroreflektiv optisk geometri, er blevet udviklet i Zemax. Vi tester den præsenterede interrogator for optisk opløsning, bølgelængde fit opløsning, nøjagtighed, temperatur- og polariserations-bølgelængde drift, og anvender den til at måle stresrespons på en FBG med få modes og en stærkt multimode FBG i en polymer fiber.

Contents

List of Publications

Journal publications

1. **D. Ganziy**, O. Jespersen. G. Woyessa, B. Rose, O. Bang, "*Dynamic gate algorithm for multimode fiber Bragg grating sensor systems,*" Applied Optics **54(18)**, 5657-5661 (2015).
2. **D. Ganziy**, B. Rose, O Bang, "*Performance of low-cost few-mode FBG sensor systems: polarization sensitivity and linearity of temperature and strain response,*" Applied Optics **55(23)**, 6156-6161 (2016).
3. **D. Ganziy**, B. Rose, O Bang, "*Compact multichannel high resolution MEMS based interrogator for FBG sensing,*" Applied Optics 55(12), 3622-3627 (2017).

Conference contributions

1. **D. Ganziy**, O. Jespersen, B. Rose, O Bang, "An efficient and fast detection algorithm for multimode FBG sensing", OFS-24, 24th International Conference on Optical Fiber Sensors, Curitiba, Brazil, Sep. 28 – Oct. 2, 2015, Proc. of SPIE Vol. 9634 963445-1. doi: 10.1117/12.2194305
2. **D. Ganziy**, O. Jespersen, B. Rose, O Bang, "Robust and accurate algorithm for multimode polymer optical FBG sensor system", POF 2015, 24th International Conference on Plastic Optical Fibers, Sep. 22-24, Nürnberg, Germany (Oral presentation).
3. A. Lacraz, **D. Ganziy**, B. Rose, O. Bang, K. Kalli, "Strain and temperature characterization of femtosecond laser-inscribed FBGs in CYTOP gradient index polymer optical fibre", SPIE Photonics Europe Symposium, 3rd – 7th April 2016, Brussels, Belgium
4. **D. Ganziy**, O. Jespersen, B. Rose, O Bang, "Multichannel spectrometer based interrogator for FBG sensing", POF 2016, 25th International Conference on Plastic Optical Fibers, Sep. 13-15, Birmingham, UK (poster presentation).

Chapter 1

Introduction

Optical fiber can proudly be considered as one of the greatest inventions of the twentieth century. Every day these tiny hair-thin devices carry tremendous quantities of information from place to place, making our dreams come true. Together with the development of the laser and laser diode, an optical fiber formed the basis of the telecommunications revolution of the late 20th century and provided the infrastructure for the internet. This was made possible by some of the important properties of optical fibers, such as huge information-carrying capacity (high bandwidth), low cost, low maintenance, low attenuation, immunity from the many disturbances that can affect electrical wires and wireless communication links. The digital revolution started in the late 20th century now continues with mobile usage and internet access growing massively. That is why for most of the general public, an optical fiber has become a synonym of modern telecommunication and fast broadband internet. However, optical fiber technology has also made a significant contribution to sensing technology. Even though fiber sensors were initially laboratory curiosities and simple proof-of-concept demonstrations, the rapid progress in the development of optical fiber technology has resulted in a high increase of fiber optic sensor research and applications over the last 20 years. The reason for this lies in important characteristics and intrinsic properties of optical fibre sensors, such as immunity to

electromagnetic interference, which means that they can be used in places where high voltage electricity occurs; light weight and relatively small size, which allows the fibre optical sensor to be made compact and portable; flexibility allowing the sensor to be placed in the tightest spaces; and high multiplexing capabilities, which facilitates deployment of large sensor networks. Thanks to these features, fiber optical sensors are widely used nowadays in civil engineering, aerospace, oil and gas, marine, smart structures, bio-medical devices, electric power industry, and many others. Many different sensor types based on different technologies have been developed, including distributed sensors based on Raman and Brillouin scattering, sensors based on Fabry-Perot cavities and, of course, Fibre Bragg Gratings (FBGs) – the central subject of this work.

An FBG can be considered as a tunable mirror or a wavelength filter in an optical fiber, which reflects a certain wavelength or, to be more precise, a certain bandwidth of light, and transmits all others. Of course, this model doesn't describe all properties of FBGs, which will be done in the next chapter, but nevertheless, it is very simple and very useful for the general public. It has been shown that the reflected wavelength has a good linear response to variations in temperature, strain, and pressure [1]. It has also been demonstrated that FBG sensors can be used for probing other types of measurand such as erosion, liquid, chemicals, bending and magnetic fields [2]. The key feature is that the measurand information is wavelength encoded, meaning that the FBG based sensor is self-referenced and independent of fluctuating signal levels, source power and connector losses that afflict many other types of optical sensors. In combination with low weight, low price, and immunity to electromagnetic interference, this makes the FBG a very attractive piece of technology for sensing purposes.

Since first commercially available telecom fibers were made from silica, the first FBGs were also inscribed in silica fibers. Silica-based FBGs have become widely known, researched and popular over the recent 20 years. Even though silica has shown itself as a very good material for optical fiber technology, it sets some limitations to silica-based fiber Bragg gratings, for example, the sensing strain range is

limited to a few percent. This and other imperfections have spurred an interest in FBG based sensors fabricated in polymer optical fibers. In comparison with silica-based FBGs, polymer fiber sensors offer increased stress sensitivity and a larger strain range [3, 4]. Since some polymers are sensitive to water, polymer FBGs can also be used as humidity sensors. Due to much lower Young's modules, polymer based FBGs perturb the behavior of the measured structure less than the much stiffer silica fiber and, thus, can be embedded in very elastic and soft materials, like fabric, nylon etc. Considering safety of use, like consequences of a fiber breakage, polymer fiber sensors may be more attractive for in-vivo medical sensing applications. The advantages of polymer FBG sensors over silica FBGs listed above indicate that polymer FBGs have a potential for use in a range of applications where the material properties of the used polymer give advantages over silica.

The core of each fiber Bragg grating sensor system is, of course, a fiber Bragg grating. However, the FBG itself doesn't show the measured value and, consequently, it is necessary to use a special device, often called an interrogator, to decode the wavelength encoded measurand. The interrogator usually measures the Bragg wavelength shift, which is then converted to measurand data (f. ex. strain, temperature, pressure etc.). Performance of each instrument is always limited by the performance of the weakest link, which can often be an interrogator in a case of the FBG sensor system. Interrogator parameters like resolution, speed, accuracy, and linearity can significantly influence sensor performance, for example, to resolve a temperature and strain change of ~0.1 °C and 1 με a wavelength resolution of 1 pm is required. But not only technical specifications are important. Low price, robustness, and durability should also be considered, since it strongly impacts on how a sensor system can be used outside a laboratory by the end-consumer.

1.1 Scope

This PhD project is part of the EU Marie Curie Initial Training Network (ITN) TRIPOD (Training & Research involving Polymer Optical Devices). The aim of TRIPOD is to significantly extend the

range of applications of optical fiber grating sensors by developing a mature version of the technology in polymer optical fibers (POF). When the TRIPOD project plan was submitted the main objectives of my part of the project were to develop phase masks and FBG interrogator suitable for polymer FBG sensing. However, it turned out that the current technology of phase mask production worked well and phase-masks for inscribing 650 and 850 nm FBGs in POF had already been produced by Ibsen Photonics and successfully used by other TRIPOD partners.

In this work I will, therefore, focus on developing a new high-quality interrogator for FBG sensor systems. The whole R&D work can be divided into three main parts:

1. investigation of using multimode fiber Bragg gratings, since almost all of commercially available POFs are multimode
2. improvement of the single channel interrogator, which is currently state of the art on the market
3. developing a new high performance and cost-effective interrogator

The following investigations and developments are targeted for the first part:

- comparison between single-mode and multimode FBG sensor system
- development of a new fitting algorithm, which can handle multimode FBG reflected spectra

The second part requires the following steps:

- determination and investigation of typical errors for spectrometer-based interrogators
- comparison between different peak-fitting algorithms and their influence on the resolution
- improvements in the optical detection channel to increase resolution and accuracy

The third part is the main part and consists of the following steps:

- development of optical design of the new interrogator
- new software algorithms for more precise peak detection
- characterization and test of the new interrogator

1.2 Outline

Chapter 2 provides a brief introduction to FBG sensing, starting with a short theory of FBGs and an overview of known interrogation techniques.

Chapter 3 is dedicated to polymer optical fiber Bragg gratings from a historical perspective, FBG inscription techniques and comparison of polymer FBGs with glass FBGs. It continues with the latest progress in the polymer FBG field.

Chapter 4 presents a novel wavelength detection algorithm (Dynamic Gate Algorithm) for FBG sensing. It is shown how the new algorithm together with a "Peak tracking" option can fit and track arbitrary changing multimode peaks in real-time.

Chapter 5 starts with an investigation and detailed comparison between few-mode and single-mode FBG performance. It shows the effect of the high order modes on the FBG sensor linearity and polarization stability.

Chapter 6 is dedicated to an investigation of errors, which are typical for spectrometer based interrogators: undersampling, grating internal reflection, photo response non-uniformity, pixel crosstalk, temperature and long term drift. Several solutions are also proposed here (wedges, abs. calibration).

Chapter 7 is dedicated to the new interrogator. It starts with brief information about digital micromirror devices (DMDs) and applications. It describes in detail the architecture and principle of the new interrogator, based on a DMD. It provides optical and mechanical design and continues with a detailed description of the device, including software and scanning methods.

Chapter 8 presents a practical evaluation of the new interrogator. It starts with in-lab tests and measurements, which include a measure of the most important properties and characteristics of an interrogator: optical resolution, wavelength fit resolution, accuracy, temperature, and polarization wavelength shift, and measurement frequency. It

continues with strain and temperature measurements of real FBG sensors, including FBGs in multimode fibers.

Conclusion and final remarks are in Chapter 9.

Chapter 2

FBG Sensing and Interrogation

This chapter is dedicated to a general description of FBG sensing principles and interrogation techniques, including a short theory of fiber Bragg gratings.

2.1 Historical perspective

The history of fiber Bragg gratings started in 1978 when Ken Hill and coworkers at the Communication Research Center in Canada first observed fiber photosensitivity [5]. During an experiment they launched visible light from argon ion laser into the core of the fiber and that led to an increase in the fiber attenuation. They found that the 488 nm laser light launched into the fiber core interfered with the Fresnel reflected beam and formed a standing wave pattern in the core. The index of refraction in the photosensitive fiber core was changed permanently at the high –intensity points. Since a refractive index perturbation had the same spatial periodicity as the interference pattern such kind of grating reflected only light at the writing wavelength. These gratings were subsequently called Hill gratings. Even though these gratings were even used to measure strain and temperature they were very long with extremely narrow bandwidth

and they reflected only the light which was used to fabricate them (488 nm), which means high losses at the sensed wavelength. All these factors unfortunately limited practical application of self-induced gratings in sensing.

A new era began in 1989 when the side-writing technique was first demonstrated by Gerry Meltz and colleagues from the United Technologies Research Center. They used a bulk optic interferometer to directly write gratings into the fiber using side illumination with a UV laser [6]. This method completely turned fiber Bragg gratings from a scientific curiosity to a mainstream tool. The key advantage was that by changing the angle between the intersecting beams and, thus, changing the spacing between the interference maxima, one could change the periodicity of the grating and, as a consequence, reflected wavelength. Ability to reflect at any wavelength independent of the writing wavelength made possible to use FBGs in modern telecommunication and sensor systems. However, there were several issues, which still set limits on the use of FBGs in the real life applications. The holographic technique used by Meltz and colleagues had few disadvantages: 1) extremely high sensitivity to mechanical vibrations – submicron displacement of interferometer components causes fringe pattern to drift and washing out the grating from the fibre; 2) extremely high requirements to the environment – even air current may have a significant impact by locally changing the refractive index; 3) laser source should have good spatial and temporal coherence and excellent wavelength and output power stability for quality gratings production. Thus, substantial amount of time and effort was required to produce a big batch of high-quality FBGs those days.

The next breakthrough took place in 1993 when two important technologies were presented: the phase-mask technique and hydrogen-loading. One of the first experiments using the phase-mask was carried out by Hill and coworkers [7]. The phase-mask technique, as appeared afterward, became one of the most effective methods for inscribing Bragg gratings. The method uses a diffractive optical element (the phase mask) to spatially modulate the UV writing beam and, thus, produce an interference pattern with a desired periodicity to print an

FBG in a fiber. The phase-mask technique successfully overcame the drawback of the previous holographic method and made a tremendous impact on the field. The main advantage was in the reduction of the complexity of the fabrication system. The use of only one optical element greatly increased robustness and stability of the method. Due to the fact that the fiber can be placed very close to the phase-mask in the near field of interfered UV beams, the only spatial coherence of the order of a few tens of microns is required. This also minimized sensitivity to mechanical vibrations. The second key development was the process of hydrogenation of fibers prior to the UV exposure, which led to an extremely high enhancement of the photosensitivity of the fibers to UV light [8]. Grating modulation amplitudes of ~10^{-2} were reached instead of ~10^{-2} before without hydrogen. This significant improvement by two orders of magnitude allowed to produce strong grating with high reflectivity and decrease the grating exposure times.

Many further improvements and developments in grating fabrication process took place in the next decade, which includes the invention of photosensitive fibers, i.e. fibers with dopant materials; so-called Type II gratings, obtained by an optical damage process when the UV light was pulsed with high peak intensity. Such kind of gratings can be fabricated by a single high power pulse during drawing process and often so-called “draw tower” gratings. These gratings are extremely stable thermally, due to the fusion of the glass matrix. Several different types of gratings were also developed that time, including long period gratings (LPG), chirped gratings, tilted fiber Bragg grating, fiber Bragg gratings inscribed in microstructured fibers.

Finally, in 2000’s fiber Bragg gratings in polymer optical fibers were demonstrated, that opened up new sensing methods and applications. Polymer optical fiber Bragg gratings (POFBG) will be discussed later in the next chapter.

2.2 Principle of operation

In its simplest model fiber Bragg grating can be considered as a wavelength filter, which reflects a certain bandwidth of light (wavelength) and transmits all others. In this model refractive index in

the fiber core is periodically modulated with a constant period and the phase fronts are perpendicular to the fiber's longitudinal axis (Fig. 2.1).

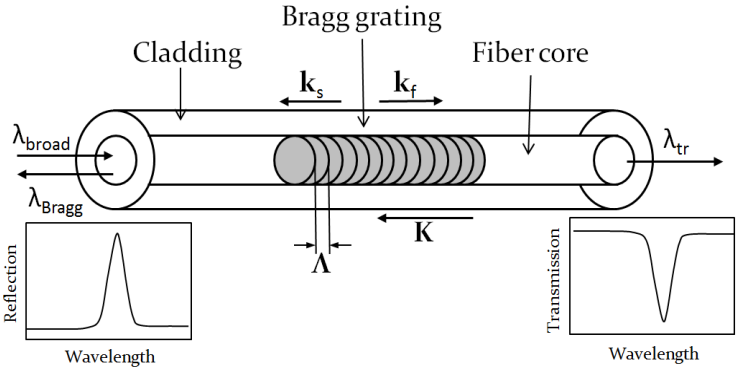

Figure 2.1. Illustration of a uniform Bragg grating with constant index of modulation amplitude and period. Incident, diffracted and grating wave vectors are also shown.

According to the Fresnel reflection, light traveling between media of different refractive indices may both reflect and refract at the interface. The same phenomenon takes place in an FBG. Each grating plane reflects and scatters some portion of light. If the phase matching (or so-called Bragg) condition is not satisfied, the light is canceled out, since the light reflected from each grating plane becomes out of phase. But when the Bragg condition is satisfied, each grating plane adds a small portion of coherent light and forms a back reflected peak with a center wavelength defined by the grating parameters. This is similar to the effect of X-rays hitting a set of planes of atoms in a crystal at a specific angle, which was discovered by William L. Bragg (1890-1971).

In a first approximation Bragg condition can be derived from energy and momentum conservation. From the energy conservation follows that the frequency of forward incident radiation equals the frequency of the reflected light: $\hbar\omega_s = \hbar\omega_f$. Momentum conservation can be stated as:

$$k_f + K = k_s \tag{2.1}$$

where the grating wavevector $\boldsymbol{K}$ has a direction normal to the grating planes and a magnitude $\boldsymbol{2\pi/\Lambda}$, where $\boldsymbol{\Lambda}$ is the grating period (see Fig.

2.1). Since the diffracted wavevector and the incident wavevector are equal in magnitude (follows from the energy conservation), but opposite in direction, the momentum conservation condition becomes:

$$2\left(\frac{2\pi n_{eff}}{\lambda_B}\right)=\frac{2\pi}{\Lambda}, \tag{2.2}$$

which can be simplified to the first-order Bragg condition:

$$\lambda_B = 2n_{eff}\Lambda, \tag{2.3}$$

where n_{eff} is the effective refractive index of the fiber core, Λ is the grating period and λ_B is the Bragg wavelength, which is the center wavelength of the input light that is back-reflected from the Bragg grating. The effective refractive index quantifies the velocity of propagating light as compared to its velocity in a vacuum and depends not only on the wavelength but also (for multimode waveguides) on the mode in which the light propagates. For this reason, it is also called modal index.

From this simple equation (2.3) one can already make a very important conclusion – the reflected Bragg wavelength depends on the effective refractive index of the core and the grating period. If even one of these parameters is affected by strain, temperature or another external influence - then the Bragg wavelength shifts. Exactly this characteristic makes fiber Bragg gratings perfectly suitable for sensing. Since the reflected wavelength is sensitive to external influences (strain, temperature, humidity, etc) by measuring the Bragg wavelength one can measure the desired measurand. And that is the principle of FBG sensing.

The most popular and historically the first physical quantities, which were measured by FBG, are strain and temperature. Let's consider how the Bragg wavelength depends on the applied strain. From Eq. 2.3:

$$\Delta\lambda_B = 2\left(\Lambda\frac{\partial n_{eff}}{\partial l}+n_{eff}\frac{\partial\Lambda}{\partial l}\right)\Delta l \tag{2.4}$$

The first term corresponds to the strain-optic induced change in the refractive index, where the second component reflects a change in the grating spacing. This strain effect can be expressed as [9]:

$$\Delta\lambda_B = \lambda_B(1-p_e)\frac{\Delta l}{l} \tag{2.5}$$

where p_e is an effective strain-optic constant defined as:

$$p_e = \frac{n_{eff}^2}{2}\left[p_{12} - \nu(p_{11}+p_{12})\right] \tag{2.6}$$

where ν is the Poisson's ratio, p_{11} and p_{12} are components of the strain-optic tensor. Figure 2.2 shows experimental results of typical FBG sensor based on silica single-mode fiber. The measured strain sensitivity at 1550 nm is around 2 pm/με.

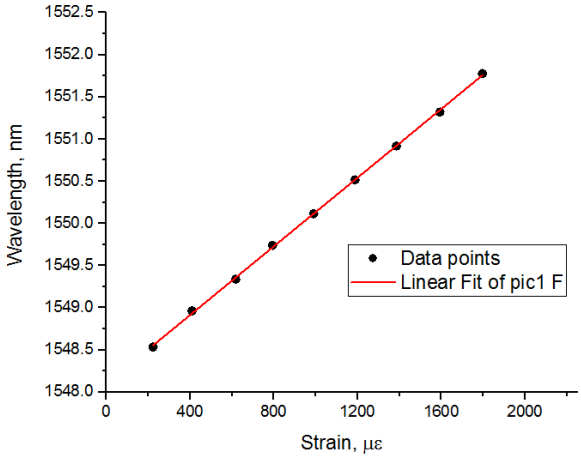

Figure 2.2. Bragg wavelength shift under applied strain

The shift in the Bragg wavelength due to the temperature changes can be expressed as (also from Eq. 2.3):

$$\Delta\lambda_B = 2\left(\Lambda\frac{\partial n_{eff}}{\partial T} + n_{eff}\frac{\partial\Lambda}{\partial T}\right)\Delta T \tag{2.7}$$

Temperature changes both index of refraction (the first term) and grating spacing (second term). Equation 2.7 can be rewritten [9]:

$$\Delta\lambda_B = \lambda_B(\alpha_n + \alpha_\Lambda)\Delta T \tag{2.8}$$

where α_n is the thermo-optic coefficient (approximately equal $8.6\text{x}10^{-6}$) and α_Λ represents the thermal expansion coefficient for the fiber and approximately equal to $0.55\text{x}10^{-6}$. Figure 2.3 shows a typical FBG

thermal response with the measured temperature sensitivity about 12.8 pm/C. Figure 2.2 and 2.3 also show that the wavelength shift is linear to the applied strain and temperature; this is a very important property of FBGs, deviations from the linearity will be discussed in Chapter 5.

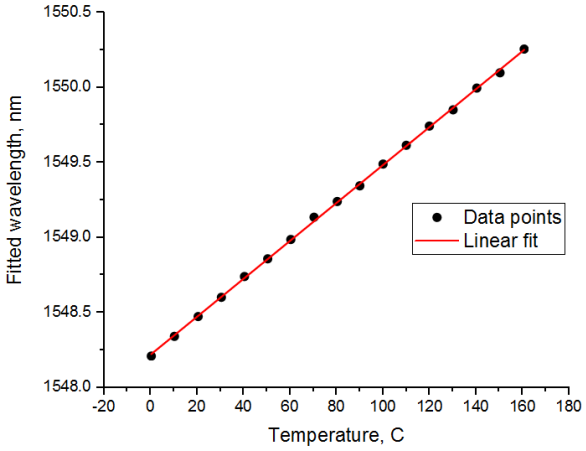

Figure 2.3. Bragg wavelength shift under applied strain

One can clearly notice that the refractive index change is much higher that the fiber thermal expansion. However, for the practical applications, this might not be true if an FBG is embedded into a structure with much higher thermal expansion coefficient, for example in a polymer 3D printed structure. By doing this one can gain the temperature sensitivity by the factor of 10, thereby highly increasing temperature resolution of the FBG sensor system. These results will be shown in Chapter 8.

It becomes obvious that an FBG is sensitive to both temperature and strain. Thus, by measuring only wavelength shift it is not possible to discriminate whether the shift was affected by the strain or by the temperature. This is probably one of the most significant limitations of Bragg gratings as sensors. That is why many solutions and techniques have already been proposed in order to overcome this issue.

The simplest solution is to use two different gratings, where one is used to measure only temperature Bragg shift ($\Delta\lambda_1$) and decoupled from mechanical impacts. The second grating, in this case, will

measure both temperature and strain response ($\Delta\lambda_2$). The temperature compensated strain can be derived from Eqs. 2.5 and 2.8 and given by:

$$\frac{\Delta l}{l} = \frac{1}{1-p_e}\left(\frac{\Delta\lambda_2}{\lambda_{B2}} - \frac{\Delta\lambda_1}{\lambda_{B1}}\right). \tag{2.9}$$

However, in some applications this approach may not be practical - sometimes it is not so easy to embed two separate gratings, even if they are written in the same fiber. Moreover, it also effects on the sensor price.

Basically, all temperature and strain decoupling methods can be classified as: a) intrinsic, which rely on the fiber properties) and b) extrinsic, when the grating is combined with an external material. One of the easiest extrinsic methods is to mount an FBG in a package with very low-temperature sensitivity or in other words to nullify the temperature to wavelength coefficient. The package is made of two materials with different thermal-expansion coefficients. As the temperature rises the strain is progressively released, compensating the temperature dependence of the Bragg wavelength [10]. Temperature stability can be improved by a factor of 10 with this method. The second extrinsic method two Bragg gratings are mounted on opposite surfaces of a cantilever [11]. When one grating is stretched, the other is compressed and the difference in Bragg wavelengths is temperature independent.

The next technique uses intrinsic properties of chirped grating in a tapered fiber. It was shown by Xu et al. [12] that these gratings can be temperature independent. Applied strain changes only the bandwidth of the reflected signal, hence the strain is intensity encoded. The intensity of the reflected signal is temperature independent. Although this approach solves the temperature stability of the FBGs it has a few disadvantages: 1) tapered section weakens the fiber and requires more complicated production process; 2) system losses will strongly affect system accuracy and produce measurement errors. In addition, all the methods listed above don't provide a separate temperature measurement.

The most desired solution would be to use only one grating to measure two quantities. This can be done by gratings inscribed in few-mode fibers [13] or by gratings in a single-multi-single mode (SMS) structure [14]. In all these approaches the reflected spectrum has at least two wavelengths; each wavelength is sensitive to strain and temperature, which can be expressed as:

$$\begin{pmatrix} \lambda_1 \\ \lambda_2 \end{pmatrix} = \begin{pmatrix} K_{1T} & K_{1\varepsilon} \\ K_{2T} & K_{2\varepsilon} \end{pmatrix} \begin{pmatrix} T \\ \varepsilon \end{pmatrix} \tag{2.10}$$

By solving a set of equations (2.10) one can discriminate strain and temperature:

$$\begin{pmatrix} T \\ \varepsilon \end{pmatrix} = \frac{1}{K_{1T}K_{2\varepsilon} - K_{1\varepsilon}K_{2T}} \begin{pmatrix} K_{2\varepsilon} & -K_{1\varepsilon} \\ -K_{2T} & K_{1T} \end{pmatrix} \begin{pmatrix} \lambda_1 \\ \lambda_2 \end{pmatrix} \tag{2.11}$$

It must be noted that the solution exists only when the determinant is not equal to zero, or in other words $K_{1T}/K_{2T} \neq K_{1\varepsilon}/K_{2\varepsilon}$. In [13] strain sensitivity was the same for different wavelengths and the discrimination is possible due to the difference in the temperature sensitivity. In [14] authors utilized the difference in response between excited modes in the multimode fiber and the FBG spectrum. Another method, which uses the same matrix approach, is based on inscribing two overlapping gratings at 2 different wavelengths [15]. The technique exploits temperature and strain coefficients dependence on the Bragg wavelength. Xu et al. [15] reported a difference of 6.5% in strain and 9.8% in temperature for gratings written at 848 and 1298 nm. Using the matrix approach they could measure strain and temperature simultaneous with an error of ±10 με and ±5 C. Unfortunately these methods have also some disadvantages. The SMS structure requires extra effort in production. The matrix method is based on the assumption of the linear response and due to the presence of the high order modes in the multimode fiber the linearity degrades (will be discussed in Chapter 5). Usually, the difference in the coefficients is not so big, and that makes the determinant in (2.11) pretty small and very sensitive to even small relative errors in strain and temperature measurement. The dual-wavelength grating method requires a very big

separation in wavelength, otherwise, the determinant is almost equal to zero, but with the big wavelength separation, two broadband sources and an interrogator with broad bandwidth are also required, which increase complicity and price of the final sensor system. There are currently no methods for simultaneous strain and temperature measurement using FBGs, which combine simplicity of the final system, low error, high precision and low price.

In addition to strain and temperature, fiber Bragg gratings can be used to measure pressure, surrounding refractive index (SRI) [16] and dynamic magnetic field. Xu et al. demonstrated $\Delta\lambda/\Delta P$ to be $3x10^{-3}$ nm/MPa for a 1550 nm FBG [17].

2.3 Fiber Bragg grating interrogation

The basic principle of FBG sensing is to measure and extract information wavelength-encoded in the Bragg reflection. Since the measurand is typically encoded spectrally, it is required to use a special device, called interrogator or demodulator, which measures the Bragg wavelength shifts and converts it to a variation of an electrical signal compatible with the common standards of instrumentation. The general principle of FBG interrogation is shown in Figure 2.4. Light from an Optical source is directed through a coupler (or circulator) and reflected at an FBG. The reflected light is sent back through the coupler to the input of a Photodetection and Processing unit.

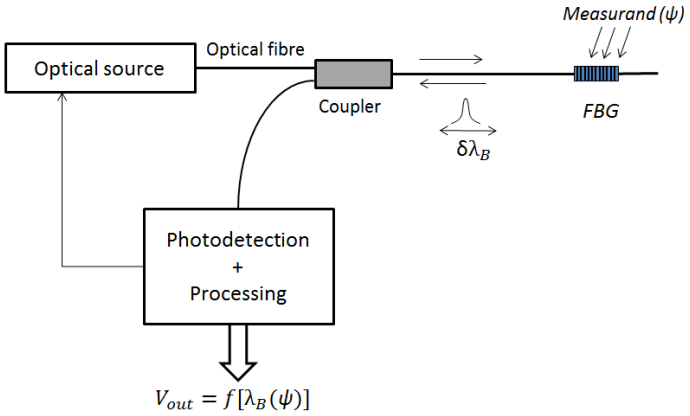

Figure 2.4. General scheme of FBG interrogation process.

In the laboratory, during FBG developing and investigation, optical spectrum analyzers (OSA) are often used to monitor grating transmission or reflection spectra. However, optical spectrum analyzers are not attractive in practical application due to their slow scanning speed, big size, limited resolution capability, and lack of ruggedness and cost-effectiveness.

Many different techniques and concepts have been developed to make an FBG interrogation faster, cheaper, more robust and precise. Usually, the wavelength measurement is not very straightforward; thus, the general principle is to convert the wavelength shift to some easily measured parameter, such as amplitude, phase, or frequency. By the type of wavelength shift conversion interrogation techniques can be divided into 5 different groups:

1. Wavelength-Amplitude conversion
2. Wavelength-Frequency conversion
3. Wavelength-Phase conversion
4. Wavelength-Time conversion
5. Wavelength-Position conversion

The most important parameters of an FBG interrogator are wavelength interrogation range, wavelength detection resolution (often is not the same as the optical resolution), acquisition rate (scanning speed), size, weight, and price.

2.3.1 Wavelength-Amplitude conversion

Conversion of Bragg wavelength shift to amplitude changes is one of the easiest interrogation techniques and it makes the interrogation process simple and cost-effective. One can divide wavelength-amplitude interrogation schemes into two groups – *Passive* and *Active* detection schemes.

Passive detection scheme

As the name suggests, no electrical, mechanical or optical active devices are used during interrogation. The Bragg wavelength is measured by detecting optical power of the signal by means of wavelength-dependable devices, such as, for instance, filter, couplers,

gratings. All intensity-based schemes have one potential problem – the measured light intensity might be changed due to not only the reflection Bragg wavelength change but also due to the power fluctuation of the light source, the disturbance in the light-guiding path, or the dependency of light source intensity on the wavelength. Therefore it is necessary to use intensity referencing components.

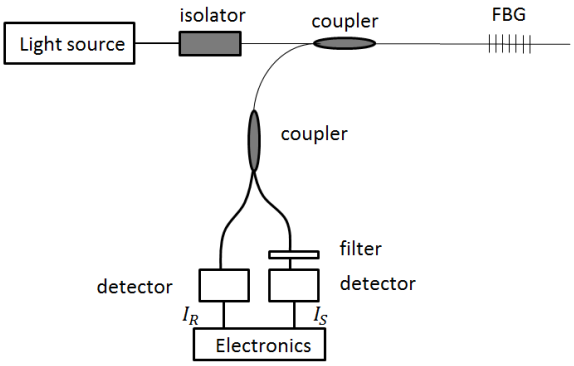

Figure 2.5. Basic scheme of an interrogator with a linearly wavelength-dependent filter.

Figure 2.5 shows the schematic diagram of the FBG sensor system based on the wavelength-dependent optical fitter, where the light reflected from the FBG is split into two arms; one of them passes through the filter, while the other is used as a reference. This was also one of the first proposed schemes FBG interrogators [18]. The filter used in this scheme has a linear response range and so-called as an edge-filter or a broadband filter. Here information relative to wavelength change is obtained by the intensity monitoring of the light at the detectors.

The intensity ratio at the two detectors is given by:

$$\frac{I_S}{I_R} = A(\lambda_B - \lambda_0 + B) \tag{2.12}$$

where $\boldsymbol{A}$ is a slope filter constant and $\boldsymbol{B}$ is a constant arising from the nonzero reflection bandwidth of the FBG. Due to the use of the second reference detector the intensity variations are canceled out by dividing the signal $\boldsymbol{I_S}$ with the reference $\boldsymbol{I_R}$. Therefore, equation (2.12) is linearly dependent only on the Bragg wavelength change.

A similar approach was demonstrated by Davis and Kersey [19]. Instead of a wavelength-dependent optical they used a wavelength division multiplexer coupler, which has a linear and opposite change in the coupling ratios between the input and two output ports. The power loss is reduced, and a static strain resolution of ~±3.5με for the range of 1050 με was obtained. The scheme described above can be further modified - one can also use a light source with intensity linearly dependable on wavelength, for example, amplified spontaneous emission (ASE) profile of an erbium-doped fiber amplifier (EDFA) [20]. If the Bragg wavelength of a sensor grating is located in the linear region of the ASE spectrum, the change in the Bragg wavelength results in a same power change at the photodiode.

Active detection schemes

Active detection schemes usually involve tracking, scanning, or modulating mechanisms to monitor Bragg wavelength shifts. The active schemes show better resolution compared to the passive detection schemes, but they usually are more complex.

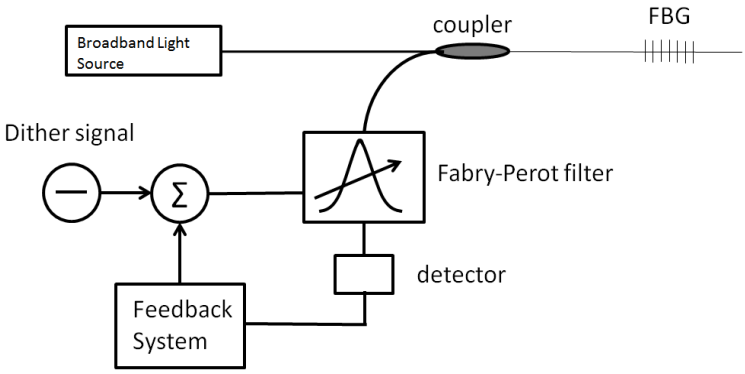

Figure 2.6. Schematic diagram of the Fabry-Perot filter interrogator sensor system working in a lock-in mode.

The first active detection scheme is based on the use of a fiber-pigtailed Fabry–Perot tunable filter [21]. Typically, tunable fiber FPFs bandwidth is about 0.2 to 0.6 nm with a spectral range of 60 nm. The filter transmission wavelength (i.e., resonance wavelength) is periodically changed by the sinusoidal dithering of the cavity length

(Fig. 2.6). If the filter resonance wavelength matches the Bragg wavelength, the measured signal has the second harmonic component and no signal at the dithering frequency. When the FBG wavelength is shifted the first order harmonic appears and used as the input error signal of the feedback system. The Bragg shift is proportional to the DC voltage applied to the FPF.

In the previous scheme, the Fabry-Perot tunable filter can be replaced by an FBG, which is mounted on a piezoelectric stretcher. The second gratings reflecting wavelength is identical to the sensed grating wavelength when no stress applied. The wavelength demodulation algorithm is equal to the Fabry-Perot technique described above.

WL tunable sources

In this technique a wavelength tunable source is used instead of a super fluorescent broadband source. This fact highly increases the signal-to-noise ratio (SNR), since the wavelength tunable source has a relatively high power and a narrow linewidth. The high SNR may significantly decrease the integration time resulting in a fast sensor response or may allow making accurate measurements in noisy environments.

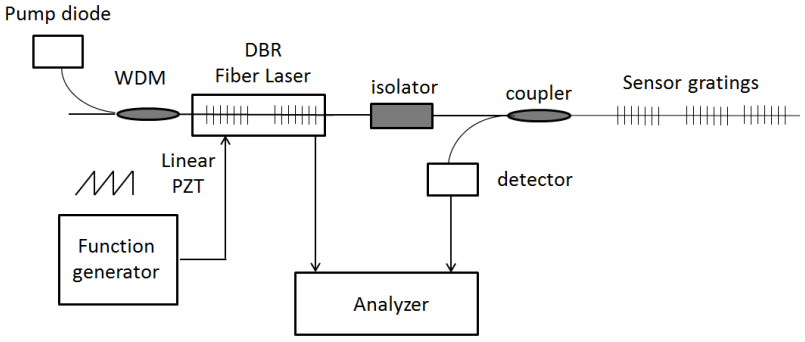

Figure 2.7. Schematic diagram of an interrogation by wavelength tunable source (WDM: wavelength division multiplexer; DBR: distributed Bragg reflector).

By tuning the wavelength of the laser source over a spectral range of interest it is possible to interrogate the spectral change in the sensor grating, since the source wavelength is known.

The wavelength tunable EDF laser has been demonstrated for the interrogation of a three-FBG sensor by Ball et al. [22]. A single frequency fiber laser that utilizes intra-core Bragg gratings for wavelength selectivity is mounted to a linear piezo-translator (Fig. 2.7). To remove hysteresis and achieve a calibrated and linear expansion position sensors and an expansion control loop were applied to the piezoceramic. The fiber laser wavelength could be linearly tuned by driving the PZT with a saw tooth waveform. In [22] the fiber laser was able to tune a total of 2.3 nm with the resolution of approximately 2.3 pm, which corresponds to a temperature resolution of 0.2°C.

The number of scanned FBGs can be significantly increased by using a wavelength tunable laser sources with a high power density of the emitted light. A scan ring laser based on semiconductor optical amplifier and tunable Fabry-Perot interferometer can provide 70nm bandwidth and 32 monitoring channels, and therefore the interrogator can simultaneously detect more than 1000 fiber Bragg grating sensors.

This interrogation technique is also used by one of the biggest interrogators manufacturers, company called Micron Optics. It allows them to reach an ultra-fast speed of scanning, up to 2 MHz with 24 pm (20 με) resolution on the full speed. For the regular speed of scanning (~100 Hz-1 kHz) the resolution is around 1-2 pm.

2.3.2 Wavelength-Frequency conversion

Wavelength-Frequency conversion technique is based on a tunable bandpass filter where arrays of FBG's are illuminated by a broadband source and the output is detected by a broadband receiver. One of the examples of such kind of filters is an acousto-optic tunable filter (AOTF). The fibre-pigtailed AOTF acts as an optical bandpass filter, where the diffracted wavelength (bandpass wavelength) is selected by varying the acoustic frequency. It is important to notice that compared to Fabry-Perot filter AOTF range of scanning is much bigger. As a result, by changing the radio-frequency (RF) of the AOTF, it is possible to interrogate a sensor grating the same way as using other bandpass filters, for example, Fabry-Perot filter. Figure 2.8 shows a schematic diagram of the AOTF interrogator.

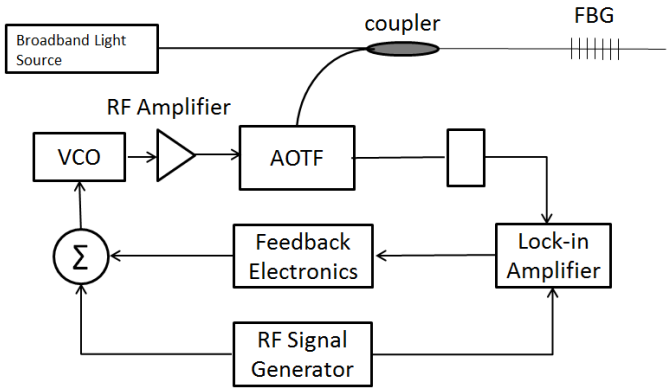

Figure 2.8. Schematic diagram of AOTF interrogation (VCO: voltage-controlled oscillator)

The interrogation system allows two modes of interrogation: a scan mode and a lock-in mode. In the scan mode, the feedback loop is disabled and the AOTF is tuned via a voltage-controlled oscillator over the wavelength range of interest. The power reflected from the gratings is recorded. The recorded signal is a convolution of the spectra of the gratings and the spectrum of the AOTF in the wavelength domain.

In the lock-in mode, the system tracks the wavelength of a particular grating using the feedback loop. The AOTF is dithered with a feedback loop, and the lock-in signal with the dithering frequency is detected.

The AOTF technique has several advantages. It can be accessed at multiple wavelengths simultaneously as well as at random wavelengths. This is obtainable by applying multiple RF signals of different frequencies. Hence, the AOTF can offer a parallel interrogation and a reduction of interrogation time in a multiplexed sensor array system.

The AOTF interrogation technique has been demonstrated by Geiger et al [23] and a standard deviation of 0.4 με was achieved at a measurement period of 100 ms. The measurement resolution could be improved by measuring the AOTF mean frequency over a longer period. However, in this case, the interrogation system requires a longer response time.

2.3.3 Wavelength-Phase conversion

In this interrogation technique, the FBG wavelength shift is converted to the phase shift of the interference signal in the output of an interferometer, which is then measured by the detector. Typically, Mach-Zehnder interferometers (MZI) are used to achieve very high resolution [24].

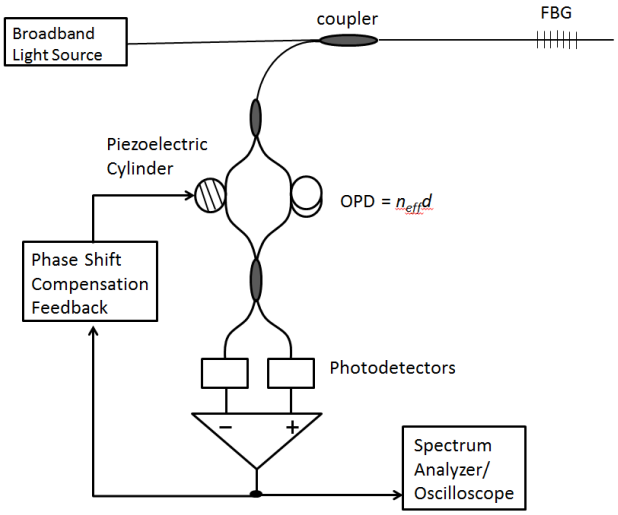

Figure 2.9. Unbalanced Mach-Zehnder interferometer interrogator.

Figure 2.9 shows a schematic diagram of the Unbalanced Mach-Zehnder interferometer interrogator. The reflected FBG signal is fed to the interferometer. The wavelength shifts induced by perturbation of the grating resemble a wavelength (optical frequency) modulated source. An unbalanced interferometer behaves as a spectral filter with a raised cosine transfer function; the wavelength dependence on the interferometer output can be expressed as

$$I = I_0(1 + a\cos\left[2\pi\frac{n_{eff}d}{\lambda} + \psi\right]) \qquad (2.13)$$

where ***I0*** is proportional to the input intensity and system losses, ***a*** is related to the temporal coherence of the light reflected by the FBG, ***d*** is the length imbalance between the fibre arms, ***n*** is the effective index of the core, ***λ*** is the wavelength of the return light from the grating sensor (sensor signal) and ***ψ*** is a bias phase offset of the Mach-Zehnder interferometer. If the Bragg wavelength is changed then the phase in

Eq. (2.13) is changed; by analyzing the phase change, the applied measurand information can be obtained.

The maximum sensitivity of the interferometer is related with the interferometer's OPD (optical path length difference) and the coherence of reflected light (which is inversely dependent on the FBG reflection bandwidth). Weis et al. [25] found that the maximum sensitivity is when $n_{eff}d\Delta k=2.355$, where $\boldsymbol{\Delta k}$ the bandwidth of FBG reflection spectrum expressed in wavenumber units.

When a fiber grating with a strain sensitivity of 1.2 pm/ με and a reflection wavelength of 1550 nm is used with the 4.5-mm optical path unbalanced MZI, the phase change response is ~12 rad/nm. By using a phase meter with a 0.1° resolution one can obtain the strain resolution of ~0.13 με and for the quasi-static and dynamic strain, respectively.

2.3.4 Wavelength-Time conversion

The main idea of this technique is to convert the grating wavelength shift to a temporal shift in the arrival time of the reflected pulses (Figure 2.10). Broadband, ultrafast pulses, generated by a passively mode-locked erbium-fiber laser, are launched into FBG sensors via a highly dispersive fiber. Reflections from individual gratings propagate back through the dispersive fiber and are monitored by a fast detector and a sampling oscilloscope. The high dispersion of the dispersive fiber converts strain- and temperature-induced wavelength shifts into a shift in the pulse arrival time at the detector. The reflected signal from an array of fiber Bragg gratings is thus a sequence of pulses separated by the time of flight between the gratings, plus a wavelength-dependent delay resulting from the double-pass through the DCF. For applications in which the physical spacing L between gratings is effectively constant (i.e., for small eL), only changes in the Bragg wavelength will shift the relative time of the reflected pulses.

When standard wavelength-domain demodulation is used, the maximum strain that can be measured by a grating in an array is limited by the spectral separation between adjacent gratings. Time-domain demodulation overcomes this restriction: as only the induced delay is measured, the wavelengths of different gratings can shift or

even overlap each other. This effect can lead to a great dynamic range of operation and increase the number of gratings per spectral bandwidth in an array.

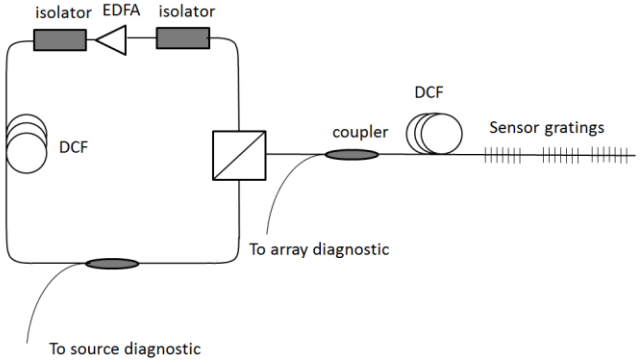

Figure 2.10. Schematic diagram of interrogation by passively mode-locked fiber lasers with wavelength-time conversion

In the experiment of Putnam et al. [26], the mode-locked output power was in excess of 50 mW, and the bandwidth and the repetition rate were 80 nm and ~7 MHz, respectively. The sensitivity was determined to be approximately ±20 με over 3500 με.

2.3.5 Wavelength-Position conversion

The principle of this approach is based on the spectrometry. In such a system wavelength interrogation is achieved with a fixed dispersive element (e.g., prism or grating), which spreads different wavelength components at different positions along a line imaged onto an array of detector elements. Linear CCD cameras used so that light with a different wavelength will be projected to a different position on the CCD, as shown in Fig. 2.11. The optical resolution of the measurement is dependent on the spatial resolution of the bulk grating and the number of the CCD pixels. For a typical spectrometer based interrogator, the center-to-center pixel spacing corresponds to ~0.10-0.20 nm, which is around 120-200 microstrain. The precise central positions of each peak along the CCD array can be extremely enhanced to sub-pixel level by applying different peak fitting algorithms, such as centroid (Center of Gravity) fitting algorithm, Gaussian fitting algorithm etc. With this approach it is possible to reach the

wavelength resolution less than 1 pm which corresponds with around 1 με. The fitting algorithm has a huge impact on the spectrometer-based interrogator performance, in Chapter 4 a new fitting algorithm will be presented.

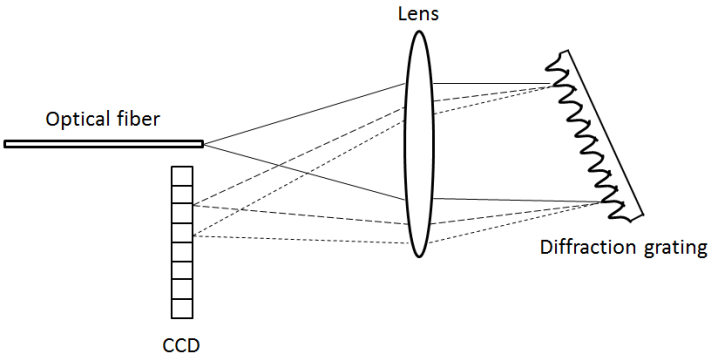

Figure 2.11. Schematic diagram of the wavelength interrogation system using a CCD and a plane reflection phase grating. The dashed and dotted lines indicate lights with different wavelengths.

As far as the light from the FBG is distributed along the detector, this scheme is well suitable for wavelength division multiplexing (WDM) and the number of FBGs which can be measured simultaneously is limited only by the covered range and wavelength distance between closest gratings.

With a combination of very fast measurement frequency, low power consumption and compact size, spectrometer based interrogators are well suited for a broad range of applications.

The wavelength-position approach will be used further in this work to develop a new type of an FBG interrogator.

Chapter 3

Polymer optical fiber Bragg gratings

This chapter is dedicated to polymer optical fiber Bragg gratings – historical perspective, FBG inscription techniques and comparison with the glass ones. It continues with the last progress in polymer FBG field. Polymer fiber Bragg grating sensors and their applications will also be discussed here.

3.1 Historical perspective

Historically, first Bragg gratings in bulk sample of polymethyl methacrylate (PMMA) were created in the 1970s at Bell Labs in the USA – much earlier than the discovery of photosensitivity in silica fibers. Unfortunately, it took more than 20 years before single-mode polymer optical fiber (POF) became available in the 1990s. The first FBG in a multimode polymer optical fiber was demonstrated only in 1999 by Gang-Ding Peng, Pak L. Chu and colleagues at the University of New South Wales, Australia [27] – 10 years later than conventional FBG in silica fiber was inscribed. Later they also demonstrated FBG in single mode fiber and showed high reflectivity of 28 dB [28]. In 2005 gratings in microstructured polymer fiber were demonstrated by Dobb et al [29]. Compared to the silica fibers, where the optimum range with

the minimum losses is 1550 nm, for polymers typical losses in this range are quite high – around 1 dB/cm for PMMA based fibers. It has been found that for polymers lower loss regions are in shorter wavelength – the 600nm region, the 800nm region [30]. Figure 3.1 shows attenuation loss of common polymers in comparison with silica. Consequently, the Bragg wavelength in polymer optical fibers is usually lower compared to the silica.

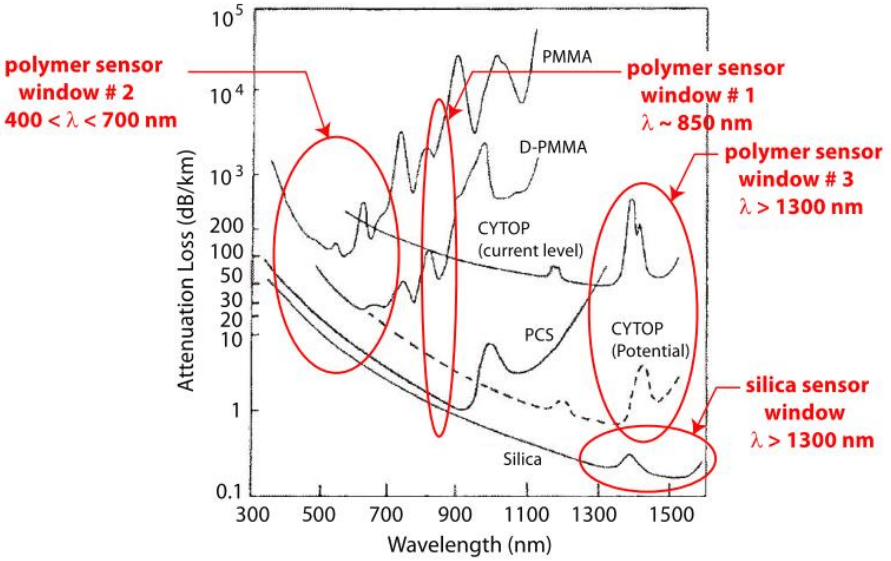

Figure 3.1. Attenuation loss of common optical polymers as a function of wavelength (taken from Kara Peters [30])

Temperature and strain sensitivity of polymer fiber Bragg gratings were studied soon after the demonstration of the first POFBG [31]. However, in the temperature experiments humidity was not controlled and this led to problems since PMMA is sensitive to water, which causes increase fiber refractive index. Harbach et al studied the influence of humidity on the Bragg wavelength of POFBG in PMMA based fiber [32].

The polymers most commonly used for the production of optical fibers are polymethyl methacrylate (PMMA), the amorphous (non-crystalline) fluoropolymer CYTOP, cyclin olefin copolymer (TOPAS), polycarbonate (PC). Different polymers can offer different properties

to fibers and FBG sensors. For instance, compared to PMMA TOPAS has several advantages, the biggest one is that TOPAS is insensitive to water [33]. Polycarbonate microstructured optical fibers can be used at temperature up to 120 °C and break at considerably higher strains than PMMA [34].

It can be also noted that at the time of writing there is only one commercial supplier of single-mode POF – Paradigm Optics and also there is a lack of single mode POF components, like couplers, pigtailed connectors. The lack of single mode fibers can be explained. Small numerical aperture and a small core are required to reduce the number of modes, which sets very high requirements for production. It is very hard to control these parameters during fabrication. That is why multimode polymer fibers are so popular and consideration should be given to the multimode polymer fiber Bragg gratings (will be done in next chapters).

3.2 FBG: POF vs silica

The main difference between polymer and silica fibers lies in the difference of mechanical properties of these two materials. The biggest difference is that silica is an isotropic elastic material, while PMMA (as the basis of most fibers used in POFBG research) is a viscoelastic material. The Young's modulus of silica is around 73 GPa [35] and PMMA's Young modulus is typically around 3.3 GPa [36]. Much lower Young modulus can be an advantage in situations where stiff fibers can strongly affect the measurand by locally reinforcing highly compliant structures, for example, Plastic fiber biotextiles [37]. For dynamic applications, like acoustic sensing or accelerometry, the low Young modulus of optical fibers is also very attractive. Stefani et al [38] demonstrated a high sensitivity POF based accelerometer with sensitivity a factor of 4 higher than an equivalent silica fiber. Another advantage of POFBG sensors, which also follows from its lower modulus, is much higher failure strain, which can reach up to 100% for PMMA based fibers [39], however, this value can strongly vary depending on polymer processing and fiber annealing [40]. But for pure silica fibers, the failure strain is only 5-10% [41].

Due to the visco-elastic nature POFBG demonstrate hysteresis to increasing and decreasing strain as shown in Figure 3.2. However, for some applications it may not be even an issue when a fiber is embedded in a material, which reduces the hysteresis problem, by forcing the fiber back to its original length. The hysteresis can also be reduced by application of pre-tension or thermal annealing [43].

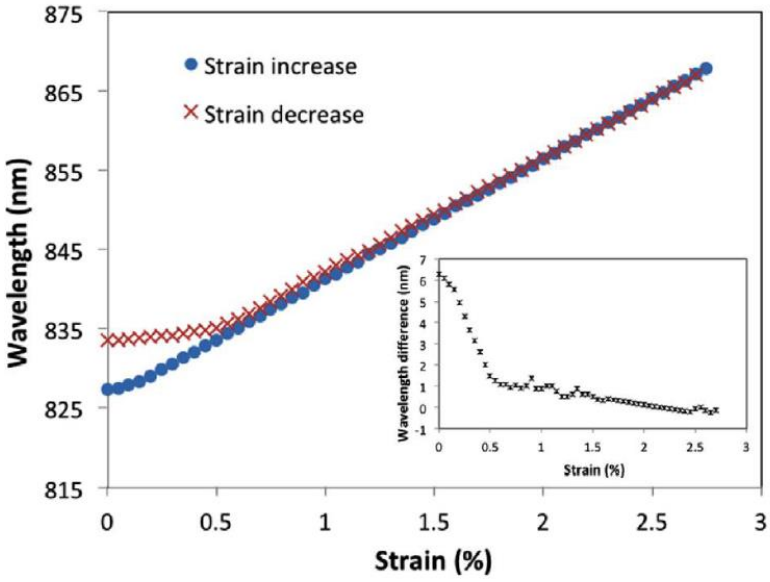

Figure 3.2. FBG wavelength peak versus strain, for the POFBG sensor in PMMA fiber. Inset shows the wavelength difference between readings taken between increasing and decreasing the strain (image taken from of Abang et al. [41])

Another big difference is that, in contrast to silica, polymers (at least some of them, like PMMA) are water sensitive [36]. Water absorption causes an increase in fibers refractive index and swelling of the fiber. Both of these effects lead to the Bragg wavelength shift. This phenomenon can be a big disadvantage, when the water sensitivity is not needed, or a big advantage for humidity sensor development. The humidity sensitivity depends also on polymer processing and fiber annealing. G. Woyessa et al. showed that the PMMA microstructured POFBG demonstrates the largest sensitivity to humidity when the fiber was annealed up to 90 % RH [44]. They also showed that mPOF PMMA FBG sensor is temperature insensitive and suites very well for

humidity measurements. However, as mentioned before, the water sensitivity can be a big disadvantage where POFBG are supposed to be used as strain and temperature sensors. For these applications, humidity insensitive TOPAS can be used as a fiber material. G. Woyessa et al demonstrated a single mode polymer humidity insensitive FBG sensor made of a TOPAS core and a ZEONEX cladding [45].

Temperature sensitivity of POFBG is also different from silica gratings. As was shown in the previous chapter, temperature changes both index of refraction and grating spacing (Eq. 2.8). For silica, both coefficients (thermo-optic for refraction index change and thermo-expansion for elongation) are positive, which is not the case for polymer fibers. For polymers, the thermo-optic coefficient is usually negative, which means that the wavelength shift can be positive or negative, depending on which coefficient is bigger [46]. Usually, for PMMA POFBGs, the temperature sensitivity varies from -10±0.5 pm/°C to -36±2 pm/°C, depending on the humidity in the environment [32]. Silica FBGs can be used for temperature sensing up to few hundred degrees, whereas POFBGs are limited by their low glass transition temperature. It means that POFBGs can be used as temperature sensor only up to 80-90 °C [47]. However, last works show that the temperature range can be expanded up to 125 °C for polycarbonate (PC) micro-structured polymer optical fiber [48].

3.3 Bragg grating inscription

Since an FBG is a structure with periodically modulated refractive index of the core, in order to make an FBG one should somehow to change the refractive index. This can be done by using UV light. Photosensitivity of polymer optical fibers is a complex topic and can be attributed to different mechanisms such as photo-degradation, photo-crosslinking and photo-isomerization [32]. Despite different mechanism of photo-induced refractive-index change for silica and for polymer fibers, Bragg grating inscription techniques are almost the same for silica and POF. There are 3 main methods used to inscribe fiber Bragg grating in polymer optical fiber.

1) Interferometric technique. Firstly was demonstrated by Meltz and co-workers in 1989 for FBG inscription in silica fibers [49]. In this method, the incoming UV beam is split into two beams of equal intensity by a beam splitter and then the beams are recombined to produce an interference pattern. This method was used to inscribe the first POFBG by Peng and co-workers in 1999 (Figure 3.3) [27,50].

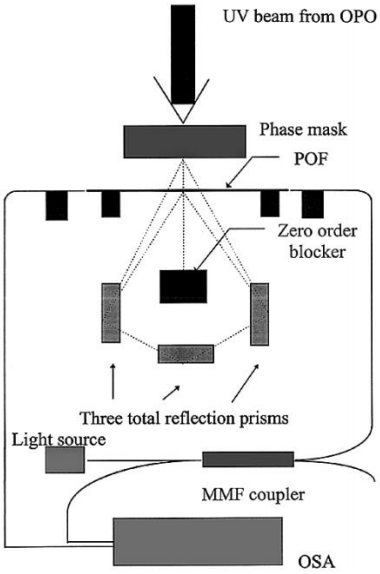

Figure 3.3. Scheme of interferometric inscription method used by Peng and co-workers to inscribe first POFBG (image taken from [50])

The main advantage of this method is high flexibility and ability to inscribe FBG at any desired wavelength by changing the intersecting angle of the two beams. However, this method has high sensitivity to mechanical vibrations, it requires very good laser source with good spatial and spatial coherence and excellent wavelength stability.

2) Phase mask technique. The phase mask technique is probably the most common method to inscribe FBG. The phase mask (PM) is basically a transmission grating optimized to diffract light equally and maximally into the plus first and minus first orders. Self-interference between the two orders creates an interference pattern immediately behind the phase mask with half the Phase mask period. A typical FBG inscription setup using a phase mask is shown in Figure 3.4. The UV

light of 325 nm after being reflected on several mirrors is focused by a plano-convex cylindrical lens through the phase mask down on to the fiber, which is lying about 100 μm below the phase mask.

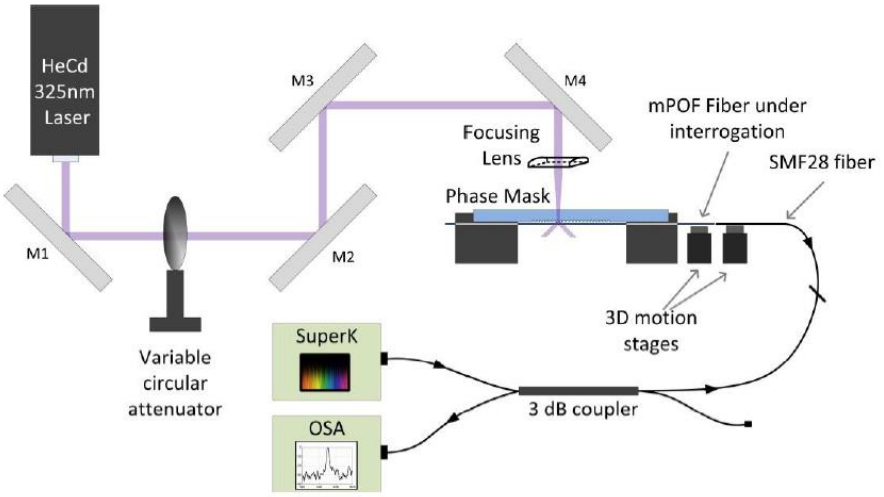

Figure 3.4. Scheme of phase mask inscription (image taken from [51])

The intensity of the zero-order diffracted beam can decrease the fringe contrast, thus, it is very important to suppress it as much as possible. The zero-order diffracted beam is suppressed down to less than 2% for phase mask produced by Ibsen Photonics. The zero-order suppression is done by optimizing the depth of the periodic structure of the PM.

A main advantage of the phase mask inscription technique is that this method is very robust and stable, it is simple to use and doesn't require high temporal coherence. A drawback of the phase mask technique is limited Bragg wavelength tunability – one phase mask can only write FBGs at a certain wavelength. However, this problem can be partly solved by stretching the fiber during the inscription process, especially for polymer fibers with their large elastic range. In addition to phase masks optimized for 1550 nm FBG inscription, which are commonly used for silica fibers, Ibsen Photonics also produces PMs for 600nm and 800nm FBG inscription, which are now widely used with polymer fibers to make POFBGs.

3) Point-by-point technique. The point-by-point (PbP) technique offers the highest flexibility among the other inscription techniques – gratings of any length, width and period can be made by the PbP technique. In this method, a grating is inscribed by changing the refractive index of the fiber core point-by-point moving the fiber connected to a translation stage. The stage is the core of this technique and the stage precision is the key point. However, nowadays one can get a very precise motorize or piezo stage with sub-micron precision.

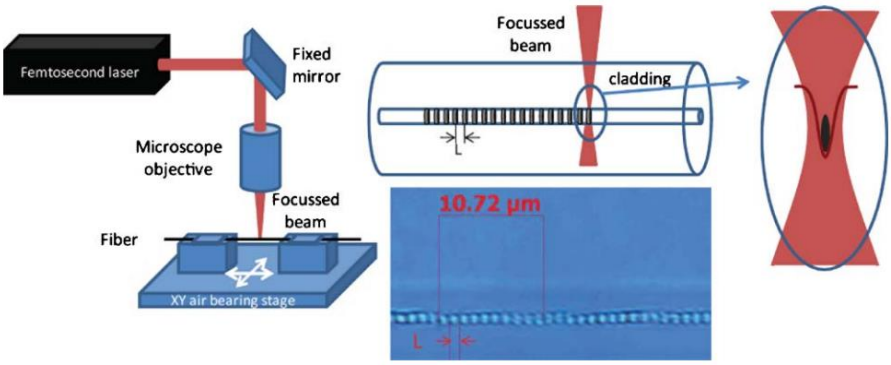

Figure 3.5. Scheme of point-by-point inscription (image taken from [52])

Using femtosecond laser in combination with the PbP technique one can significantly decrease the inscription time down to tens of seconds [52]. T. Geernaet et al showed that grating can be inscribed in 10 seconds in photonic crystal fiber with a period of 539 nm. A. Lacraz et al used this method together with a femtosecond laser to inscribe 1550 nm gratings in CYTOP multimode fiber with 70% of reflectivity [53].

Chapter 4

This Chapter along with the majority of its graphs, tables and images is based on the following publication: "Dynamic gate algorithm for multimode fiber Bragg grating sensor systems" [54].

Dynamic Gate algorithm

Different interrogation techniques have been already discussed in Chapter 2 and the most common and commercially available of them – spectrometer based and swept laser based – sample the reflected spectrum with a finite sample step, for spectrometers given by the pixel pitch in the diode array. The optical resolution of these techniques is often limited by the sample resolution and is relatively poor compared to, for example, Fabry–Perot filters [21] and Mach–Zehnder interferometers [24]. The resolution in the detected FBG peak position can be enhanced to subpixel level by applying different peak fitting algorithms, such as center of gravity (COG) [55] and Gaussian fitting [56]. However, the fitting algorithm should be chosen carefully to achieve the best wavelength fit resolution. Most of the conventional algorithms are designed to work with sharp Gaussian peaks and use a constant number of pixels for peak fitting. This can result in inaccurate results, when the peak shape is not sharp and narrow and if the peak shape changes during measurements.

In this chapter I will present a fast and accurate peak detection algorithm, which is well suited for spectrometers with a limited number of pixels. The algorithm is based on a threshold determined

fitting window and a modified COG algorithm with bias compensation. Thus, the number of pixels used for peak determination is not constant and changes during measurements. This approach avoids sudden shifts in the fitted wavelength and improves the wavelength fit resolution. Using simulations and experiments, we investigate the static and dynamic behaviors of the proposed method and compare it with other algorithms: COG, least squares Gaussian fitting and the linear phase operator (LPO) algorithm [57].

4.1 Dynamic gate algorithm principles

The basic principle of FBG sensing is to measure the reflected spectrum and to track the FBG peak position. Most conventional algorithms use a constant number of samples (pixels) for peak position calculations. The first step of these algorithms is to find the local maximum point and then take ***n*** points (neighbors) to the left and ***n*** points to the right of the maximum, so the total number of points is ***2n+1***. Problems with this approach may appear when there is uncertainty in the determination of the maximum point. For example, as shown in Fig. 4.1(a), the maximum can be point number 1, but due to noise, the maximum can jump to point number 2.

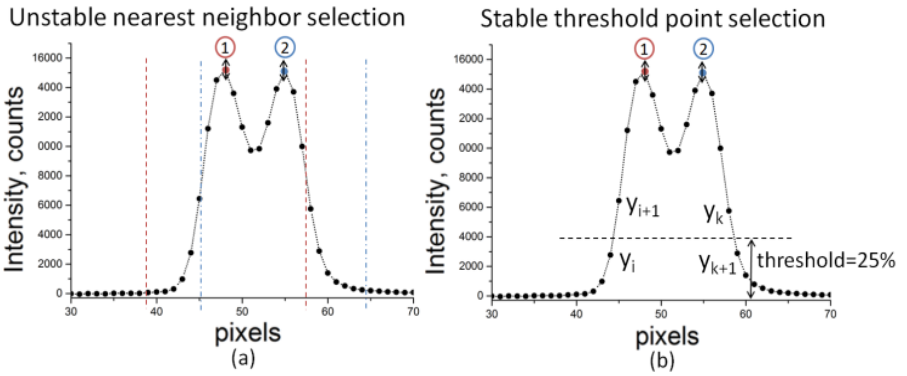

Figure 4.1. (a) The fitting window shift on non-uniform double peak FBG spectrum, number of neighbors=10; (b) The threshold fitting window determination principle, with a threshold= of 25% of the maximum.

These jumps lead to changes in the points used for peak fitting. When point 1 is maximum, the selected points are between the two red

dashed lines and when point 2 is maximum, the selected points are between the two blue dashed–dotted lines. The sudden jumps in the fitting window may produce sudden shifts in the fitted wavelength as will be illustrated later in this chapter. One way to avoid this problem is to simply increase the number of points in order to be sure to always cover the whole peak. However, this approach has disadvantages: (I) the fitting speed will be reduced, (II) adding side points will increase the noise and decrease the fit resolution, and (III) if peaks are close to each other the increased number of points may lead to the use of points from the neighboring peak.

To overcome this problem we propose a threshold-based point selection, where all points higher than or equal to a threshold T will be selected, as shown in Fig. 4.1(b).

As we mentioned in the Introduction, our algorithm is based on COG calculations. The standard COG of the points selected by the threshold method described above can be found by the following equation:

$$COG = \frac{\sum_{j=x_{i+1}}^{x_k} x_j y_j}{\sum_{j=x_{i+1}}^{x_k} y_j}. \qquad (4.1)$$

A problem appears when the threshold level crosses one of the points. Let us consider what happens when the threshold T relatively shifts towards to the point with coordinates (y_i, x_i) [see Fig. 4.2(a)]. Since the threshold-based point selection method takes all points with intensity higher than T, when the threshold goes below yi the total number of points in Eq. (4.1) increases by 1. This leads to a sudden shift of the COG value calculated by Eq. (4.1) and thus, a shift in the fitted wavelength.

To overcome this issue we developed a sub-pixel endpoint interpolation. Let us assume that $y_i<T< y_{i+1}$, see Fig. 4.2(b). Our objective is to find values of χ and γ, which can be added to the numerator and denominator in Eq. (4.1) to indicate the real threshold

position and to avoid the sudden shift described above. These values (χ, γ) can be associated with coordinates of a point or endpoint, however, it must be noted that there is no real point there and γ is not equal to the intensity of the point with x-coordinate χ.

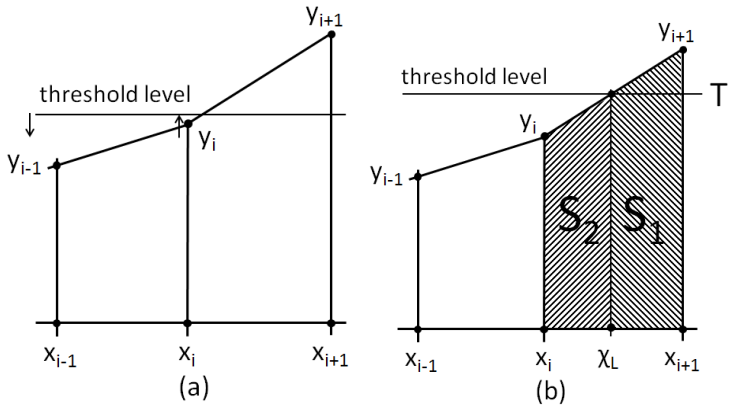

Figure 4.2. (a) The threshold problem; (b) The endpoint interpolation

The parameter γ can be considered as the additional amount of energy limited by the threshold. To overcome the problem, the "coordinates" of the left endpoint (χ_L, y_L) should meet the following boundary conditions:

$$\chi_L \to x_{i+1};\ \gamma_L \to 0 \quad \text{when} \quad T \to y_{i+1}; \tag{4.2}$$

$$\text{and} \quad \chi_L \to x_i;\ \gamma_L \to y_i \quad \text{when} \ T \to y_i. \tag{4.3}$$

In other words, the parameter χ_L is the x-coordinate of the point where the threshold T crosses the line which connects points y_i and y_{i+1} [see Fig. 4.2(b)] and the parameter γ_L is proportional to the amount of energy between χ_L and x_{i+1}. Assuming a linear interpolation, γ_L is proportional to the area of the trapezoid S_1:

$$\frac{\chi_L - x_i}{x_{i+1} - x_i} = \frac{T - y_i}{y_{i+1} - y_i} \quad \text{and} \quad \frac{\gamma_L}{y_i} = \frac{S_1}{S_1 + S_2}; \tag{4.4}$$

where S_1 and S_2 are trapezoids shown in Fig. 4.2(b). Solving Eq. (4.4) gives the "coordinates" (χ_L, γ_L) for the left endpoint:

$$\chi_L = x_i + \frac{T - y_i}{y_{i+1} - y_i}; \quad \gamma_L = y_i \frac{y_{i+1}^2 - T^2}{y_{i+1}^2 - y_i^2}. \tag{4.5}$$

Applying the same reasoning for the right endpoint gives:

$$\chi_R = x_k + \frac{y_k - T}{y_k - y_{k+1}}; \; \gamma_R = y_{k+1} \frac{y_k^2 - T^2}{y_k^2 - y_{k+1}^2}. \tag{4.6}$$

Here (x_i, y_i), (x_{i+1}, y_{i+1}), (x_k, y_k) and (x_{k+1}, y_{k+1}) are the coordinates on each side of the threshold ***T*** on the left and right side of the peak, respectively, see Fig. 4.1(b). The updated COG is then found by the following equation:

$$COG = \frac{\chi_L \gamma_L + \chi_R \gamma_R + \sum_{j=x_{i+1}}^{x_k} x_j y_j}{\gamma_L + \gamma_R + \sum_{j=x_{i+1}}^{x_k} y_j}. \tag{4.7}$$

The fitting window borders are limited by the left endpoint χ_L and by the right endpoint χ_R and it is no longer discrete. This fact allows us to avoid sudden jumps of the fitting window, which appears when the measured peak shifts.

The last step of the proposed algorithm is to process the selected points. Originally, we selected the COG algorithm for this purpose, because it is fast and has high accuracy, but the COG is sensitive to the bias level of the measured signal. To overcome that problem we developed a modified COG algorithm with bias compensation.

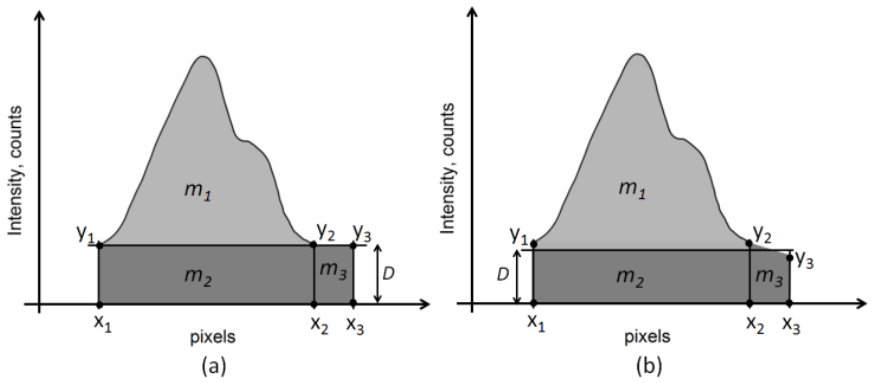

Figure 4.3. Principle of bias compensation when (a) $y_2 = y_3$ and (b) $y_2 \neq y_3$.

Now suppose that we need to find the COG of the continuous shape m1 limited by the points with coordinates x_1 and x_2, which is biased by the D level [light grey color in Fig. 4.3(a, b)]. The parameter ***m*** is proportional to the mass of the selected shape and, assuming constant density, ***m*** is proportional to the area of the selected shape. By definition, the x-coordinate ***c*** of the center of mass satisfies the equation:

$$(m_1 + m_2)c = m_1 x + m_2 x_c, \tag{4.8}$$

where ***c*** is the COG of the whole shape between x1 and x2 including the bias part (m_2).

Here our goal is to find x, which is the bias compensated COG of shape m_1. The x-coordinate x_c of the center of mass of the bottom shape m_2 filled with the dark grey color [see Fig. 4.3(a, b)] can be easily found, since it is rectangular and thus $x_c=(x_1+ x_2)/2$. Let $x_3= x_{2+1}$ and, by definition, the coordinate ***r*** of the center of mass of the shape between x_1 and x_3 can be found by the following equation:

$$(m_1 + m_2 + m_3)r = m_1 x + (m_2 + m_3)(x_c + 1/2), \tag{4.9}$$

where $m_3 = m_2/(x_2 - x_1)$ and ***r*** is the COG of the whole shape between x_1 and x_3 including the bias part (m_2 and m_3).

Solving Eqs. (4.8) and (4.9) and assuming that in our case the selected signal is limited by the left endpoint χ_L and by the right endpoint χ_R we find ***x***, which is the bias compensated COG of the measured spectrum:

$$x = \frac{kc + x_c(c - r)}{k + c - r} \tag{4.10}$$

$$\text{with} \quad c = \frac{\sum_{j=\chi_L}^{\chi_R} x_j y_j}{\sum_{j=\chi_L}^{\chi_R} y_j}; \quad r = \frac{\sum_{j=\chi_L}^{\chi_R+1} x_j y_j}{\sum_{j=\chi_L}^{\chi_R+1} y_j};$$

$$k = \frac{2(x_c - r) + \chi_R - \chi_L + 1}{2(\chi_R - \chi_L)}; \quad x_c = \frac{\chi_R + \chi_L}{2}.$$

Here we assumed that the amplitudes in points x_2 and x_3 are equal to each other, i.e., $y_2 = y_3$, and in this case $D = y_2$ [Fig. 4.3 (a)]. If $y_2 \neq y_3$, the bias level D is equal to the average of y_2 and y_3, or $D = (y_2 + y_3)/2$ [see Fig. 4.3 (b)]. The calculated peak position λ_B found by the DGA is equal to the bias compensated COG given by Eq. (4.10) where χ_L and χ_R are the coordinates given by Eqs. (4.5)-(4.6).

4.2 Simulations and results

To evaluate the proposed algorithm, we performed simulations and comparisons using three different measured FBG spectra, as can be seen in Fig. 4.4. The aim of the first test was to calculate the wavelength fit resolution σ given by Eq. (4.11):

$$\sigma = \sqrt{\frac{1}{N}\sum_{i=1}^{N}(x_i - \mu)^2}, \tag{4.11}$$

where $\mu = \frac{1}{N}\sum_{i=1}^{N} x_i$ and x_i is the calculated peak position at the ith repetition.

We added white Gaussian noise with a signal-to-noise ratio (SNR) of 10 and 30 dB to the measured spectra (Fig. 4.4). For each value of the SNR the peak position was calculated 100,000 times to determine the wavelength fit resolution σ [see Eq. (4.11)]. The peak position was calculated in pixels using Eq. (4.10), and then converted to wavelength applying the spectrometer calibration coefficients. For the first spectrum, FBG 1, which is a typical single mode FBG peak, the maximum point is stable. Therefore, there are no sudden jumps of the fitting window and all algorithms perform well, as can be seen in Fig. 4.5. The number of neighbors ***n*** was set to be 3 for FBG 1.

Problems appear with FBG 2 and FBG 3, for which the maximum position is not stable. In order to overcome the problem with the sudden jumps appearing when using the conventional algorithms, we

increased the number of neighbors to cover the whole peak. We selected 12 and 14 nearest neighbors for FBG 2 and FBG 3, respectively.

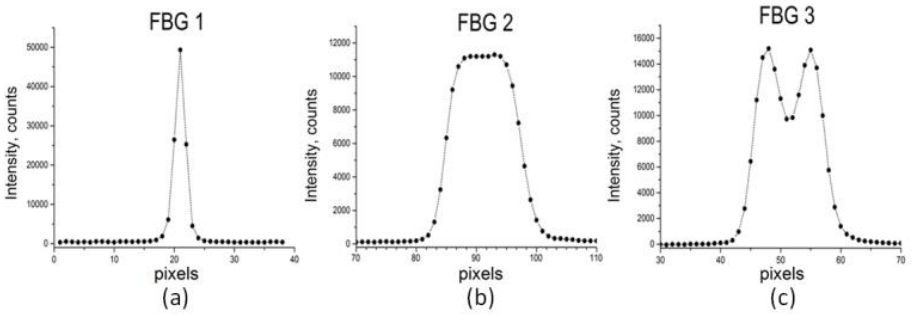

Figure 4.4. (a) FBG 1 – single mode spectrum, (b) FBG 2 - few mode spectrum and (c) FBG 3 – few mode spectrum

The threshold in the DGA was set at 30% for all measurements. As can be seen, our algorithm shows the best fit resolution for FBG 2 and FBG 3 for both low and high SNR (Fig. 4.5). For SNR=10 dB the DGA improves the fit resolution by 32% for FBG 2 and by 63% for FBG 3 compared to the best conventional algorithms [see Fig. 4.5 (a)]. When the SNR is increased up to 30 dB the DGA improves the fit resolution by 33% for FBG 2 and by 47% for FBG 3 compared to the best conventional algorithms. When the peak shape is known, as for example for FBG 1 with the Gaussian shape, the best fit resolution is obtained with the Gaussian fitting. However, for FBG 1 the DGA improves the wavelength resolution by 24% compared to the COG algorithm and shows almost the same result as the LPO algorithm. The DGA is less sensitive to white Gaussian noise because it uses fewer points for fitting compared to the conventional algorithms. Especially, the algorithm allows to avoid side points with very low SNR, whereas conventional algorithms such as COG and LPO are required to cover the whole peak during measurements to provide accurate peak determination. One can also notice that the DGA fit resolution is almost insensitive to the peak shape, whereas the conventional algorithms, such as the Gaussian and LPO algorithms, demonstrate a strong dependence on the peak shape.

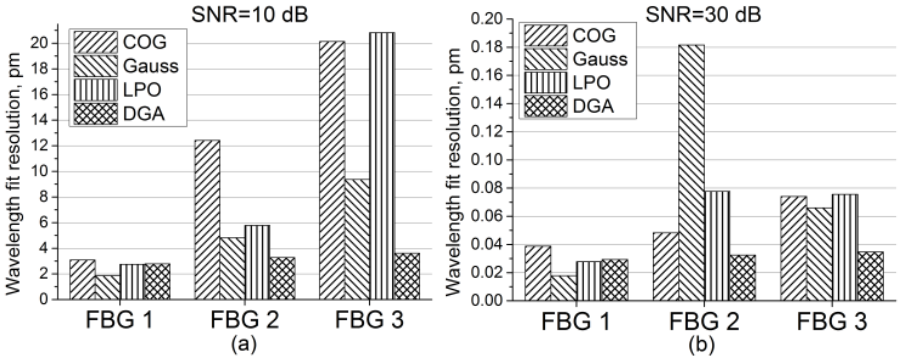

Figure 4.5. Wavelength fit resolution with low SNR=10 dB (a) and high SNR=30 dB (b).

The computation speed is another important parameter for the performance evaluation of the proposed algorithm. It should be noted that the absolute computation speed depends on the number of points and the number of peaks.

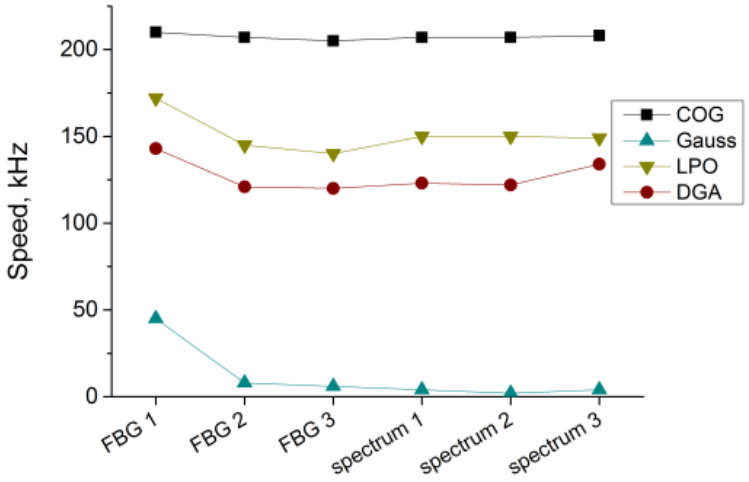

Figure 4.6. Absolute computation speed for 6 different spectra.

To calculate and compare the computation speed we used the 3 spectra shown in Fig. 4.4 (FBG 1, FBG 2, FBG 3) and 3 spectra (spectrum 1, spectrum 2, spectrum 3) from Fig. 4.8(b). The same data was fed to all algorithms, the number of neighbors and the threshold level was set to achieve the best fit resolution. All algorithms were implemented in LabVIEW. We ran each algorithm 200,000 times in a

cycle loop and measured the total time. The absolute speed illustrated in Fig. 4.6 was obtained by dividing the total time by the number of iterations (200,000). We would like to stress that the presented absolute speed is the pure algorithm computation speed, and in a real system the maximum measurement speed is often limited by the raw spectrum read-out time. To ease the comparison we normalized the absolute speed using the COG speed as a reference. Table 4.1 reports the average relative speed for all different algorithms.

Table 4.1. Average relative speed of computation.

Algorithm	COG	Gauss	LPO	DGA
Relative speed, %	100	6	73	61

The DGA is 10 times faster compared to the Gaussian fitting and only 39% slower than the simplest COG algorithm. The proposed method represents an excellent compromise between the fit resolution, robustness and computation speed.

4.3 Experimental evaluation

An experiment was carried out to validate the simulations and to demonstrate the effectiveness of the proposed DGA algorithm. The experimental setup is shown in Fig. 4.7.

An FBG was written in a commercially available multi-mode POF manufactured by Mitsubishi. The core is made of PMMA (polymethyl-methacrylate) with refractive index 1.492 and the cladding is a thin layer of perfluorinated polymer with a lower refractive index of 1.402. The multimode fiber has a core and cladding diameter of 240 and 250 μm, respectively. An FBG was written into the POF using the standard phase mask UV-writing technique with a 50 mW HeCd CW laser (IK5751I-G from Kimmon) operating at 325 nm.

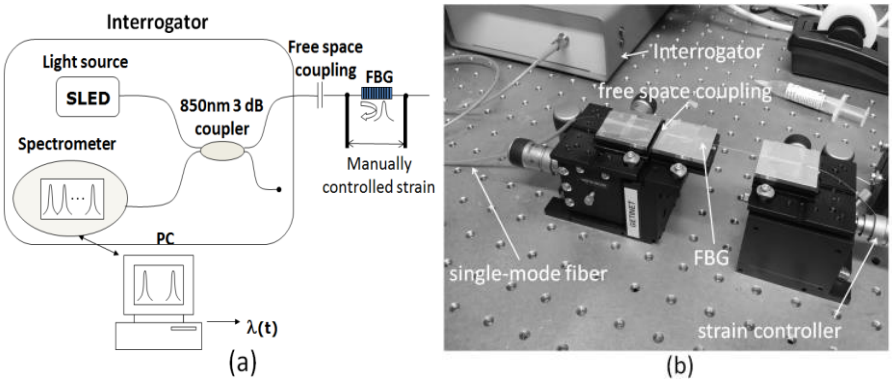

Figure 4.7. Experimental configuration.

The fiber with the FBG was glued to two XYZ stages and coupled to an SMF28 fiber, which is connected to a commercially available interrogator from Ibsen Photonics A/S [see Fig. 4.7]. Index matching oil was put in between the SMF28 and the interrogated fiber to reduce reflections and thereby minimize the noise. The wavelength range of the interrogator goes from 824 to 857 nm using a detector with 1024 pixels and, thus, the sample resolution is 32 pm per pixel.

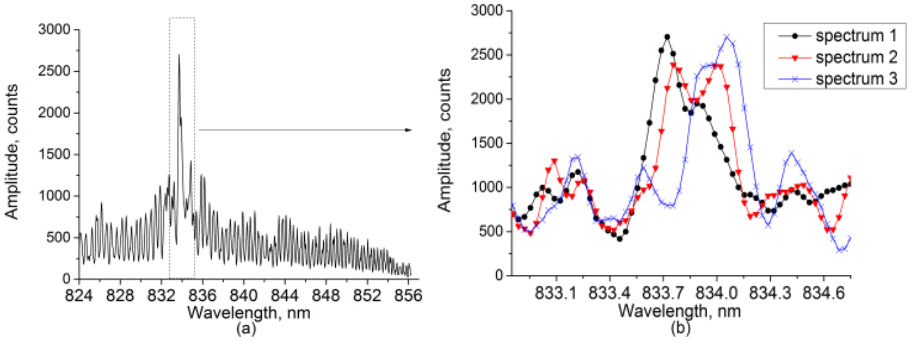

Figure 4.8. (a) Multimode FBG spectrum when no strain is applied; (b) three spectra measured during the strain test

Figure 4.8(a) shows the reflected spectrum of the FBG when no strain is applied. Since the interrogator has a single-mode fiber at the input and the FBG fiber is highly multimode, only fundamental modes can pass through the coupling [58]. The measured spectrum depended strongly on the relative position of the single-mode fiber compared to

the multi-mode in the free space coupling. The goal of this experiment was to show how the DGA can track any selected arbitrarily shaped and fluctuating peak compared to the other algorithms. The strain was continuously increased by a hand-driven screw up to 1.2 mε. The FBG spectrum was measured and saved with a frequency of 500 Hz. The raw data was processed using the COG, Gaussian, LPO and DGA algorithms. Despite the fact that the Gaussian fitting is not well suited to fit arbitrary peak forms presented in Figure 4.8(b), we included the Gaussian fitting to demonstrate how important is to use the correct fitting algorithm. The number of neighbors was optimized in order to minimize the jumps of the fitted wavelength. The DGA threshold was set at 50% of the maximum. Figure 4.8(b) shows how the tracked peak is changing during the measurements. Spectrum 1 was measured after 4 seconds; spectrum 2 was measured after 7.6 seconds and spectrum 3 was measured after 14 seconds when the strain was 0 με, 490 με and 1.2 mε, respectively. In multimode fibers, the Bragg peak position depends strongly on the mode field distribution and on the coupling conditions, which can be seen in Fig. 4.8(b), where the measured peak changes shape when strain is applied. Due to this fact, high robustness is required to fit the peak with good fit resolution. Figure 4.9 reports the fitted peak wavelength as a function of time, which is common user desire: to track a time-varying FBG peak.

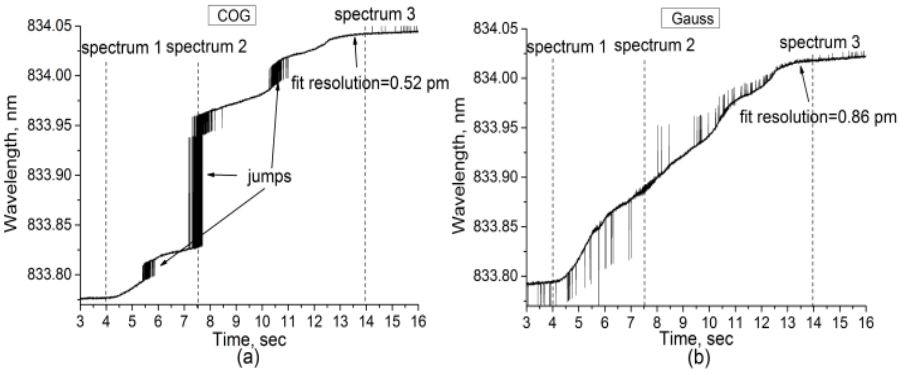

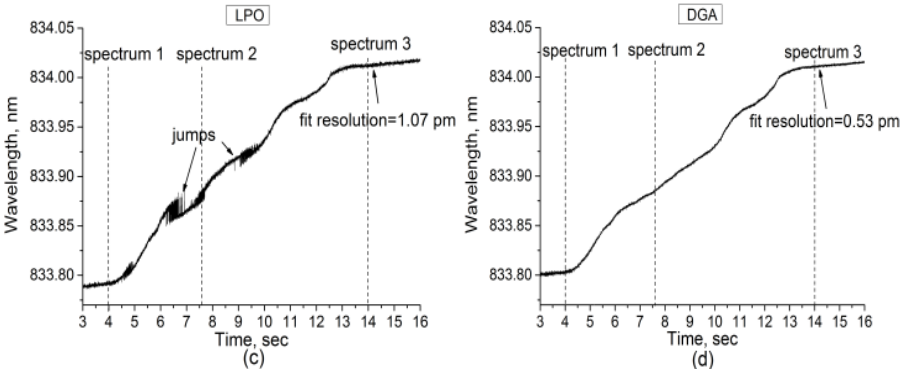

Figure 4.9. Fitted wavelength of the multimode FBG computed with (a) COG, (b) Gaussian, (c) LPO and (d) DGA algorithms.

The wavelength fit resolution was calculated as the standard deviation (Eq. (4.11) with N=500) between the measured data and their best fit. The jump magnitude was calculated as the peak-to-peak amplitude of the sudden jumps. To ease the comparison we put all numbers in Table 4.2:

Table 4.2. Best fit resolution and jump magnitude.

Algorithm	Fit resolution, pm	Jump magnitude, pm
COG	0.52	100
Gaussian	0.86	60
LPO	1.07	25
DGA	0.53	<0.5

As expected, all conventional algorithms demonstrate poor performance due to the sudden jumps in the fitting window caused by shifts in the maximum point determination, while the DGA shows a continuous response without any jumps larger than the wavelength fit resolution. Despite the acceptable fit resolution from 0.52 pm for the COG to 1.07 for LPO fitting, the overall performance of the conventional algorithms is strongly limited by the presence of fitting errors, which can reach up to 100 pm. Only the DGA allows monitoring an applied strain in this experiment continuously with a wavelength fit resolution of 0.53 pm, corresponding to 2.9 με.

4.4 Peak tracking

Let us consider the whole interrogation process for spectrometer-based interrogators. The first step is to measure a spectrum. Then the measured spectrum is processed in order to identify and calculate Bragg wavelengths. This post-processing stage is also divided into two parts: peak(s) selection (step 2) and peak(s) processing (step 3), see Figure 4.10. In the previous sections of this chapter I have presented and described the new fitting algorithm, which is step 3 in this workflow. The new Dynamic gate algorithm avoids sudden shifts in the fitted wavelength and improves the wavelength fit resolution. Now the second step will be considered in more details together with potential problems that may arise.

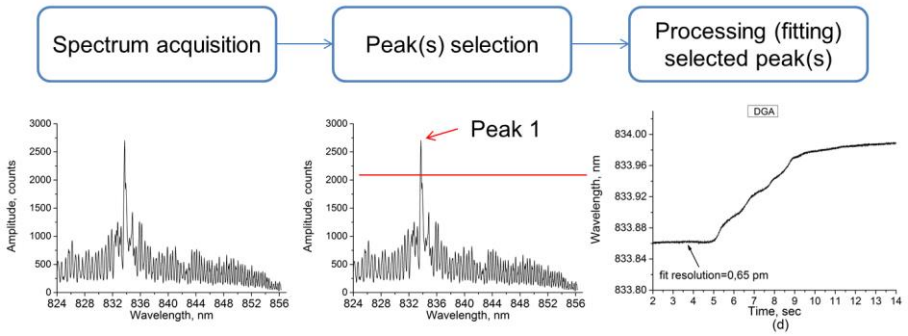

Figure 4.10. Interrogation process.

Peak selection process works in the following way – the user sets the peak searching threshold and positions of all peaks higher than the threshold are sent to the peak fitting algorithm for further calculations. FBGs written in single-mode fibers usually are very stable and their peaks have predictable behavior, usually, they don't change their intensity too much. Even if many gratings are inscribed in the same single-mode fiber and, hence, the reflected spectrum contains many peaks, the picture doesn't change during measurements. Unfortunately, everything changes in multi-mode fibers. FBGs inscribed in MMFs usually have a very unstable spectrum, which constantly changes its shape. Because of mode repartition peaks start to ascend and descend relatively the threshold. It leads to the fact that

the number and order of the peaks, which are sent to the fitting algorithm vary during the measurements and that may cause huge jumps in the fitting wavelength.

Figure 4.11 shows the reflected spectrum of an FBG inscribed in a multimode polymer optical fiber with core diameter about 62 um (FBG 1). At the beginning, before strain was applied, peak determination routine found 3 peaks (black curve, Fig. 4.11), which exceed the threshold, which was set to be 80% of maximum. When the strain was applied, the FBG spectrum was changed (blue curve). The peak, which was between peaks 1 and 2 at the initial spectrum, is now higher than the threshold and recognized as peak number 2, original peak number 2 fell down and now is between peaks number 2 and 3 and is not processed by the fitting algorithm. Moreover, a peak between 2 and 3 at the initial spectrum also exceed the threshold and now is number 3, whereas peak number 3 becomes peak number 4. It is clearly a huge mess!

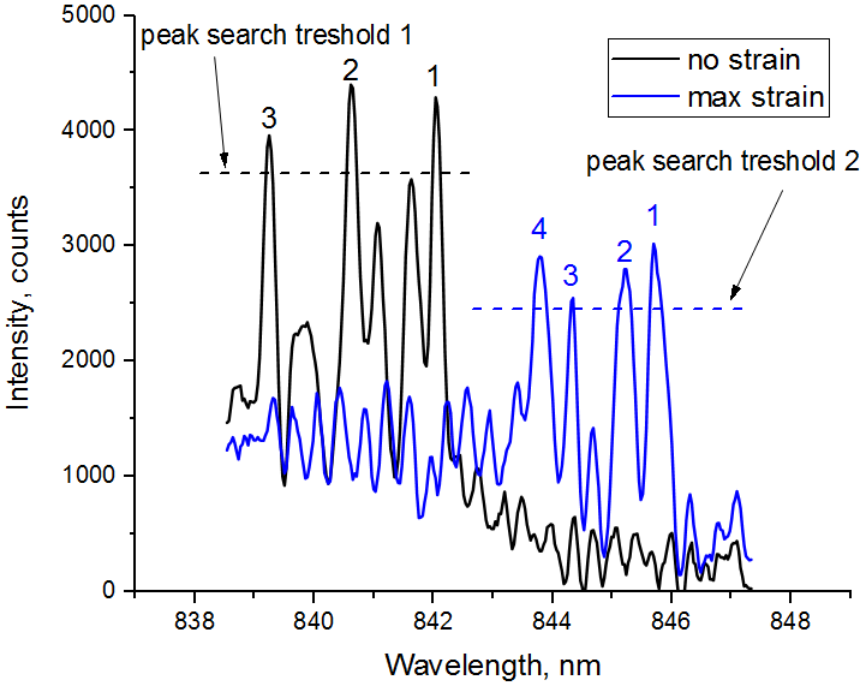

Figure 4.11. Multimode FBG spectrum when no strain is applied (black) and when the maximum strain was applied.

One could try to decrease the threshold level to get more peaks at the initial spectrum but in most cases one would fail, because it is very difficult to predict the behavior of the multimode FBG spectrum and, thus, very difficult to find the initial threshold level.

In order to overcome this problem I have developed an improved peak searching routine, which I called "Peak tracking mode". The new routine works the following way:

- The first spectrum in a sequence defines maxima points with the standard algorithm;
- Peak maximum in the next spectrum will be searched only from ***m-n*** to ***m+n*** pixel, where ***m*** is the maximum from the previous spectrum in a sequence and ***n*** is the number of pixels, defined by the user.

Here ***n*** is not the number of neighbors used to determine points for fitting.

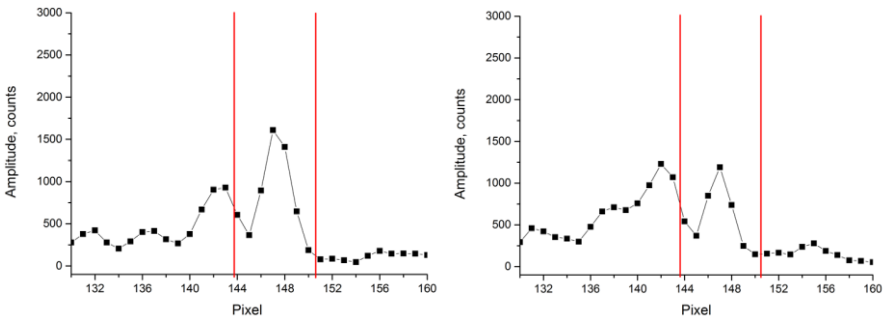

Figure 4.12. Left – first spectrum in a sequence, right – next spectrum in a sequence.

Figure 4.12 demonstrates the described principle. At the initial spectrum (left image) the standard peak searching algorithm was used and pixel 147 was identified as a peak and then was sent to the fitting algorithm to further processing, so ***m=147*** and *n* were set to be 3. In the next step, the spectrum was modified (right image) but the peak maximum will be searched only from pixel 144 to pixel 150, so the higher peak, which is on the left, is not considered and thereby no jumps occur. Thus, when the peak tracking mode is on, the software "tracks" or follows the peak(s) during measurements.

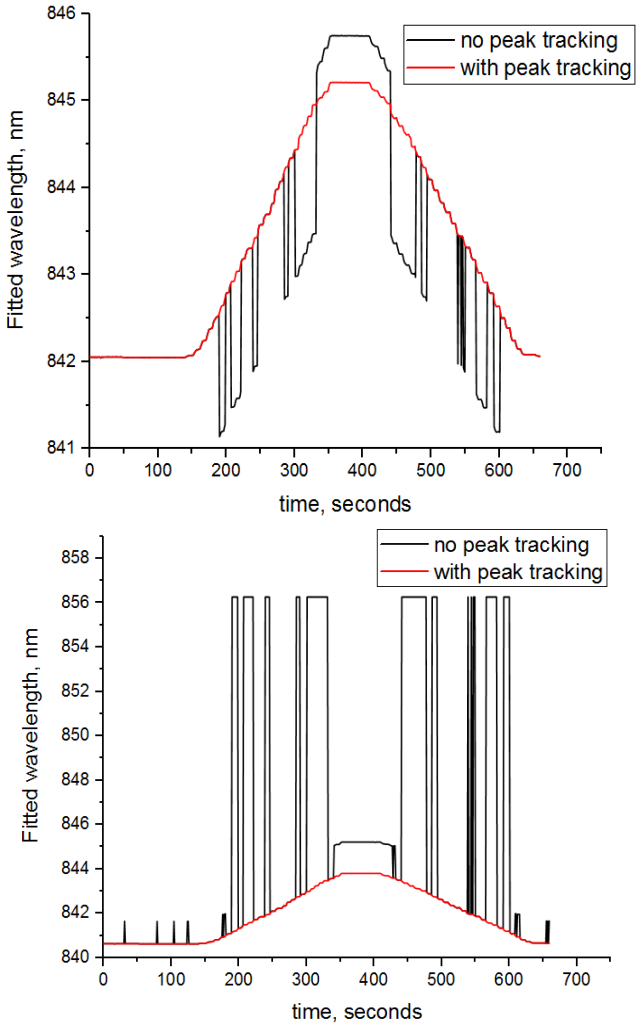

Figure 4.13. Top – peak number 1 from the FBG 1, bottom – peak number 2 from the FBG 1.

Figure 4.13 shows the difference when the peak tracking was off (black) and on (red). The top and bottom curves were obtained by tracking the peak number 1 and peak number 2 from the FBG 1, respectively (Figure 4.11). Since the peak searching routine doesn't give the precise wavelength position, the fitting algorithm is then used to determine the Bragg wavelength with high precision. The novel dynamic gate algorithm was used in both cases to calculate the fitting wavelength. The jump magnitude on the top image reaches 2 nm.

However, in the bottom image the jump magnitude is much significant (~about 15 nm) and higher than the total wavelength shift caused by the strain applied. Enabling the peak tracking mode totally changes the picture – curves are smooth and all jumps disappear.

Figure 4.14 illustrates another example. An FBG was inscribed by femtosecond laser in multimode polymer optical fiber (CYTOP). During the experiment the fiber was heated up to 60 C. Figure 4.14 (top) shows how the reflected spectrum changes. One can clearly see the peak ascending and descending phenomenon described above.

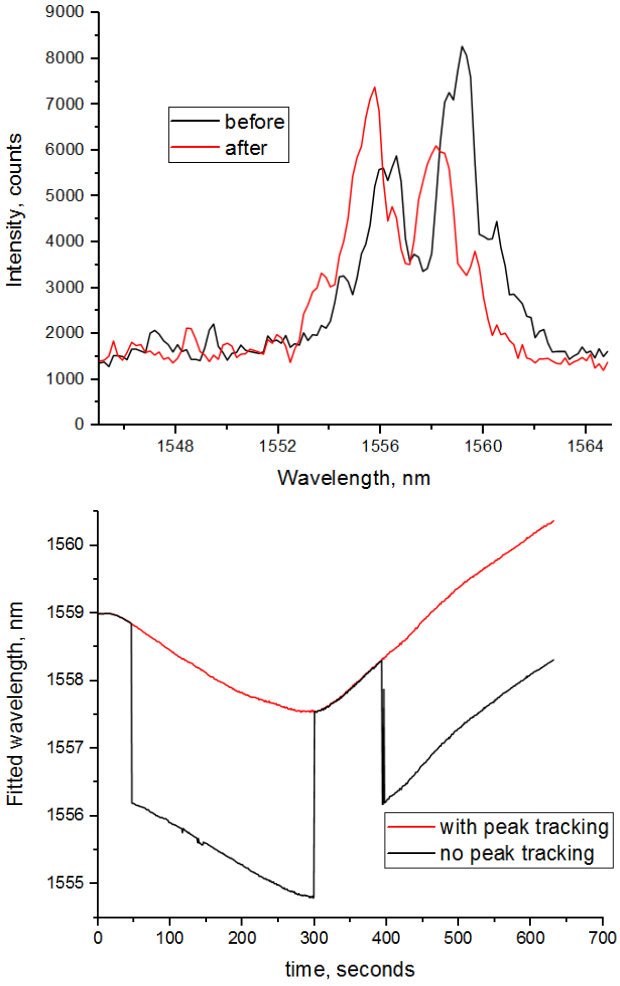

Figure 4.14. Top – multimode FBG spectrum, bottom – fitted wavelength vs time with enabled and disabled peak tracking mode.

The bottom image shows the fitted wavelength vs time. When peak tracking option is activated the wavelength curve is smooth and properly reflects the applied temperature.

4.5 Conclusions

In this chapter I presented an efficient and fast detection algorithm for FBG sensing based on a threshold-determined detection window and a bias-compensated COG. This method avoids sudden shifts in the fitted wavelength and improves the wavelength fit resolution. Simulations and experiments demonstrated that the proposed algorithm is highly robust and has significantly improved wavelength fit resolution compared with conventional algorithms. Due to the fast demodulation speed, which is 10 times faster than Gaussian fitting, the proposed algorithm can be used in dynamic-sensing systems with high-speed requirements. These properties make the DGA an attractive and suitable method for future implementation in sensing systems based on multimode fiber Bragg gratings.

A new “peak tracking” mode helps to avoid jumps and shifts, which occur due to the peak ascending and descending phenomenon and together with the dynamic gate algorithm makes the spectrum processing routine more robust and stable. It has been shown that the new fitting algorithm together with the “Peak tracking” option can fit and track arbitrary changing multimode peaks in real-time.

Chapter 5

Performance of few-mode FBG sensor system

This Chapter along with the majority of its graphs, tables and images is based on the following publication: "Performance of low-cost few-mode FBG sensor systems: polarization sensitivity and linearity of temperature and strain response" [59].

The most common and commercially available FBGs work in the 1550 nm range, primarily because of the availability of low-cost telecommunications equipment at that wavelength. However, this requires to use expensive 1550 nm InGaAs detectors to interrogate the sensors. Using 850 nm light in interrogation schemes allows installing cheaper silicon detectors and may therefore significantly decrease the detector price in spectrometer-based interrogators. Furthermore, one can get more pixels in the diode array, which means better sampling and increase of the fit resolution and/or larger measurement bandwidth. Unfortunately, 850 nm single mode fibers (SMF) are not as cheap and available as standard 1550 nm telecom fibers.

In view of these facts, it would be attractive to switch to an 850 nm sensor wavelength, while still being able to use 1550 nm fibers. An added benefit would be the possibilities for using the 1550 nm fiber distribution network in several already installed FBG sensor systems. In essence the idea is to use low-cost FBG sensor systems based on multi-mode fibers. This idea is not new

and has earlier been proposed by several groups [60], who studied such systems and demonstrated an approximately linear response of both the fundamental and higher-order modes (HOMs) [13]. It was even proposed to use the HOMs for specific measurements to detect twisting [61] and discriminate between bending and strain [62]. However, in general an approximate linear response was just assumed. In this chapter I go a step further and look more deeply into the deviations from linearity of the response actually observed but neglected in earlier papers on HOM FBG sensing.

In this chapter I therefore investigate the performance and polarization sensitivity of low-cost FBG sensor systems based on 850 nm FBGs written in a standard 1550 nm single-mode fiber. This fiber is few-moded at 850 nm, which is shown to introduce 2 satellite peaks in the FBG reflection spectrum and degrade the stability of the main FBG peak. I make a detailed comparison with systems based on 850 nm FBGs in 850 nm single-mode fibers. Using strain and temperature sensing experiments, the linearity of the two FBG sensor systems will be compared. Here a simple solution to suppress the observed higher polarization sensitivity and degraded linearity in the few-mode FBG sensor system is also proposed. In the end I will also investigate on polarization properties of highly multimode polymer FBGs and give some example of potential use of these grating sensors.

5.1 Properties of multi-mode FBGs

As it was mentioned many times before, the basic principle of FBG sensing is to measure the reflected wavelength spectrum and to track the FBG peak position. The reflected Bragg wavelength λ_B is defined by the phase-matching condition:

$$\beta_{l,m}^{f} + \beta_{l.m}^{b} = \frac{2\pi}{\Lambda_G}, \tag{5.1}$$

where $\beta_{l,m}^{f}$ and $\beta_{l,m}^{b}$ are the propagation constants of the forward and backward propagating modes, Λ_G is the pitch of the index modulation fringe pattern. and ***l*** and ***m*** are integer numbers, which determine the

particular LP_{lm} mode of propagation. The propagation constants depend on the refractive index profile of the optical fiber.

In birefringent fibers the refractive index is anisotropic and varies for different states of polarization. This leads to broadening and splitting (for highly birefringent fibers) of the reflected Bragg peak. For standard fibers as used here birefringence is relatively small [63], but, nevertheless any birefringence can slightly broaden the FBG peak and make it non-Gaussian, and thereby add to the polarization sensitivity of an FBG sensor.

The modal properties of a fiber also influence the properties of an FBG sensor. In particular more peaks are introduced when the fiber supports more modes and the power distribution among the different guided modes depends on the polarization state of the input light and the coupling, which enhances the effects of birefringence and adds to the polarization sensitivity.

Another factor is non-uniformity of the refractive index profile due to the FBG UV-writing process itself [64,65,66]. This effect is more significant for fibers with larger core diameters and the 1550nm fibers have a core diameter of about twice that of the 850nm fiber. Combining these factors we expect a higher polarization sensitivity and non-linearity of the response for 850 nm FBGs in few-mode 1550 nm fibers, as compared to 850 nm FBGs in single-mode 850 nm fibers.

The interrogator is also a very important part of a sensing system and quite often its influence is underestimated. The most common and commercially available FBG interrogators contain single-mode fibers. Let us consider what happens when the single-mode fiber from the interrogator is connected to the multi-mode fiber (MMF) with a fiber Bragg grating:

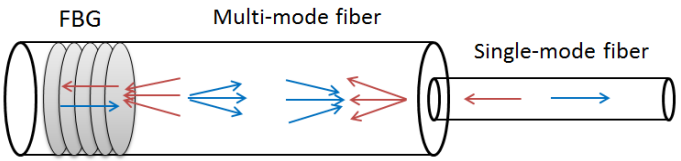

Figure 5.1. Multi-mode to single-mode coupling: red represents forward propagating light; blue represents FBG reflected light.

The light from the broadband light source in the interrogator propagates through the single-mode fiber (red arrow in Fig. 5.1). When the light passes through the coupling point multiple modes will be excited in the MMF. The FBG in the MMF will introduce coupling between the modes, not only between the same mode (e.g. LP_{01}-LP_{01} or LP_{11}-LP_{11}), but also between different modes (LP_{01}-LP_{11}). For each reflected Bragg wavelength several modes are supported in the MMF. However, when the reflected Bragg wavelengths are coupled back into the SMF, only the fundamental mode can propagate in the single-mode fiber [58]. The detected output spectrum results from mode re-coupling back into the SMF from the MMF, through which both the fundamental and HOMs of the MMF can excite the fundamental LP_{01} mode of the SMF. This fact leads to a higher polarization sensitivity of FBG sensors in MMFs than in SMFs.

Typical reflection spectra from a single-mode FBG and a few-mode FBG are shown in Fig. 5.2. The FBGs were made by Advanced Optics Solution (AOS) in an 850 nm step-index SMF with core diameter 5.4 μm (Fig. 5.2(a)) and in a standard 1550 nm step-index SMF with core diameter 8.2 μm (Fig. 5.2(b)), which is a few-mode fibre for 850 nm light (the FMF).

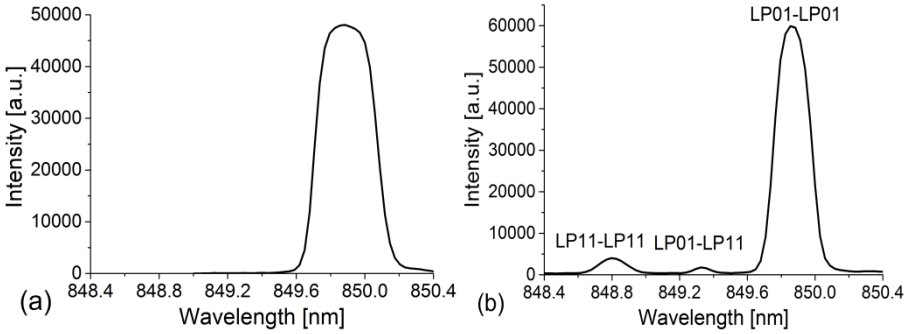

Figure 5,2. (a) Single-mode reflection spectrum, (b) Few-mode reflection spectrum

The normalized frequency $V=(\pi d/\lambda)*NA$ [67], where d is the core diameter, is 3.7 at 850 nm for the FMF with NA=0.14 (according to standard SMF-28 specifications). This means that the fiber supports up

to 4 modes (HE_{11}, TE_{01}, TM_{01}, and HE_{21}), corresponding to the LP_{01} and LP_{11} modes [68]. As expected, for the FBG in the FMF we measured three reflected peaks at 849.88 nm, 849.33 nm, and 848.77, as shown in Fig. 5.2(b), corresponding to LP_{01} self-coupling, LP_{01}-LP_{11} cross-coupling, and LP_{11} self-coupling, respectively.

5.2 Static experiment

The first experiment was carried out to measure the polarization sensitivity of the selected fiber Bragg gratings. The experimental setup is shown in Fig. 5.3.

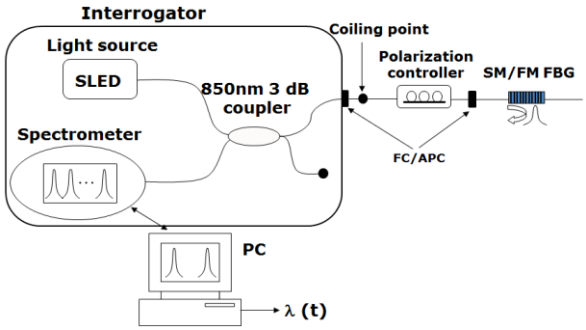

Figure 5.3. Experimental configuration: The fiber with the FBG is FC/APC connected to a polarization controller and the 850 nm interrogator containing 850 nm single-mode fibers.

The fiber with the grating was connected to a manual fiber polarization controller from Thorlabs, which uses stress-induced birefringence produced by wrapping the fiber around three spools to alter the polarization of the transmitted light. The fiber in the controller was selected to match the FBG fiber. The controller was connected to a commercially available interrogator from Ibsen Photonics (I-MON 850 FW). The wavelength range of the interrogator goes from 824 to 857 nm using a detector with 1024 pixels. All fibers inside the interrogator are 850 single-mode fiber with 5.4 μm core diameter. The position of the controller was selected to simulate the situation when birefringence and polarization scrambling occurs between the FBG and the interrogator. During the experiment we went continuously through all polarization states changing the polarization

between linear, circular and elliptical. The FBG spectra were measured and saved with a frequency of 1783 Hz.

Since the measured peak may change shape during the experiment, high robustness is required to fit the peak without significant fitting errors, which may influence the results. We selected a novel dynamic gate algorithm (DGA) for this purpose, which was described in detail in the previous chapter. The algorithm uses a threshold determined detection window and center of gravity algorithm with bias compensation and avoids sudden shifts in the fitted wavelength. The DGA threshold was set at 25% of the maximum. In order to be sure that the system performance is enough to detect small deviations the wavelength fit resolution (WFR) has been calculated as the standard deviation between the measured data and their best fit. The WFR was found to be 0.05 pm for given fibers and given algorithm. All fibers were fixed to the table during the experiments to ensure that the polarization was only changed by the controller.

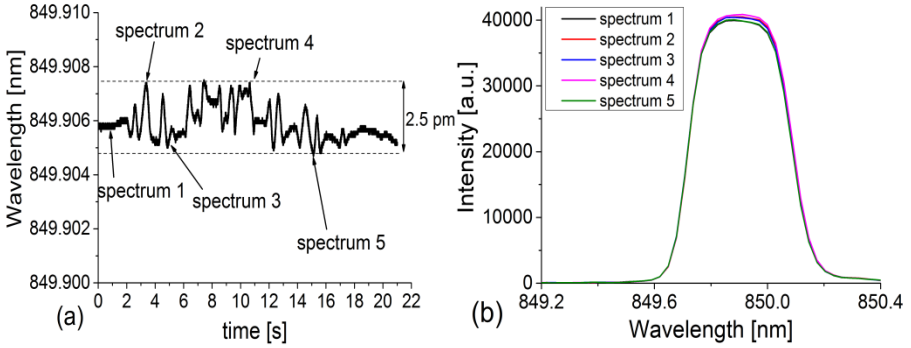

Figure 5.4. Polarization sensitivity of the FBG in the SMF: (a) wavelength change versus time, (b) spectral profile at the indicated 5 points.

Figure 5.4(a) shows the polarization sensitivity of the FBG inscribed in the 850 nm SMF, when continuously changing the polarization through all types (linear, circular, elliptical) and states of polarization several times. The polarization dependent wavelength (PDW) shift, which is the overall peak-to-peak amplitude deviation, is around 2.5 pm. Figure 5.4(b) shows how the single-peak FBG profile is varying during the measurements. Only small changes in the profile and the peak amplitude (~2%) can be detected.

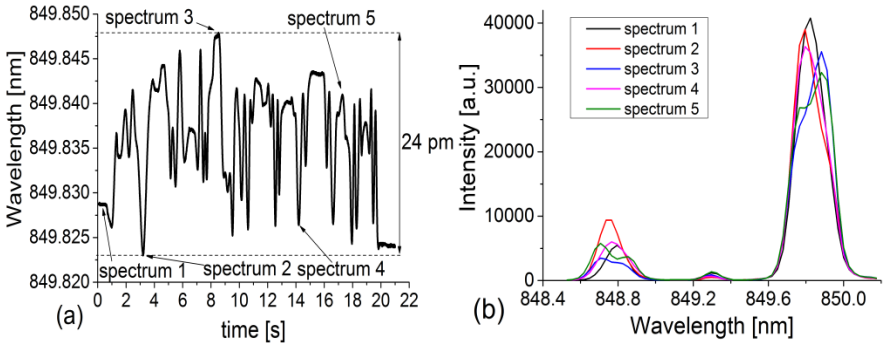

Figure 5.5. Polarization sensitivity of the FBG in the FMF: (a) wavelength change versus time, (b) spectral profile at the indicated 5 points.

Figure 5.5 shows the polarization sensitivity of the main (LP_{01}-LP_{01} self-coupling) FBG peak inscribed in the FMF. The PDW is now much higher, reaching almost 24 pm, and the 3-peak profile is changing dramatically with polarization.

Our results show that the FBG in the FMF cannot directly be used for high sensitivity sensor applications because the robustness to polarization is significantly degraded by the presence of the HOMs. This is important that it shows that the approximate linear response typically assumed in sensor demonstrations with FBGs in FMFs [13,61,62] is in fact not necessarily sufficiently linear, but has too high PDW to be used in accurate detection. This is one of the main points of our study.

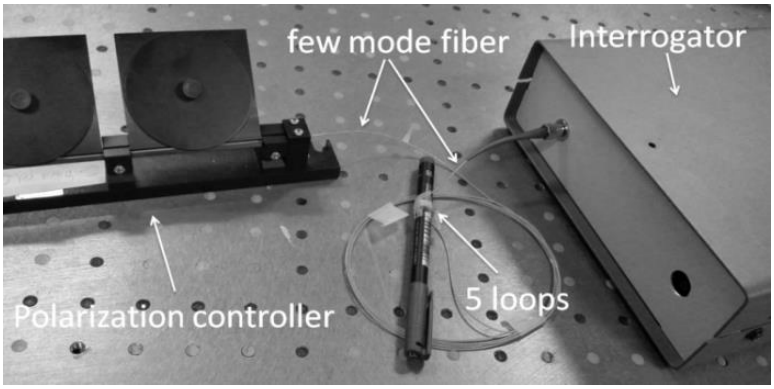

Figure 5.6. Loop-filter position.

However, it is well-known that simple coiling can strip off HOMs [69,70,71], but how would this alter the polarization stability of the

sensor? To investigate this we bent the FMF between the polarization controller and the interrogator as seen in Fig. 5.3. The bending was done by making 5 small loops of the FMF around 10 mm in diameter, as seen in Fig. 5.6.

The spectrum of FBG in the coiled FMF is shown in Fig. 5.7(b). The filter is seen to remove all HOMs from the spectrum, leaving only the fundamental mode. The intensity of the main peak slightly decreased compared to the uncoiled fiber: from 41000 a. u. to 34000 a. u., which is around 17% or 0.8 dB. It shows that coiling can induce some loss, however, in our case, these losses are relatively small and, thus, have no influence on the system performance. Figure 5.7(a) shows the polarization sensitivity of the main FBG peak when the loop filter is introduced in the test setup. The PDW is around 2.5 pm, which equals the value for the FBG in the SMF. The profile is stable and doesn't change during the experiment.

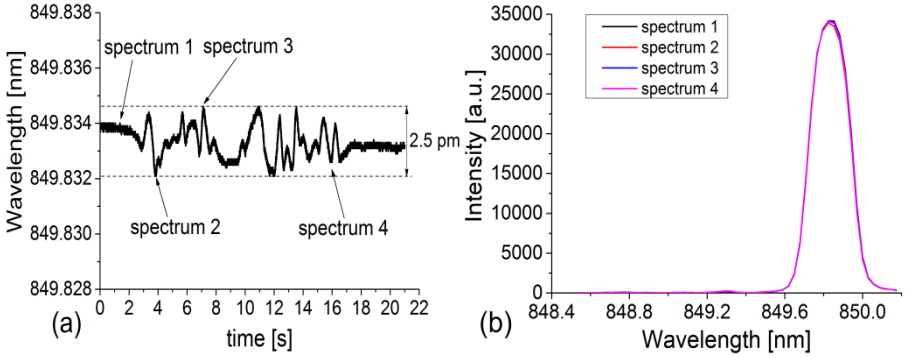

Figure 5.7. Polarization sensitivity of the FBG in the FMF with 5 coils, 10 mm diameter: (a) wavelength change versus time, (b) spectral profile at the indicated 4 points.

5.3 Dynamic experiment

The static measurements showed that when coiled, the FBG sensor using a standard cheap 1550 nm FMF, could perform equally as well as the 850 nm SMF. However, this needs to be verified in real dynamical sensor experiments. For these experiments we used the same interrogator and the same fitting algorithm as in the previous section.

A. Temperature measurements

In the first experiment we compare the temperature performance of the FBG sensors. An FBG was installed and fixed inside an oven together with a thermocouple. The temperature was increased to 115 °C, then after 30 minutes the oven was turned off and the measurement began. The FBG spectrum and the temperature from the sensor were recorded simultaneously every 20 seconds during 8 hours, as the temperature inside the oven dropped down from 115 to 55 °C. This free cooling process allows us to avoid turbulence and rapid temperature changes inside the oven.

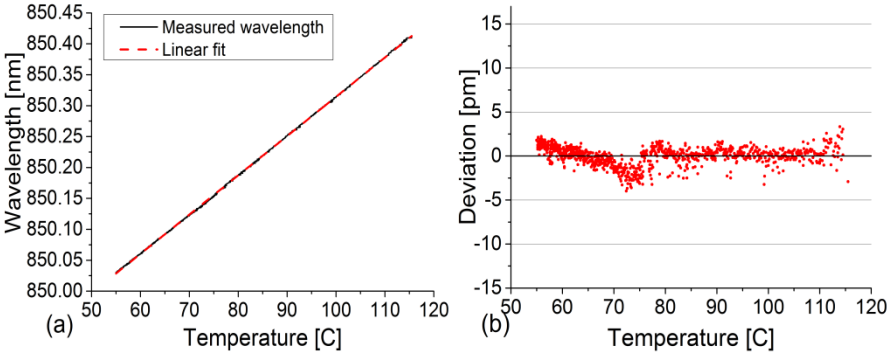

Figure 5.8. SMF FBG temperature test, (a) wavelength vs. temperature, (b) Deviation from the linear fit.

Figure 5.8 shows the linearity of the FBG sensor in the SMF. As can be seen from Fig. 8(b) the peak-to-peak deviations from the linear fit is less than 5 pm and the temperature sensitivity is 6.35 pm/°C with a standard deviation of about 1.09 pm.

Figure 5.9 reports the fitted wavelength of the FMF main peak as a function of temperature. In contrast to the SMF FBG sensor the FMF FBG sensor is not linear and has a significant peak-to-peak deviation of up to 25 pm. The temperature sensitivity is 6.77 pm/°C with a standard deviation of about 6.87 pm. This fiber sensor is definitely not suitable for precise temperature monitoring.

However, when the loop-filter was installed between the FBG and the interrogator (same position as in the previous section), the linearity of the FMF FBG sensor was significantly improved (see Fig. 5.10)

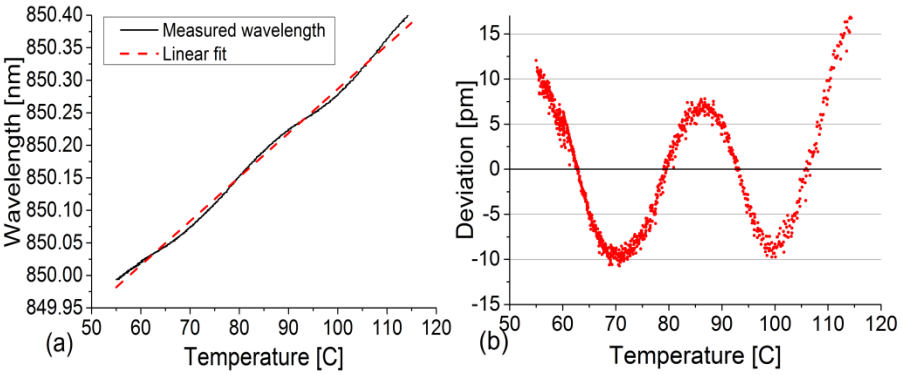

Figure 5.9. FMF FBG temperature test, (a) wavelength vs. temperature, (b) Deviation from the linear fit.

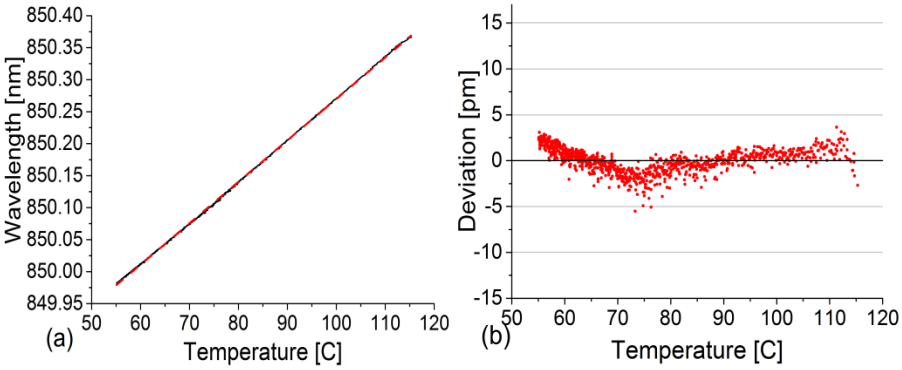

Figure 5.10. Coiled FMF FBG temperature test, (a) wavelength vs. temperature, (b) Deviation from the linear fit.

The peak-to-peak deviation and the standard deviation are 6 pm and 1.34 pm, respectively. The overall performance and linearity are almost the same as for SMF FBG sensor. These results confirm that adding the loop-filter restores the accuracy and sensitivity and makes the FMF FBG temperature sensor applicable to also real dynamical sensor applications.

B. Strain measurements

Strain monitoring is another important application of FBG-based sensors. Static characterization of FBG sensors in terms of axial strain sensitivity is done by fixing the FBG in two points to translational stages, stretch the fiber and then recording the wavelength and applied

strain in a number of discrete points [1]. Here we would like to have a continuous recording of the accuracy of the sensor response in order to detect possible small deviations from linearity. We therefore perform dynamical measurements using a shaker (Brüel & Kjær Type 4810) controlled by a waveform generator as shown in Fig. 5.11, which is a standard way of doing such a characterization [72].

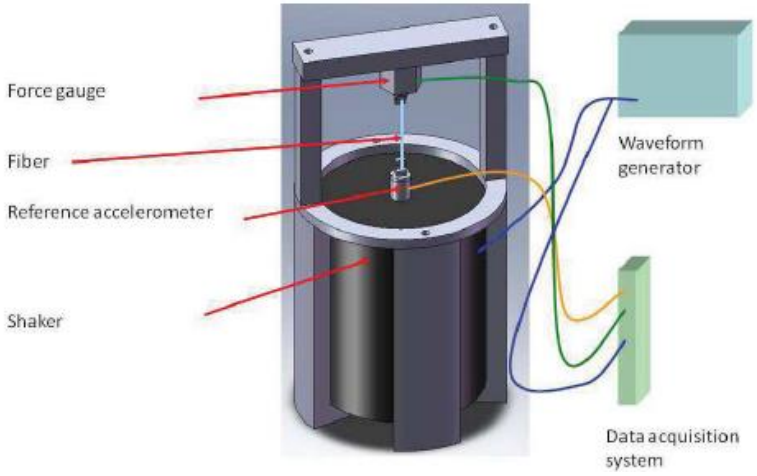

Figure 5.11. Strain measurement setup.

The fiber was fixed in on one end to the shaker and the other end was fixed to a force gauge. A waveform generator was used to drive the shaker to oscillate between 0.2% and 0.42%. The fibers were pre-strained before being elongated in order to make sure it was in the linear regime and never loose. We applied a sinusoidal signal with a frequency of 2 Hz to the shaker. Assuming elastic deformation and Hooke's law the wavelength-time dependence is given by

$$\lambda(t) = \lambda_0 + A\sin(\pi t + \phi), \tag{5.2}$$

where $\boldsymbol{\lambda 0}$ is an average wavelength, and $\boldsymbol{A}$ and $\boldsymbol{\varphi}$ are the amplitude and phase of the oscillation, respectively. The wavelength-time curve for the SMF FBG sensor is shown in Figure 5.12.

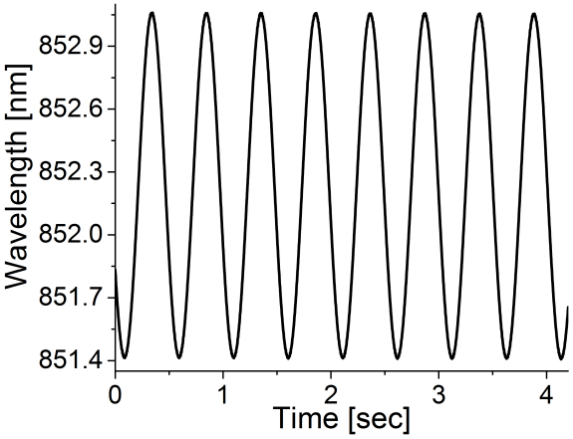

Figure 5.12. SMF FBG wavelength vs time when a sinusoidal strain was applied with a frequency of 2 Hz between 0.2% and 0.42%..

In this experiment the FBG spectra were measured and saved with a frequency of 1783 Hz and then the wavelength-time curves were fitted with the function from Eq. (5.2).

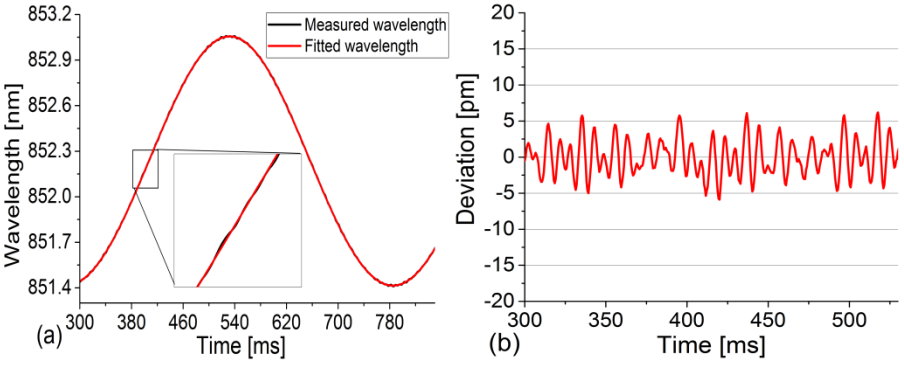

Figure 5.13. SMF FBG strain test: (a) wavelength-time curve, (b) deviation from the fit.

Figure 5.13 shows that for the SMF FBG sensor the strain response is highly linear, i.e., the response follows accurately the predicted sinusoidal response. As can be seen from Fig. 5.13(b) the total peak-to-peak deviations from the selected fit is around 10 pm.

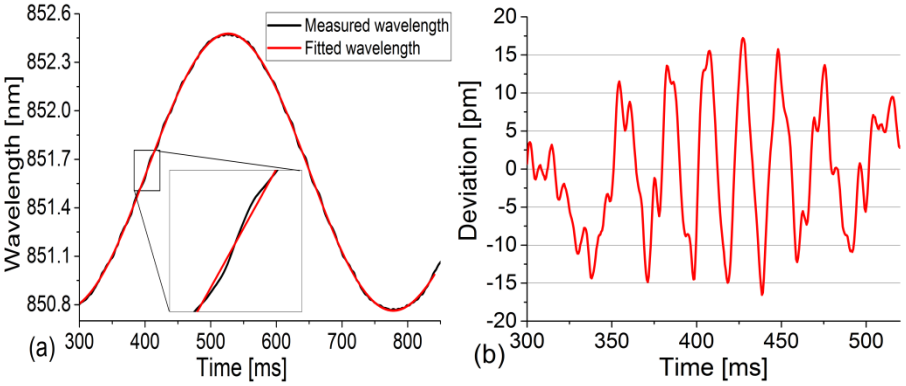

Figure 5.14. FMF FBG strain test: (a) wavelength-time curve, (b) deviation from the fit.

Figure 5.14(a) shows the fitted wavelength of the FMF FBG main peak as a function of time. Clearly, the presence of HOMs has a strong influence on the linearity of the response, which now does not match the expected sinusoidal function and has a significantly higher peak-to-peak deviation of up to 32 pm (see Fig. 5.14(b)). This fiber sensor is not suitable for precise strain monitoring.

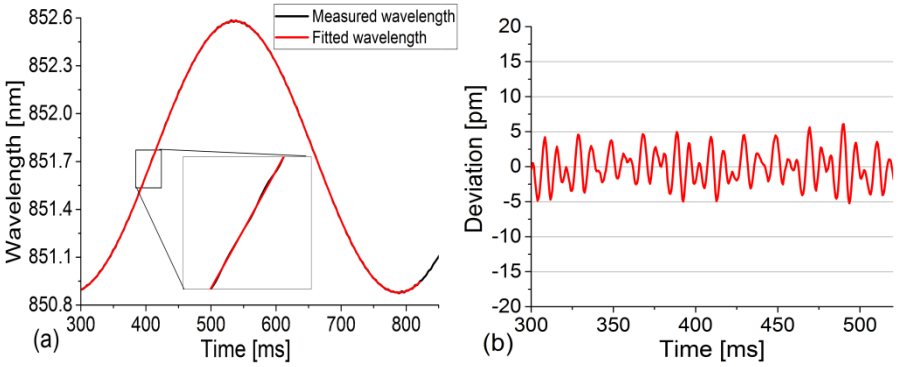

Figure 5.15. FMF FBG strain test with the loop-filter: (a) wavelength-time curve, (b) deviation from the fit.

Figure 5.15 shows how the loop-filter can improve the wavelength-strain linearity. When the loop-filter was installed between the FBG and the interrogator, the main FMF FBG peak demonstrated the same performance as the SMF FBG, i.e., the peak-to-peak deviation was decreased from 32 pm to 10 pm.

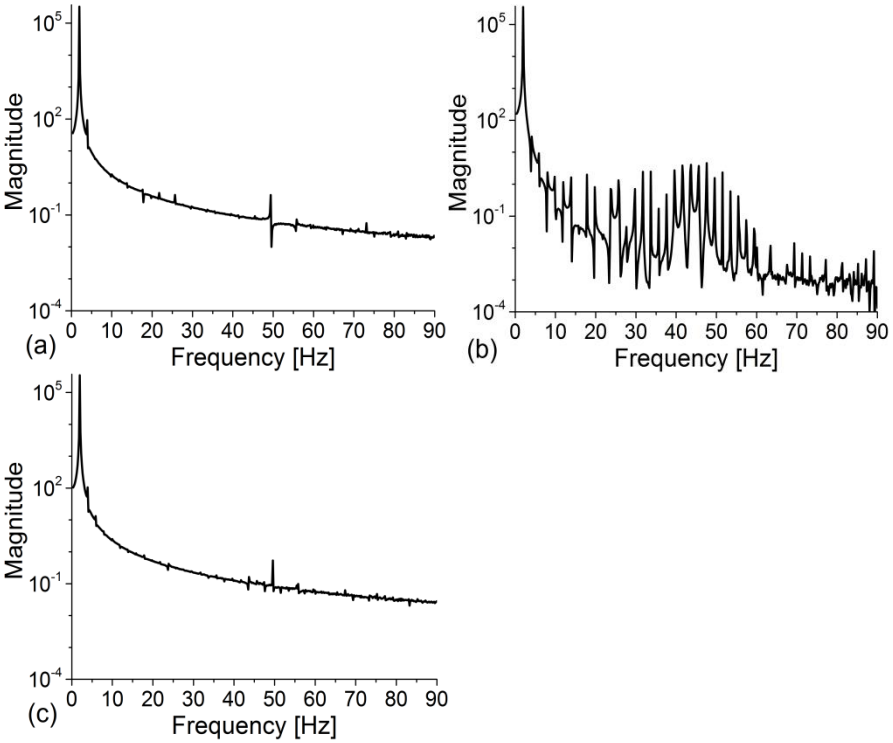

Figure 5.16. FFT of the measured wavelength-time relation when a sinusoidal strain was applied with a frequency of 2 Hz for (a) the SMF FBG (b) the FMF FBG, and (c) the coiled FMF FBG.

Figure 5.16 shows an FFT of the measured sensor response. The frequency analysis further highlights the poor performance of the uncoiled multi-mode FBG sensor in that it shows the presence of high frequencies for the FMF FBG compared to the SMF FBG sensor. However, when the loop-filter was installed, the FFT picture of the coiled FMF FBG becomes again almost equal to the SMF – the undesired frequencies vanish. The magnitudes of the high frequencies introduced by the HOMs are relatively small compared to the main peak of 2 Hz (about 10^5 times smaller). However, when the FMF FBG sensor is used to detect small variations of strain, as for example in accelerometers or acoustic microphones [38], these high frequencies can potentially distort the measured signal, and thus it is very important that simple coiling can remove them.

Table 5.1. Polarization sensitivity.

	SMF FBG	FMF FBG	FMF FBG with filter
PDW, pm	2.5	24	2.5
Temperature test deviation, pm	5	25	6
Strain test deviation, pm	10	32	10

A comparison between the performance of the 3 sensors is given in Table 5.1. As can be seen, both the linearity and polarization sensitivity of the SMF FBG and FMF FBG with the loop-filter are almost identical.

5.4 Conclusions

In the work presented in this chapter we have evaluated how detrimental the influence of higher-order modes is to the polarization stability and the linearity of the strain and temperature response of an FBG sensor. We have done this by comparing the performance of a few-mode 850nm FBG sensor using a standard 1550nm telecom fiber to a strictly single-mode 850nm FBG sensor system using an 850 nm single-mode fiber.

Our results show that the polarization stability and the linearity of the response degrade so much due to the presence of the higher-order modes, that in practice the sensor would not be usable for high-precision measurements, in contrast to what have been concluded in several earlier investigations [60, 73].

However, we have demonstrated that using the well-known technique of simple coiling of the few-mode fiber one can regain the single-mode performance of the multi-mode sensor system. These experiments therefore demonstrate that 850 nm FBG sensor systems can indeed in practice be based on low-cost 1550 nm telecom fibers, despite these being multi-mode at 850 nm.

Chapter 6

Spectrometer-based interrogators: errors and solutions

The basic principle of FBG sensing is to measure and extract information wavelength-encoded in the Bragg reflection. One of the most important parameters is precision of the measured information or, in other words, the difference between the real and the measured information. In the perfect world this difference is equal to zero and we always get what we have. Unfortunately, in the real life we always have some deviations. In the previous chapter I analyzed deviations, which come from the sensor itself. I showed that due to the presence of the high order modes the polarization stability and the linearity of the strain and temperature response of an FBG sensor degrade so much that the sensor might not be usable for high-precision measurements.

In this chapter I will deeply analyze and investigate errors, which are typical for spectrometer-based interrogators: undersampling, grating internal reflection, photo response non-uniformity, pixel crosstalk and temperature and long term drift. For this purposes I will use a commercial state-of-the-art spectrometer-based interrogator

manufactured by Ibsen Photonics (I-MON 256 USB). I will also propose several solutions and improvements to some of the errors.

6.1 Accuracy

To compare the measured wavelength by the interrogator and the real wavelength of the input light we carried out an experiment where we used a tunable laser source with the Gaussian-shaped peak with a peak width much narrower than the interrogator resolution. The laser wavelength was varied from 1525 nm to 1570 nm with a step of 25 pm. The output from the laser was split into two paths, one path was connected to the spectrometer and the second one was connected to a high precision wavemeter (Figure 6.1). Spectra were measured by the interrogator and then Gaussian fitting (since the laser output is Gaussian shaped and the interrogator has a Gaussian shaped response) was applied. The data captured by this experiment is also used for calibration, so the interrogator is newly-calibrated and one can be sure that there are no errors, which occur due to bad calibrations.

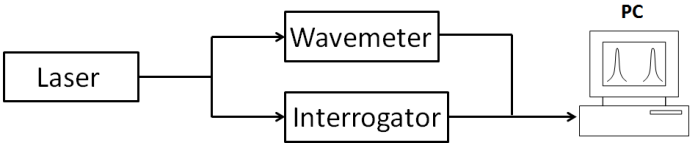

Figure 6.1. Experimental configuration.

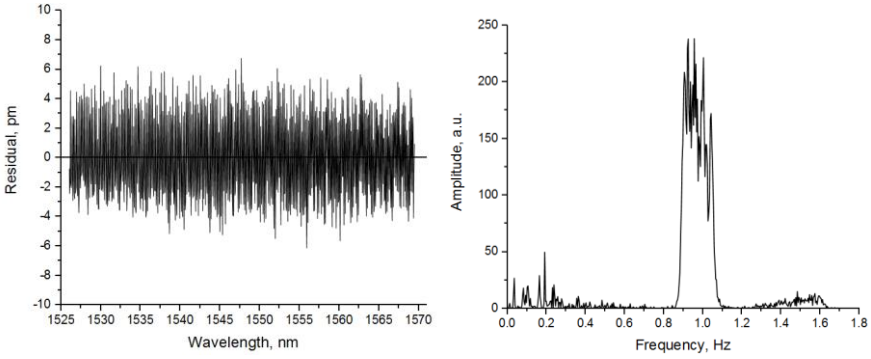

Figure 6.2. (a) left – difference between the measured and reference wavelength; (b) right – Fourier transform of the residual.

Figure 6.2 (a) shows the residual, which is the difference between the fitted wavelength and the referenced one measured by the wavemeter. At first one can say that the residual looks very noisy and randomly. However, on the Fast Fourier transform image (Figure 6.2 (b)) one can clearly see some peaks, which indicates that noise has periodical structure. The highest peak has a frequency of 1 Hz and here X axis unit is 1/pixel, so it means that the period of the highest noise is 1 pixel. This noise is called undersampling noise. Other periodical noise with frequencies around 0.03-0.2 Hz and period of 5-10 pixels comes from the grating internal reflection.

6.1.1 Grating internal reflection

Ibsen uses transmission diffraction gratings in their products. Transmission diffraction gratings have many advantages: high environmental stability; low-temperature expansion and sensitivity; high diffraction efficiency combined with high dispersion; homogenous diffraction efficiency values over the spectral band and others. However, since the gratings are made by fused silica, light can internally reflect. It is illustrated in Figure 6.3 (a). Small portions of light according to Fresnel equations are internally reflected from the grating edges and then are sent towards to the detector (blue arrows in Fig. 6.3 (a)).

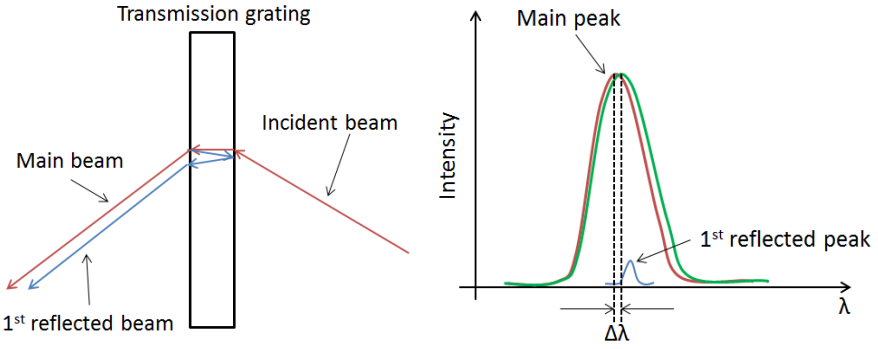

Figure 6.3. (a) left – transmission grating internal reflections (top view); (b) right – difference in the peak positions on the detector.

Due to small angle between grating surfaces and imperfection of other optical components these two beams (main beam and 1st reflected) are not focused at the same position on the detector (see Figure 6.3 (b)). Since the detector reads the sum of these two portions the result (green color) is slightly shifted compared to the main beam position (red color), see $\Delta\lambda$ in Figure 6.3 (b). Now let's take into account that these two beams have the same wavelength – it means that these beams interfere with each other. Depending on the phase difference the effect of the 1st reflected peak can be positive or negative. The phase difference depends on the wavelength, thus, the difference in wavelength position is a periodical function of wavelength.

Besides the first reflected beam, there is also 2nd reflected and so on, but even the first reflected beam has very small intensity compared to the main beam, so that high order reflections can be neglected. There are several ways of how one can decrease the effect of the described internal reflection. The first method is to use special antireflection coatings and highly suppress intensities of the internally reflected beams. The second method is to use transparent wedges, which introduce an angle between the main and reflected beams and deflect out of the detector. Figure 6.4 shows the principle.

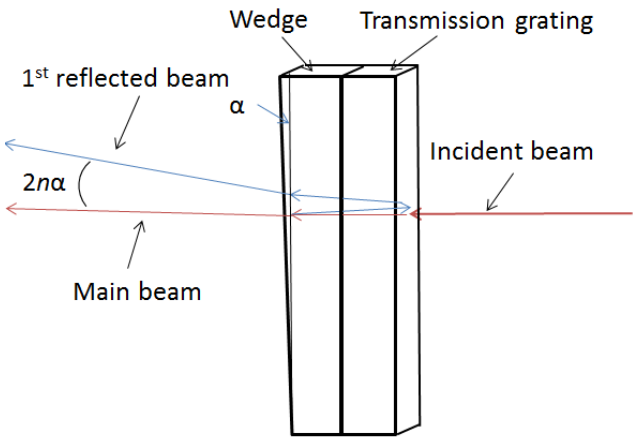

Figure 6.4. Wedge deflection principle (side view).

If α is the wedge angle, then the angle between two beams is ***2nα,*** where n is the refractive index of the wedge material, which is fused silica. Knowing the interrogator geometry I was able to find the optimum wedge angle when the 1st reflected beam was focused out of the detector. Zemax software was used to do all calculations and simulations. With wedge angle equal to 0.33 degree (or 20 arc minutes) the distance between the beams is more than 0.73 mm, which is a few times bigger than the detector height (0.25 mm). Figure 6.5 shows the interrogator optical scheme with wedges.

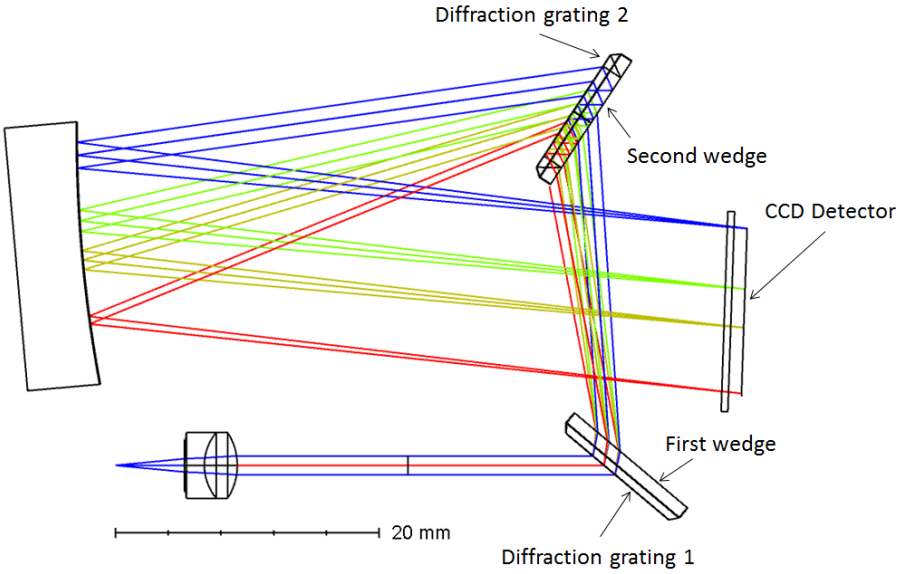

Figure 6.5. I-MON USB 256 2D optical layout with wedges.

In order to prove my assumption, I carried out an experiment. In the experiment I used the wedges made by fused silica – the same material used for grating production. The wedges were glued to the gratings by UV curing glue, which is almost 100% transparent for visible and IR range. All transmission gratings used in this experiment were made without AR coating – this should emphasize the effect described above and also AR coating may interact with glue, so I decided to avoid using AR coating in this experiment. Figure 6.6 shows the residual measured without wedges (no AR coating on the gratings).

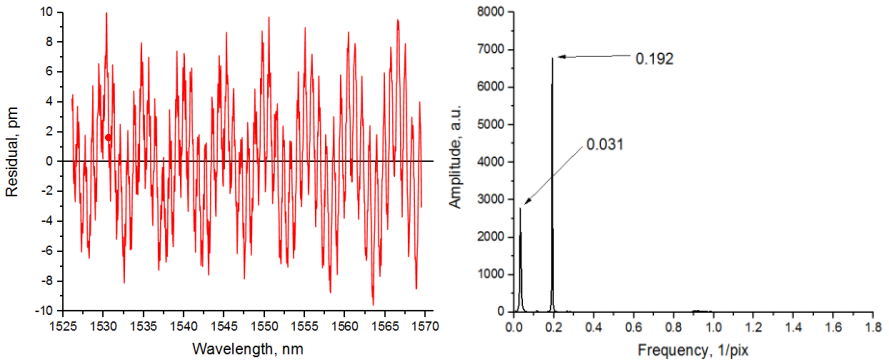

Figure 6.6. (a) left – difference between the measured and reference wavelength; (b) right – Fourier transform.

At FFT image one can clearly see 2 strong frequencies of 0.031 and 0.192 1/pix. We observe two frequencies because the interrogator has 2 diffraction gratings one after another. Figure 6.7 shows the residual when the wedge was glued to the second grating (GW configuration). As can be seen, only one component at 0.192 Hz remains, the other frequency of 0.031 Hz was deleted by the wedge. This proves that the frequency of 0.031 Hz comes from the second grating. The next step is to glue the wedge to the first grating only. If the assumptions made before are correct then the wedge glued to the first grating should remove frequency of 0.192 Hz.

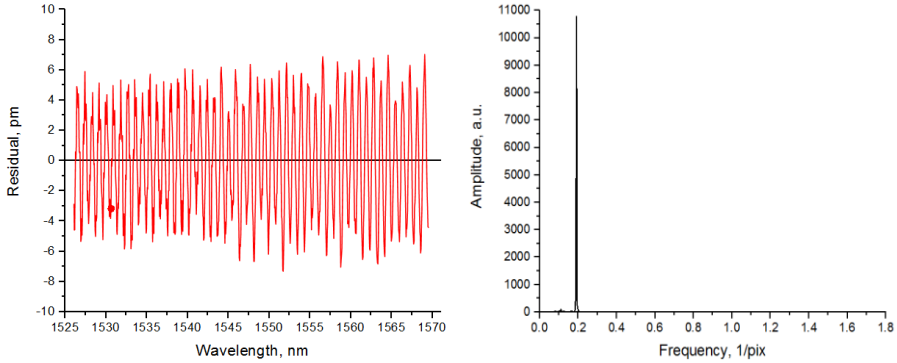

Figure 6.7. GW configuration: (a) left – difference between the measured and reference wavelength; (b) right – Fourier transform.

Figure 6.8 proves the assumption – the wedge removes higher frequency coming from the first grating.

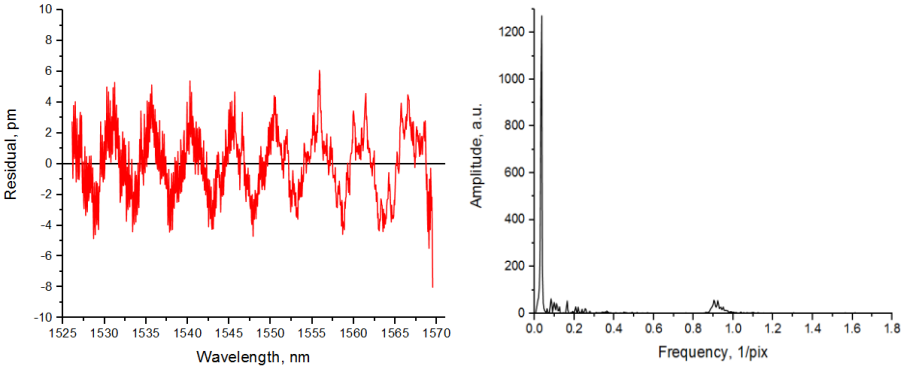

Figure 6.8. WG configuration: (a) left – difference between the measured and reference wavelength; (b) right – Fourier transform.

Finally, figure 6.9 shows results when two wedges were glued to both gratings (WW configuration). In comparison with Figure 6.6, one can clearly notice that both frequencies were eliminated and the residual were decreased from ±10 pm to ±2 pm. The results prove the initial assumption of origin of frequencies caused by grating internal reflection and show how one can improve the precision of transmission grating based spectrometer. The other way of suppression of these frequencies is, as was mentioned before, to decrease the amount of internally reflected light by use special antireflection (AR) coatings.

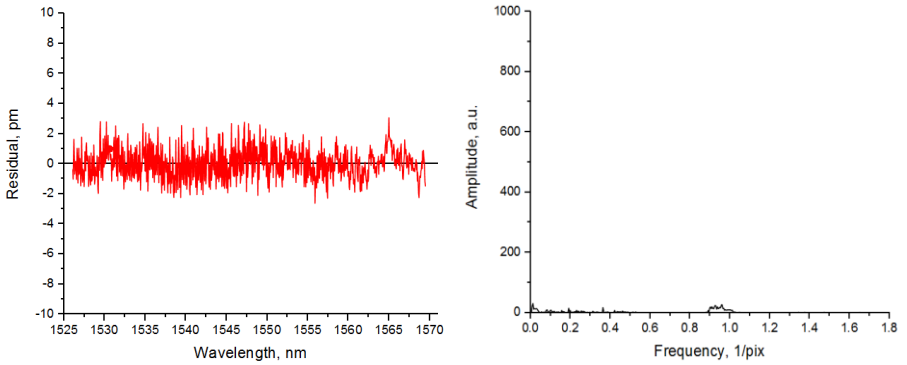

Figure 6.9. WW configuration: (a) left – difference between the measured and reference wavelength; (b) right – Fourier transform.

At Ibsen Photonics several layers of coating are used to suppress unwanted ripple and noise coming from gratings. Significant progress in grating design has been made over last 2 years. Figure 6.10 shows the residual measured with new gratings where the grating design was optimized to suppress unwanted internal reflection.

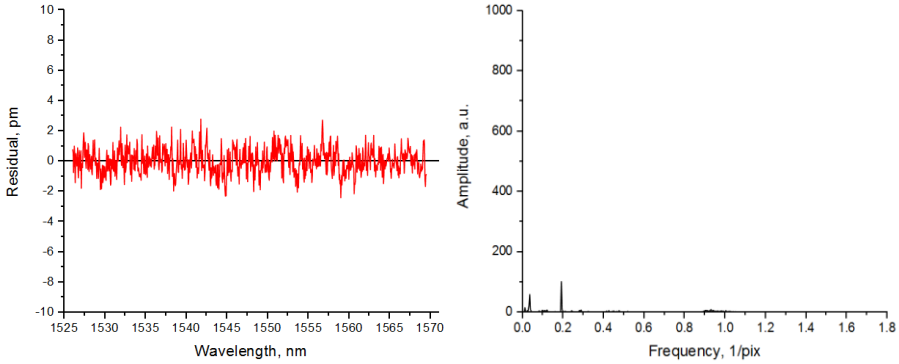

Figure 6.10. New gratings: (a) left – difference between the measured and reference wavelength; (b) right – Fourier transform.

One can still notice same two frequencies, so this method doesn't remove it completely compared to the wedge approach. However, the amplitude of the noise is 10-20 times smaller compared to the uncoated gratings and the effect of the internal reflection is negligible – the residual amplitude is compared to the one, which was obtained with 2 wedges.

6.1.2 Undersampling

Another component on Figure 6.2 (b) has a frequency of 1 Hz so its period equals to 1 pixel. This noise is called undersampling and comes from the fact that the measured spectrum is sampled with a finite sample step, for spectrometer-based interrogator usually given by the pixel pitch in the diode array. Continuous distribution of the energy along wavelength axis becomes discrete and then is decoded by using fitting algorithms. When "the sampling frequency" is too low the initial spectrum cannot be completely reconstructed – the same effect happens when one samples a bandpass-filtered signal at a sample rate below its Nyquist rate.

Figure 6.11 shows simulations of how a Gaussian-shaped signal with full width on half maximum (FWHM) about 16 um is sampled with three different sample pitch: 16 um, 7.5 um and 5 um. Each image contains 3 curves, which indicate different peak position relative to the sample grid. It can be clearly noticed that when the sampling pitch is compared to the FWHM of the peak (Figure 6.11 (a)), the image measured by the detector contains much less information and distorts much more compared to the case when the pitch size is 5 um (Figure 6.11 (c)).

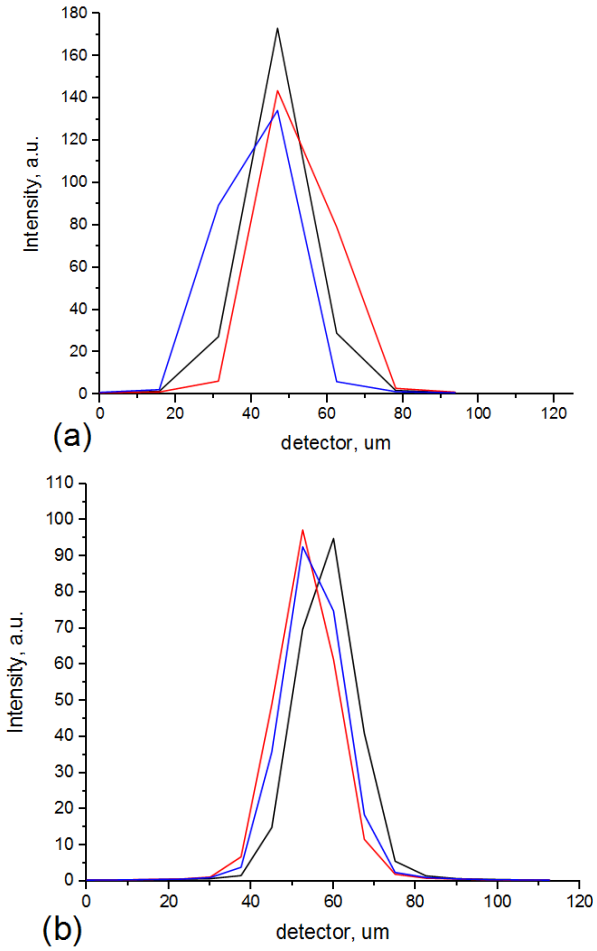

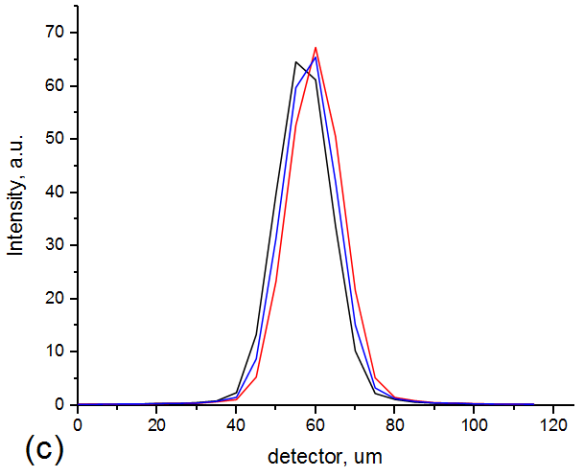

Figure 6.11. Gaussian-shaped signal sampled with different pitch size: (a) – 16 um; (b) – 7.5 um and (c) – 5 um.

By applying Gaussian fitting one can "recover" initial signal and calculate the center wavelength and the FWHM. The calculated FWHM for 3 different pitch sizes is 19.3 um, 16.7 um and 16.2 um for sample pitch of 16 um, 7.5 um and 5 um, respectively. Thus, too high sample step leads not only to higher peak distortion and higher undersampling noise but also to peak broadening and increasing of the calculated optical resolution. The main parameter is the ratio of the FWHM to the pitch size. It has been found [74] that undersampling is negligibly small when the FWHM is more than 2.8 pixels (samples).

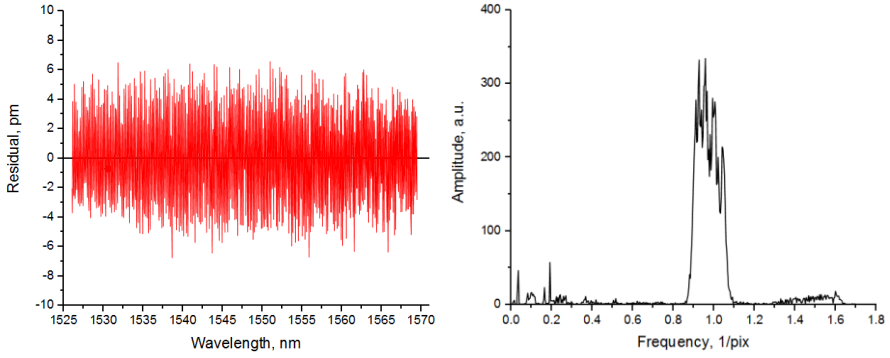

Figure 6.12. Gaussian fitting: (a) left – difference between the measured and reference wavelength; (b) right – Fourier transform.

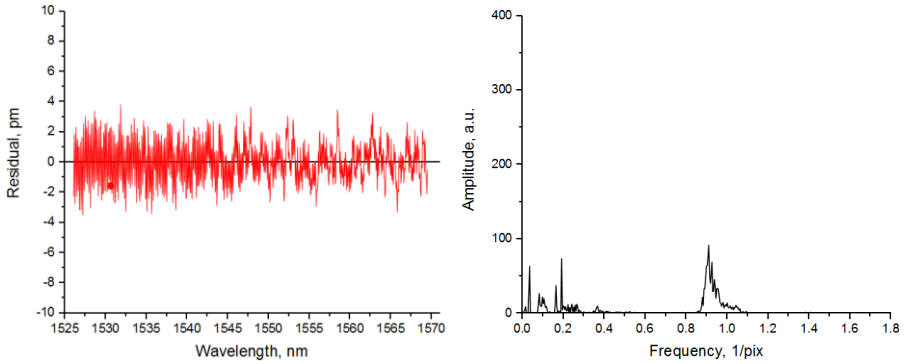

Figure 6.13. DGA fitting: (a) left – difference between the measured and reference wavelength; (b) right – Fourier transform.

I also found that the undersampling noise is sensitive to the fitting algorithm used to calculate the wavelength position. Gaussian fitting always demonstrates higher undersampling noise compared to center of gravity based techniques, such as Dynamic Gate algorithm (DGA).

Figures 6.12 and 6.13 show the difference between the Gaussian fitting algorithm and DGA used to calculate the measured wavelength and then to find the residual (the same method as in the experiment described at the beginning) on a commercially available interrogator. In this example the FWHM of the peak was 1.3 pixels in average, which led to quite strong undersampling, especially with the Gaussian fitting. When the algorithm was changed to the DGA the amplitude of the undersampling error decreased several times – from 300 to 100 a.u. (see Fig. 6.12 and 6.13 (b)). For the next experiment I used the interrogator from the previous section with wedges glued to both diffraction gratings. The FWHM was 1.9 pixels in average. Figure 6.14 and 6.15 show how by only changing the fitting algorithm one can decrease the residual and increase the precision. Since the FWHM value was higher (1.9) compared to the previous value (1.3) even with the Gaussian fitting the residual is not as big and equals to ±2 pm, by changing the fitting algorithm to the DGA one can improve this value to ±1 pm. Fourier transform images on Figures 6.14 and 6.15 show that the residual decreases due to the undersampling noise reduction. On Figure 6.15 (b) 1 Hz peak is completely gone. This is another advantage of the new fitting algorithm.

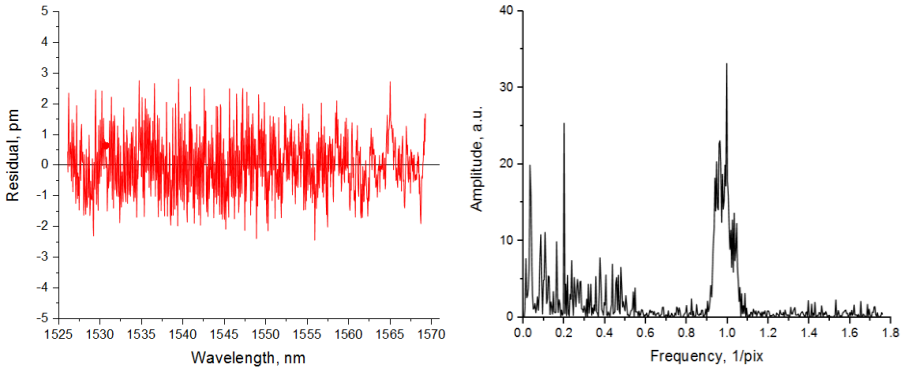

Figure 6.14. Gaussian fitting: (a) left – difference between the measured and reference wavelength; (b) right – Fourier transform.

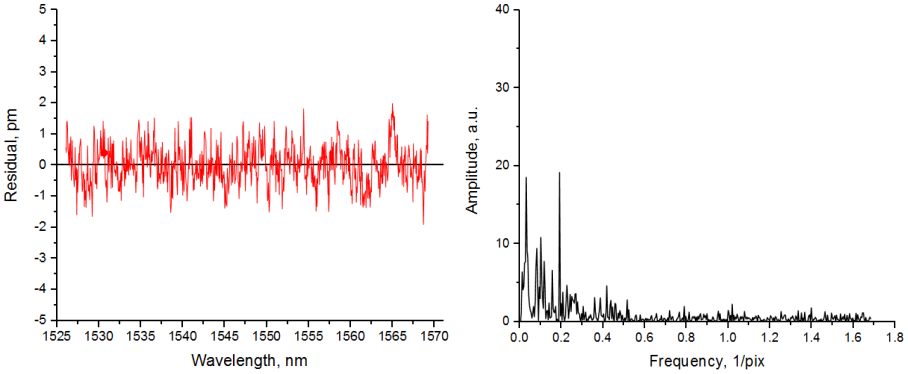

Figure 6.15. DGA fitting: (a) left – difference between the measured and reference wavelength; (b) right – Fourier transform.

In spite of the fact that by changing the fitting algorithm one may significantly decrease the undersampling noise, it is very important to take into account the pixel pitch during interrogator design, considering that the undersampling noise is negligibly small when the FWHM of the spot higher than 2.8 (or at least 2) pixels.

6.2 Photoresponse non-uniformity

Every Charge-Coupled Device (CCD) sensor is composed of an array of light-sensitive pixels. When uniform light falls on a camera sensor, each pixel should output exactly the same value. Small variations in cell size and substrate material result in slightly different output values. Thus, every pixel on a CCD array has a slightly different

response to a perfect flat-field illumination, and the difference in this response is defined as the CCD sensor's photo response non-uniformity (PRNU). The PRNU is defined by the following equation:

$$PRNU = \frac{(V_{MAX}^{OUT} - V_{MIN}^{OUT})/2}{V_{AVG}^{OUT}} \cdot 100\% \quad (6.1)$$

where V_{MAX}^{OUT}, V_{MIN}^{OUT} and V_{AVG}^{OUT} are the maximum, minimum and average output voltages, respectively.

Since PRNU is caused by the physical properties of the sensor itself, it is almost impossible to eliminate completely and is usually considered to be a normal characteristic of the sensor. Typical values of PRNU are around 5% for Hamamatsu and Sony CCD detectors. It means that difference between the maximum and the minimum output voltages are less than 10% of the average output voltage.

Since each pixel has its own response, the PRNU may distort the measured spectrum, introducing some uncertainties and errors in the wavelength position calculations. To investigate how the PRNU effects on the spectrometer performance I made LabView software, which simulates the PRNU. As input it takes a distribution of energy at the detector plane saved in a text file. Such distribution can be obtained in Zemax software by using Extended Diffraction Image Analysis (EDIA).

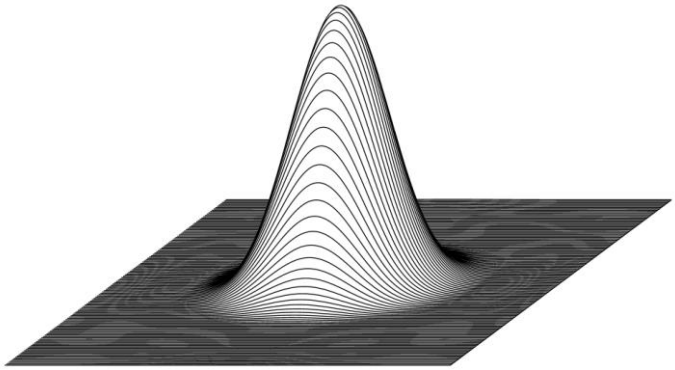

Figure 6.16. 2D distribution of intensity on the interrogator's detector plane calculated in Zemax using EDIA.

This feature can compute complex diffraction image properties from extended sources while accounting for the variation in the optical

transfer function (OTF) over the field of view. I took a Zemax file, which contains all optical components of the I-MON 256 USB interrogator and run the EDIA. As the result, I got a 2D distribution of energy on the detector plane including all aberration and diffraction effects (Figure 6.16).

Then the LabView software takes this text file and samples it, simulating detector pixel grid. The output of each pixel is a 2D numeric integral (I_1, I_2, ... I_{10}). Figure 6.17 schematically shows the principle.

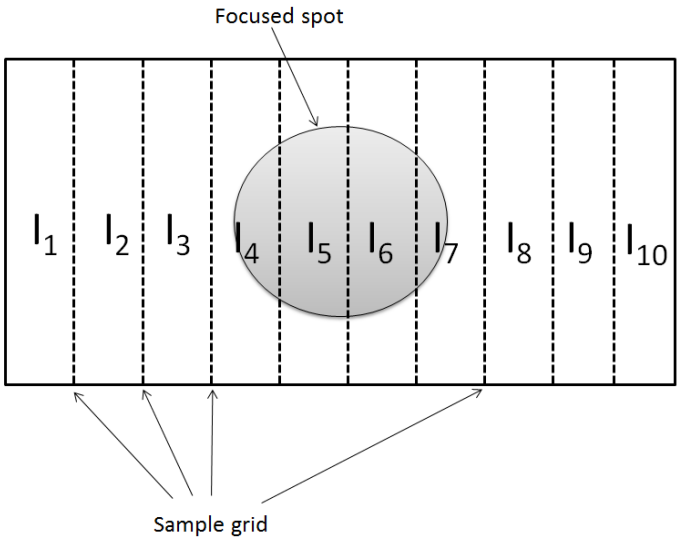

Figure 6.17. Scheme of the detector grid and focused spot sampling.

To simulate the PRNU a sequence of random values has been generated in a way that each pixel has its own coefficient ranging from 0.9 to 1. It corresponds to the PRNU of 5%. Then the output of each pixel (***In***) was multiplied by its own coefficient. To simulate different spot positions on the detector the grid was continuously shifted relative to the spot. The shift step was 1/100 of the pixel size and the total shift was 1 pixel. In order to get rid of the undersampling effect the grid pitch (which is virtual "pixel size") was set to make the FWHM equal to 4 pixels (around 1.9-2 in real device). Figure 6.18 shows how the 2D image from Fig. 6.16 looks when it was sampled and shifted along the detector axis.

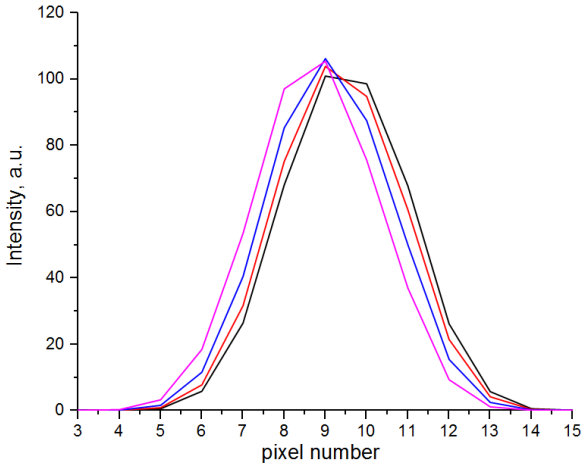

Figure 6.18. Spot shape changes depending on its position relative to the detector pixel grid.

Figure 6.19 shows the result of the simulation: the difference between the reference and the calculated spot position calibrated in pm (assuming 1550 nm wavelength). When the PRNU is off, so the numerical integrals are not multiplied by the PRNU coefficients, the residual is less than 0.01 pm, and is negligibly small. Situation changes when the PRNU is present – the residual reaches 1.5 pm peak-to-peak value. Figure 6.19 proves that the PRNU effects on the precision of the wavelength position determination. However, one can add that the PRNU error is not very big and usually less than 1 pm.

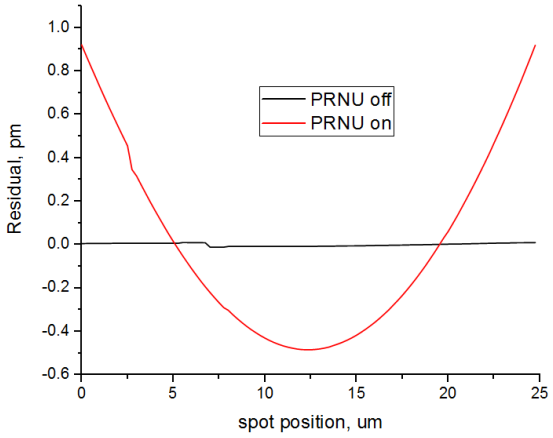

Figure 6.18. PRNU effect.

By using the same simulation software it is possible to see how the undersampling noise depends on the fitting algorithm. This issue was discussed in section 6.1.2. I found that the Gaussian fitting is more "sensitive" to undersampling than the DGA. I showed this by calculating residual using experimentally measured data. By using the simulation software it is possible to verify that assumption. Here, in contrast to the experimental data, we can exclude all other error sources – grating internal reflection, detector noise, PRNU etc.

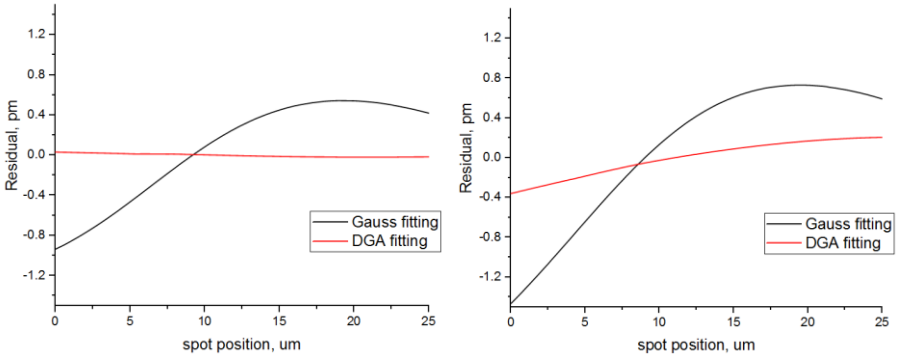

Figure 6.20. (a) left – comparison between Gaussian and DGA fitting, PRNU off; (b) right – comparison between Gaussian and DGA fitting, PRNU on.

To simulate the real detector grid, pixel size was set to 25 um, which corresponds to the pixel size on the Hamamatsu G11620 detector used in the interrogator, which was analyzed in Section 6.1.2. With this pixel size, the FWHM is 1.9 pixels, which also corresponds to the measured values.

Figure 6.20 (a) shows the residual calculated using LabView simulation software. Here PRNU is off. It can be clearly seen that the DGA fitting produce much less undersampling noise (<0.05 pm), whereas with the Gaussian fitting residual reaches 1.5 pm peak-to-peak value. When PRNU is ON (Figure 6.19 (b)), which corresponds to the real detector, the difference between the algorithms is almost the same.

Since the pixel response changes from pixel to pixel almost randomly, the PRNU noise is not periodic function as for example the undersampling is.

6.3 Pixel cross-talk

Another disadvantage of array detectors is pixel cross-sensitivity. During charge collection, electrons and holes in the detector bulk can diffuse laterally into neighboring pixels before they arrive at a pixel well. After collection, when the charge is stored in the collecting node, capacitive coupling between neighboring nodes will result in additional crosstalk.

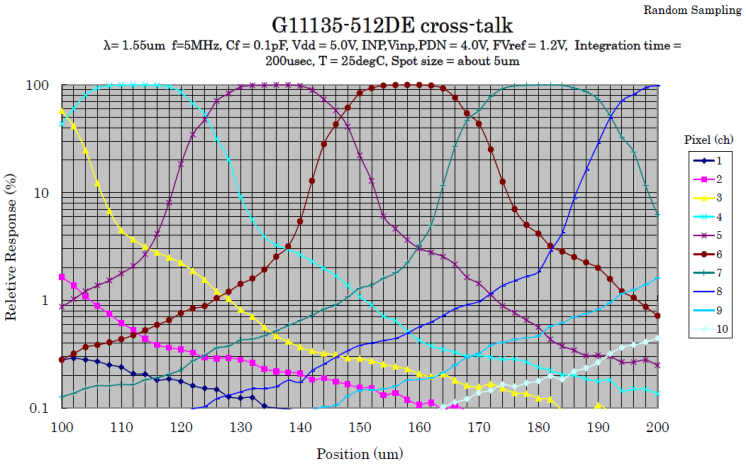

Figure 6.21. CCD cross-sensitivity (image source - Hamamatsu).

Crosstalk leads to blooming and broadening of the peak, which results in a reduction of the optical resolution of the spectrometer. Figure 6.21 shows the crosstalk measured in Hamamatsu G1l135 detector. According to the image, crosstalk sensitivity is around 10%, which means that the displayed value has 10% from the left and 10% from the right neighboring pixels.

The LabView software used in the previous section has been upgraded in order to simulate the crosstalk. The same data was used as in the previous section. The FWHM was measured by applying the Gaussian fitting to the sampled data. The pixel pitch was select to be: 12.5 um (high sampling, FWHM=3.6 pix); 25 um (standard detector pitch, FWHM=1.8 pix) and 35 um (low sampling, FWHM=1.3 pix). The crosstalk sensitivity was set to 10%, which corresponds to the real one in used detectors.

Table 6.1 reports the average measured FWHM with and without pixel cross-talk. As can be seen, the influence of the cross-talk depends on the sampling. When the sampling is high or, in other words, when the optical FWHM is 3.5-4 pixels, the increase of the measured FWHM ("cross-talk effect") is only 4%. However, the situation changes when the sampling is low - the measured optical resolution (FWHM) decreases on 20%! For standard sampling, which is used on the current interrogator, degradation of the measured optical resolution is around 12%.

Table 6.1. Pixel cross-talk influence.

Pixel size, um	FWHM, pix	FWHM, no crosstalk, um	FWHM, with crosstalk, um	Increase, %
12.5	3.6	45.1	46.9	4.0
25	1.8	46.3	52.0	12.3
35	1.3	48.7	58.6	20.3

Simulations above show again how important is high sampling and what potential problems low sampling may cause – errors in the wavelength determination (undersampling noise) and degradation in the optical resolution.

6.4 Thermal and long-term drift

The main principle of spectrometer-based interrogators is that a dispersive element (usually grating) spreads different wavelength at different positions along a ccd/array detector. A pixel position on the CCD/image needs to be linked to the wavelength that ends up at that position. For this a light source with narrow peaks at known positions is used. In the end of the calibration procedure the calibration polynomial is obtained. The main goal of the calibration polynomial $\boldsymbol{C(p)}$ is to convert pixel position to wavelength, thereby if $\boldsymbol{p_1}$ is the fitted peak position in pixel units, then $\boldsymbol{\lambda_1=C(p_1)}$ is the peak position in nanometer units. Each spectrometer should pass the calibration procedure during assembling and manufacturing. However, long term drift and temperature change may lead to small shifts of components

inside the spectrometer, which cause a relative shift of the measured spectrum on the detector plane.

In order to correct calibration polynomial coefficients, I made in LabView an absolute calibration tool. The utility uses Argon, Neon or Xenon spectra as a reference. The idea was to use this software in combination with an in-built source with known wavelengths to always have correct calibrations. Unfortunately, hardware development required too much time and effort so I have made only a software part.

Let assume that $C(p)$ is the original polynomial made during spectrometer assembling and calibration procedure. Let $\alpha_1, \alpha_2 \ldots \alpha_n$ be the reference wavelengths of a known spectrum (f. ex. Argon, Neon, etc) and $\lambda_1, \lambda_2 \ldots \lambda_n$ are measured wavelengths, using the original calibration polynomial, in other words, $\lambda_1=C(p_1)$, $\lambda_2=C(p_2)$, etc. The deviation between the reference and measured wavelength is $\Delta_j=\alpha_j-\lambda_j$ and $D(p)$ is a polynomial which fits a set of deviations Δj, in other words, $\Delta_j=D(p_j)=\alpha_j-\lambda_j \Rightarrow \alpha_j=D(p_j)+\lambda_j=D(p_j)+C(p_j)$. The new calibration polynomial is sum of the original polynomial $C(p)$ and polynomial $D(p)$, which fits the deviations between the reference and measured wavelength.

The algorithm works as follows:

- Measure the reference spectrum
- Find the set of deviations **Δj** between the measured and known wavelengths
- Fit the deviations and find the coefficients of the new polynomial (order can be selected)
- Change the coefficients and save it to a file (if needs)

Figure 6.22 shows a screenshot of the main window. The top graph shows the measured reference spectrum, and the bottom one shows the calculated deviations and the correcting polynomial $D(p)$ (red line). The order of polynomial can be selected, but the maximum order is n-1, where n is the number of peaks. After the calibration the software asks to create a new file with the new corrected coefficients, the previous coefficients will be saved in a separate file with indicator old in the file name.

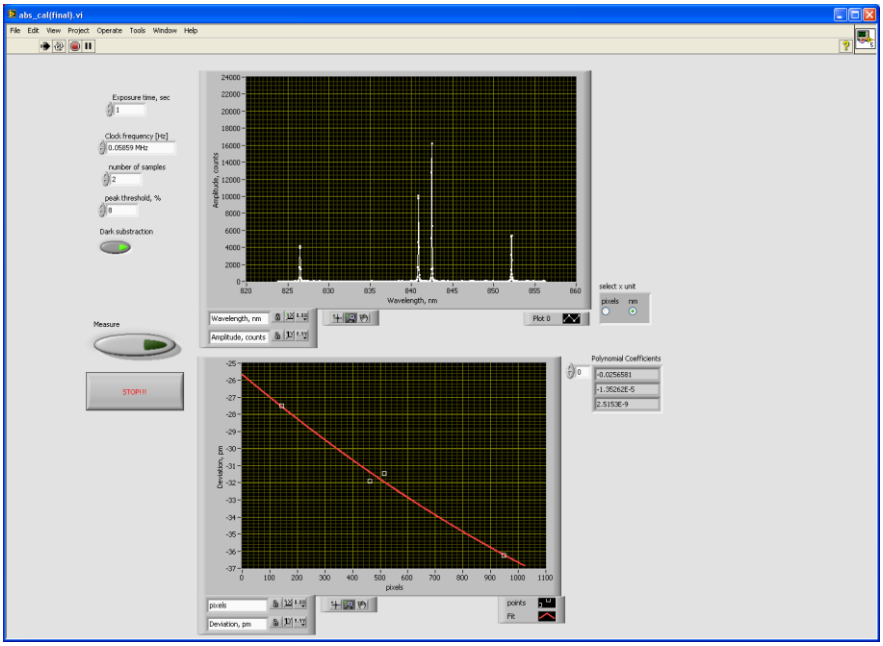

Figure 6.22. Calibration software main window.

The proposed method can easily correct the calibration polynomial and the order of correction depends only on the number of spectrum lines (peaks) used during the procedure. The proposed algorithm of calibration polynomial change will be used in the next chapter for a new method of temperature compensation.

6.5 Conclusions

In this chapter I analyzed and investigated errors, which are typical for spectrometer-based interrogators: undersampling, grating internal reflection, photo response non-uniformity, pixel crosstalk and temperature and long term drift. I showed how each of these problems affects the interrogator performance and how to eliminate and improve them. Some of the issues, like PRNU and pixel crosstalk, are intrinsic for CCD array detectors and therefore cannot be completely eliminated. However, by changing the detector to something, which doesn't have these problems, may improve interrogators precision and performance.

Chapter 7

New DMD-based interrogator: system architecture

The basic principle of FBG sensing is to measure the reflected spectrum and to track the FBG peak position. One of the most common and commercially available interrogation techniques is a spectrometer based technique. The principle of this approach was described in Chapter 2 and is the same as that used in the spectrometry. In such a system wavelength interrogation is achieved with a fixed dispersive element (e.g., prism or grating) that distributes different wavelength components at different positions along a line imaged onto an array of detector elements. Spectrometers have been continuously developed during last decades. A big effort has been directed to improve such spectrometer parameters as resolution, size, cost, speed, robustness etc [75,76,77]. One of the most important optical components of each spectrometer is a detection unit, which is typically a linear CCD array detector. It has been demonstrated that using a Digital Micromirror Device (DMD) instead of a standard array detector improves performance, programmability and signal-to-noise ratio of a spectrometer [78,79]. Moreover, due to the availability of low-cost telecommunications equipment, the most common and commercially

available FBGs work in the 1550 nm range. However, this requires use of expensive 1550 nm InGaAs array detectors to interrogate the sensors. The DMD is typically cheaper and has better pixel sampling than an InGaAs detector used in the 1550 nm range, which may lead to cost reduction and better performance. DMDs have not been used in interrogators for sensing systems and here we do it for the first time.

In this chapter we describe the architecture of a novel type of multichannel DMD based interrogator, where the linear detector is replaced with a commercially available Digital Micromirror Device (DMD) [80]. Because the DMD is a 2D array, multichannel systems can be implemented without any additional optical components, it makes the proposed interrogator highly cost-effective, in particular when used in multi-channel systems.

The presence of multiple channels also allows to measure simultaneously several parameters, like temperature, strain, humidity, etc. In addition, the digital nature of the DMD makes it very flexible and provides opportunities for Hadamard spectroscopy, which greatly improves the performance [81].

7.1 Digital Micromirror Device

7.1.1 Principle of operation

DMD is a micro-opto-electromechanical system (MOEMS) that is the core of the trademarked DLP projection technology from Texas Instruments (TI). The DMD was invented by Dr. Larry Hornbeck in 1987 and since that time has been used in many different applications: televisions and HDTVs, Head-mounted displays, digital cinema, metrology, laser beam machining and spectroscopy [78, 82]. However, the biggest application is Digital Light Processing (DLP) projectors.

The DMD is a 2D mirror array with several hundred thousand microscopic mirrors that can be set individually in either on or off state. Each micromirror is attached to a hidden torsional hinge. The underside of the micromirrors makes contact with the spring tips shown in Figure 7.1. By activating an electrode (red in Fig. 7.1) on the opposite side the mirrors turns to that side. Each mirror can be in three states: an ON state, where the mirror is tilted on +17° (or +12°, it depends on the model of the DMD chip), an OFF state, where the mirror is tilted on -17° (or -12°) and a zero (resting) state where the mirror

is parallel to the DMD chip surface. When the DMD is used all mirrors can be in either ON or OFF state, in zero state mirror can be when no signal is sent to the DMD chip.

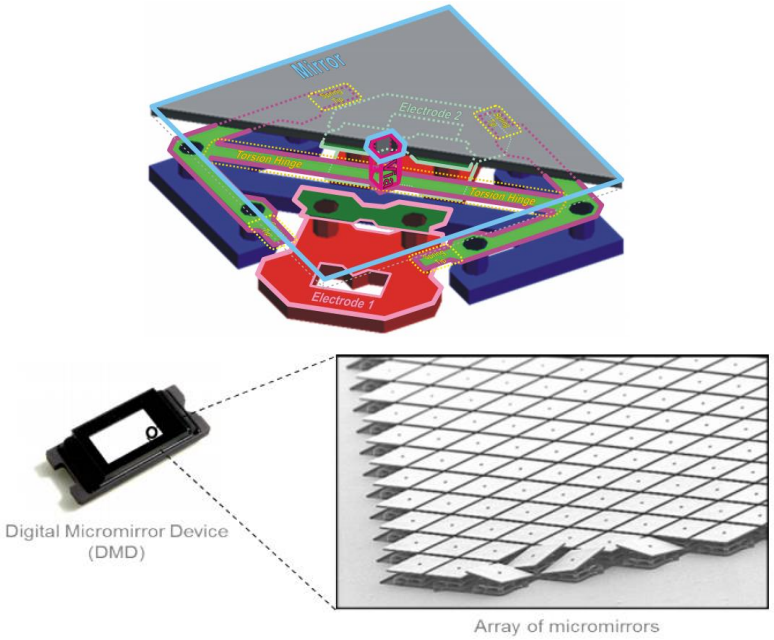

Figure 7.1. (a) top - single mirror scheme, (b) bottom – close-up of a Mirror Array (image from [83]).

7.1.2 DMD in spectroscopy

In a standard spectrometer different colors are dispersed by the diffraction gratings across the linear detector (Figure 7.2(a)). In the DMD the mirrors can be controlled individually, thus the replacement of the detector by the DMD makes it possible to switch out exactly the color required, whereas all other colors are sent to a wavelength dump (Figure 7.2(b)). In other words, when the mirror is in the ON state the wavelength, which is focused on that mirror by the lens, is sent by the mirror to a single point detector (green color on Figure 7.2 (b)). By sequentially scanning through the columns (turning on specific columns of pixels) of the DMD, a spectrum of the input light is measured by the detector as a function of time.

The DMD-based schemes for spectroscopy offer many advantages over existing solutions:

1. DMDs have more pixels and better sampling that are available in CCD arrays (especially for InGaAs detectors)
2. DMDs are cheaper then InGaAs detectors
3. DMD eliminates errors due to pixel defects and non-uniformities, which was discussed in the previous chapter
4. DMD can be very compact making the whole spectrometer also very compact
5. DMD is a 2D array and each mirror can be controlled individually:
    - Multichannel systems can be implemented without additional optical components, dropping price per channel significantly down
    - Hadamard scan method can be implemented, greatly increasing signal-to-noise ratio (SNR)

For this project I selected a new commercially available DLP2010NIR produced by Texas Instrument.

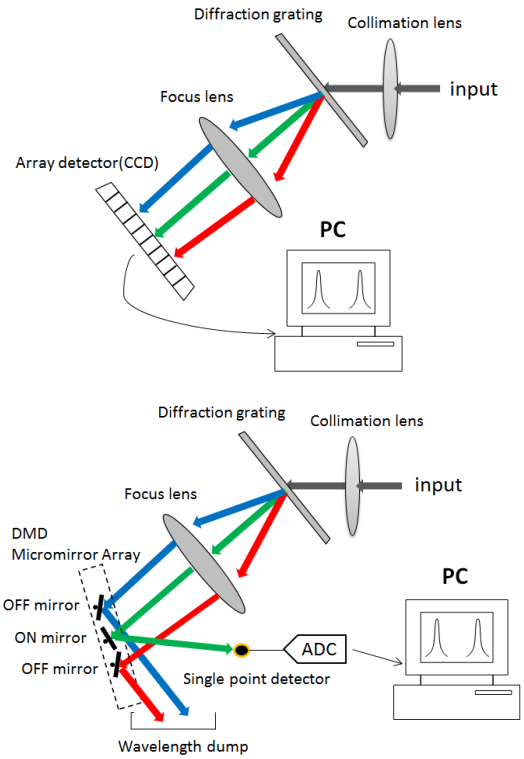

Figure 7.2. (a) top – standard spectrometer scheme, (b) bottom - DMD-based spectrometer scheme.

7.1.3 DLP2010NIR and control electronics

The new DLP2010NIR DMD is optimized for operation at wavelengths between 700 and 2500 nm and has an 854x480 array of polarization independent aluminum micrometer-sized mirrors in an orthogonal layout with 5.4 um mirror pitch. The micromirror active array size is 4.61 by 2.59 mm, which makes a potential interrogator very compact. One of the most important parameters, which defines the geometry, is how the mirrors tilt and switch from the ON to the OFF state. The landed pixel orientation and tilt are shown in Figure 7.3, the micromirror tilt angle is 17° relative to the plane formed by the overall micromirror array.

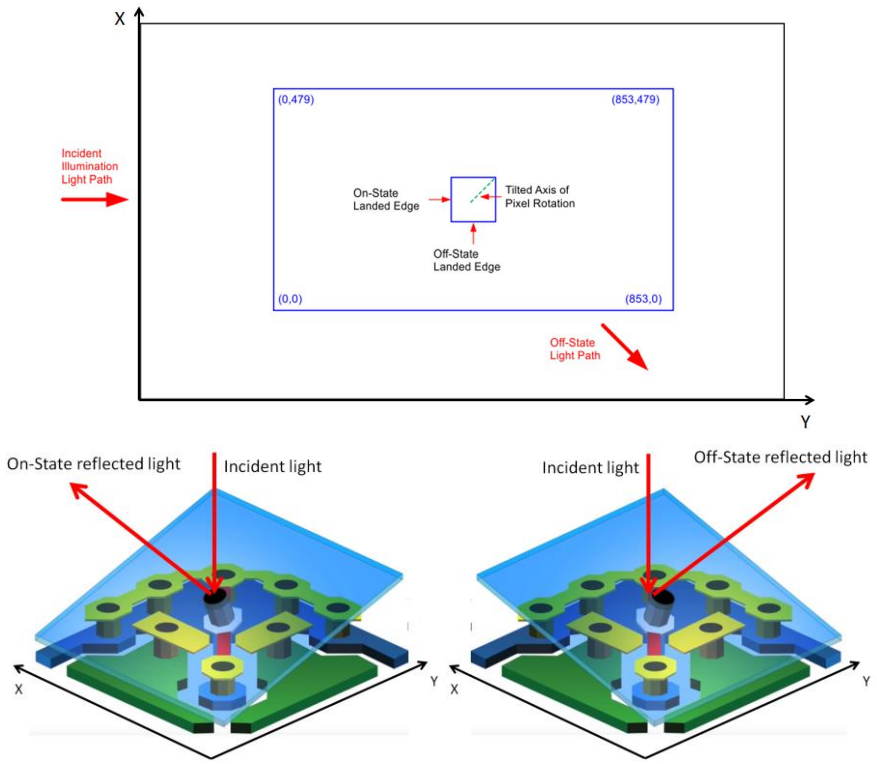

Figure 7.3. (a) top – landed mirror orientation and tilt of the DLP2010NIR, (b) bottom left – ON state micromirror position, (c) bottom right – OFF state micromirror position (image from [80]).

The DLP2010NIR DMD is always controlled by the DLPC150 controller, which provides a convenient, reliable, and multi-functional interface between user electronics and the DLP2010NIR with high-speed, precision, and

efficiency. Since the development of own electronics is a quite difficult task, which requires special skills and experience, it has been decided to use an existing solution, which could greatly simplify the whole product development and allowed us to focus on optical performance, software development and improvements. As an existing solution, it was decided to use electronics from DLP NIRscan Nano EVM – an evaluation spectrometer module made by Texas Instruments. The EVM contains the DLP2010NIR digital micromirror device, DLPC150 digital controller, DLPA2005 integrated power management components and also optomechanical components, such as lenses, grating, slits, housing, which were not used in this work. It is important to note that only electronics from the EVM module was used, which includes:

- **Microcontroller board**
  1. Tiva TM4C1297 microprocessor for system control operating at 120 MHz
  2. 32MB SDRAM for pattern storage
  3. CC2564MODN Bluetooth Low Energy module for Bluetooth 4.0 connectivity
  4. USB micro connector for USB connectivity
  5. microSD card slot for external data storage
  6. HDC1000 humidity and temperature sensor
- **DLP controller board**
  1. DLPC150 DLP controller
  2. DLPA2005 integrated power management circuit for DMD and DLP controller supplies
- **Detector board**
  1. Low-noise differential amplifier circuit
  2. ADS1255 30 kSPS analog-to-digital converter (ADC) with SPI
  3. TMP006 thermopile sensor for detector and ambient temperature measurement
  4. 1-mm non-cooled Hamamatsu G12180-010A InGaAs photodiode
- **DMD board**
  1. DLP2010NIR near-infrared digital micromirror device

The full description of the components can be found in [84]. Figure 7.4 shows all electronic components listed above, which were decided to be used.

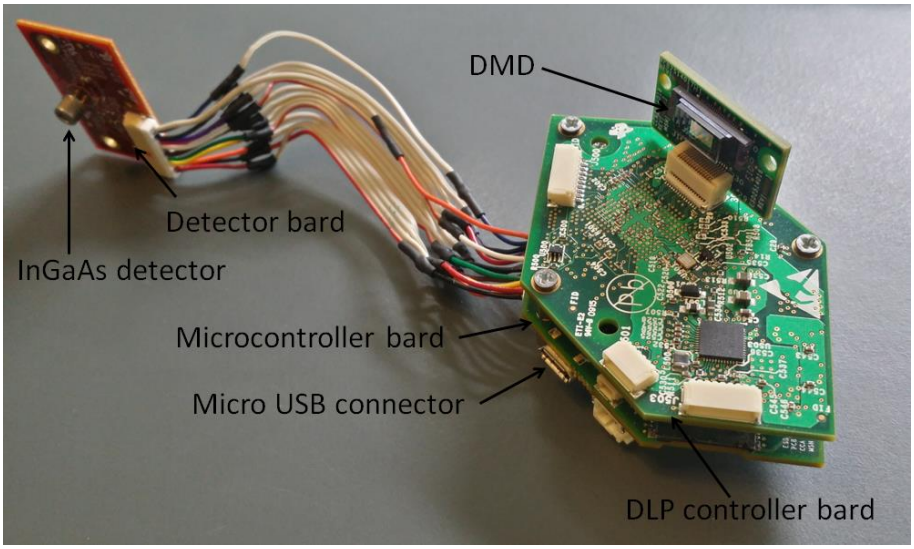

Figure 7.4. Electronics and DMD from EVM module used in the project.

As was listed above, the electronics contains Tiva TM4C1297 microprocessor, which is the system's main control processor. The Tiva handles button presses, commands and data transfers over USB or Bluetooth, controls the DLP subsystem, streams the patterns to select specific wavelengths, captures data from InGaAs detector, activates lamps, and stores data in the microSD card. The Tiva microprocessor, in turn, can be controlled by the main application installed on the PC. The main application initializes the system and sends commands and receives data via USB. The whole list of commands with detailed description can also be found in [84] and not included here due to its big size. As the main software Texas Instruments provides also Windows software called NIRscan Nano GUI, which can run a scan and interpret measured data, so, in other words, show the measured spectrum. But due to the limited functionality of the NIRscan Nano GUI, it has been decided to build own software, which should be more suitable for interrogation process and include extra features, such as spectrum processing, temperature compensation etc. The new software will be described later in this chapter.

7.2 Optical design

In this section an optical design of the new DMD based interrogator is discussed. The optical design has been made using Zemax. All optical analysis in this and next chapters have also been done in Zemax.

Zemax is an optical design program that is used to design and analyze imaging systems such as camera lenses, as well as illumination systems. It works by ray tracing—modeling the propagation of rays through an optical system. It can model the effect of optical elements such as simple lenses, aspheric lenses, gradient-index lenses, mirrors, and diffractive optical elements, and can produce standard analysis diagrams such as spot diagrams and ray-fan plots

7.2.1 Choice of geometry

In a standard spectrometer different wavelengths are dispersed by the diffraction gratings across the linear detector. In the DMD the mirrors can be controlled individually, thus the replacement of the detector by the DMD makes it possible to switch out exactly the wavelength required, whereas all other colors are sent to a wavelength dump. There are two different ways of sending light back to the detector: 1) retro-reflect and 2) transmission scheme [86].

In the retro-reflect scheme the on-state light is captured by the focus lens and the colors are gathered by the diffraction grating(s) and focused to a single element detector or a fiber via an output lens. Since the light is sent back through the same diffraction grating(s) and the light dispersion in the forward path is totally compensated in the reflected optical path it is possible to achieve a wavelength homogeneous small output image. It means that as an output one can use small single element detectors or even fiber(s), also due to the small image size the light density is relatively high, this fact means potentially higher signal-to-noise ration.

In the transmission geometry, the DMD is side illuminated and the input and output path are separated completely. Use of the diffraction grating(s) only in the forward path gives a benefit in power, as there is no diffraction efficiency loss in the output. However, lack of gratings in the output makes is

difficult to have all wavelengths focused in the same spot on the detector, which obviously requires a larger detector.

Since the DMD is a 2-dimensional array of mirrors it makes it possible to build multichannel system, where several channels can be monitored simultaneously. There are 2 ways to implement the channel separation and simultaneously interrogation: 1) using a single-element detector and scan each channel one by one (signal from different channels is separated in the DMD plane); 2) scan the whole DMD by column and simultaneously measure signals from several detectors (pixels). The second approach gives x times higher interrogation speed, where x – is the number of channels, however, it requires smaller spot size and low cross-talk on the detector plane.

In order to investigate and select the best configuration, 3 different optical concepts have been developed and presented below.

7.2.1.1 Retro-reflect scheme with mirror

The first trial was to take the standard commercial available interrogators (I-MON) optical scheme and slightly modify it – change the detector array to the DMD, add one more lens to focus the light to the detector. One can add that the DMD size is almost 3 times smaller than the standard detector size: 4.5 mm vs 12.8 mm.

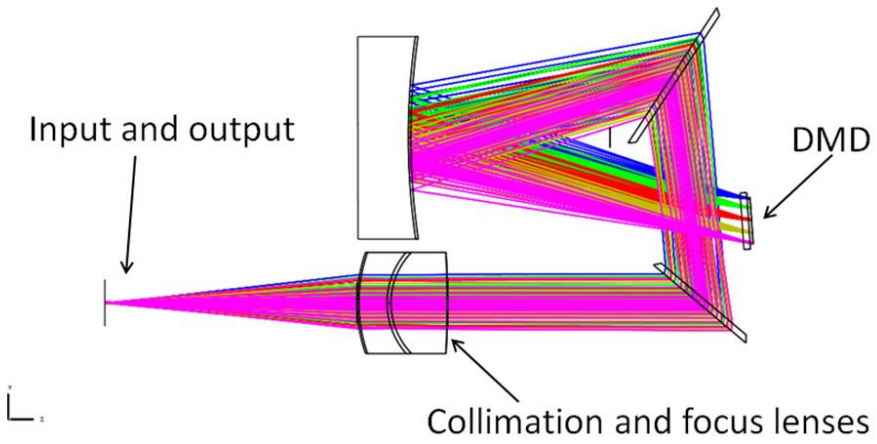

Figure 7.5. Schematic for the mirror retro-reflection concept.

A schematic of the optical layout for the mirror retro-reflection concept is shown in Fig. 7.5. The main advantages of this concept are: a) it uses the

standard I-MON optical scheme (compact size); b) the output is a wavelength homogenous small output image (Fig. 7.6 right).

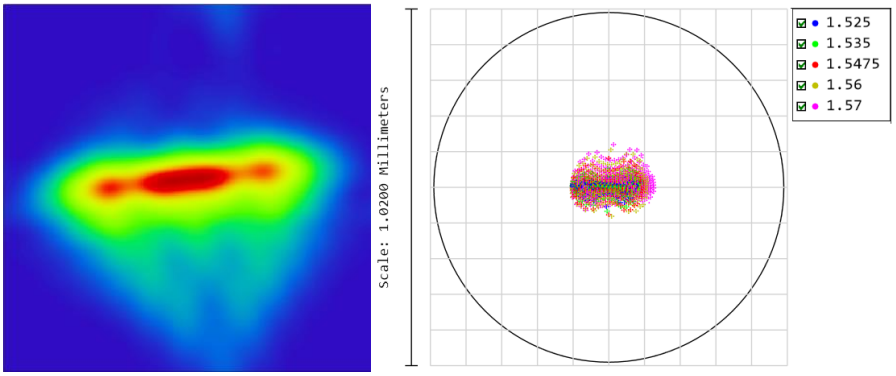

Figure 7.6. (a) left - spot shape on the DMD plane (different color indicates different intensity); (b) right - on the detector plane.

Despite the use of the retro-reflect scheme advantages, this concept shows poor performance in terms of the resolution and spot shape on the DMD plane (see Fig. 7.6(a)). It seems that one surface of the mirror is not enough to focus the light on 3 times smaller surface (it leads to higher magnification) and at the same time keeping a good resolution. The other problem is that the DMD main surface has to be tilted at 17 degrees to the chief ray. The FWHM on the DMD plane was shown to be ~40 um, which gives approximately 400 pm optical resolution.

7.2.1.2 Retro-reflect scheme with lens

The next concept is also based on the retro-reflect scheme, however, the focusing mirror has been exchanged with a focus lens. Since even a simple (singlet) lens has 4 variables (two surface curvatures, the lens thickness and the glass material) compared to the mirror (only one – the radius of curvature) this fact may introduce some improvements in the performance.

A schematic of the optical layout for the lens retro-reflection concept is shown in Fig. 7.7. As the previous one, this concept uses the main advantage of the retro-reflection scheme – the output is the image of the input, it means that the light is focused into a very small spot in the detector plane, and the colors are gathered by the gratings and focused into the same spot (Fig. 7.8(b)). However, compared to the previous scheme, the FWHM on the DMD plane is much better – around 16 um for the central wavelength and

the spot shape on the DMD plane is close to the ring (see Figure 7.8 (a)). I.e., it is easier to separate multiple channels in the output plane with room for more channels in the same optical design. The optical resolution is around 160 pm.

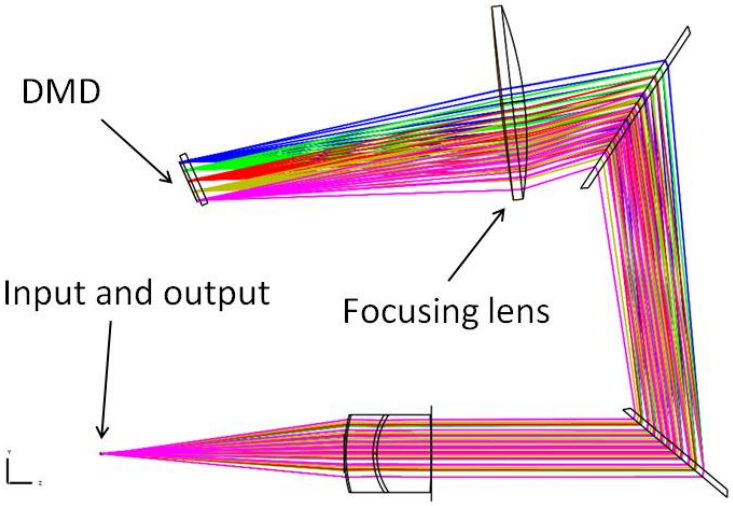

Figure 7.7. Schematic for the lens retro-reflect concept.

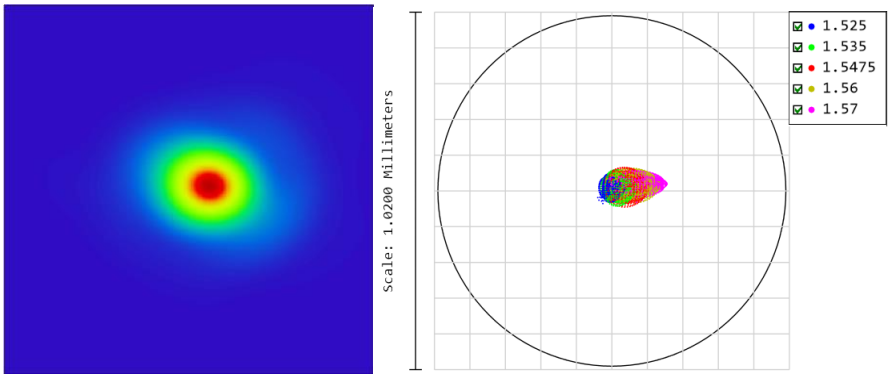

Figure 7.8. (a) left - spot shape on the DMD plane (different color indicates different intensity); (b) right - on the detector plane.

7.2.1.3 Transmission scheme with lens

Despite the fact, that the retro-reflect scheme has a big advantage, it is also worth to mention that it requires using big diffraction gratings and one additional lens. And this may potentially increase the price (and size) of the system.

A schematic of the optical layout for the transmission concept is shown in Fig. 7.9.

The main advantage is that the DMD plane is now perpendicular to the chief rays. It makes easier to focus light on the DMD; the focusing lens is not off-axis. However, the detector focusing lens cannot focus different colors into the same spot in the detector plane and the output image is bigger and significantly in-homogenous (Fig. 7.10(b)), which potentially gives smaller SNR and requires much bigger detector, which may effect on the price, especially for InGaAs detectors. The optical performance on the DMD plane is as good as in the previous concept with FWHM around ~16 um for the central wavelength and the circular spot shape (Fig. 7.10(a)).

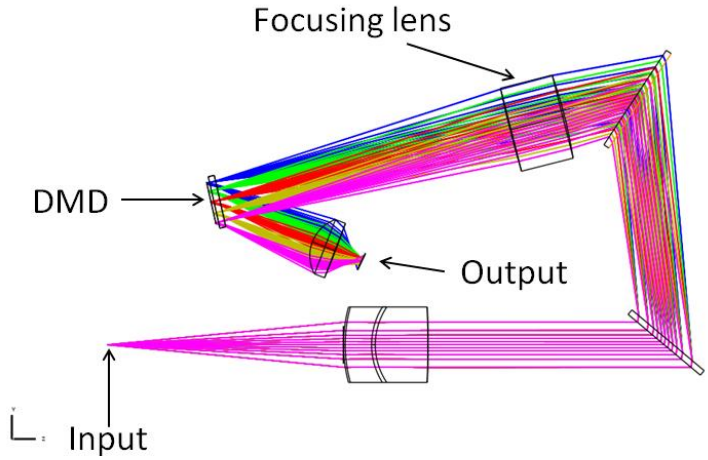

Figure 7.9. Schematic for the straight-forward scheme.

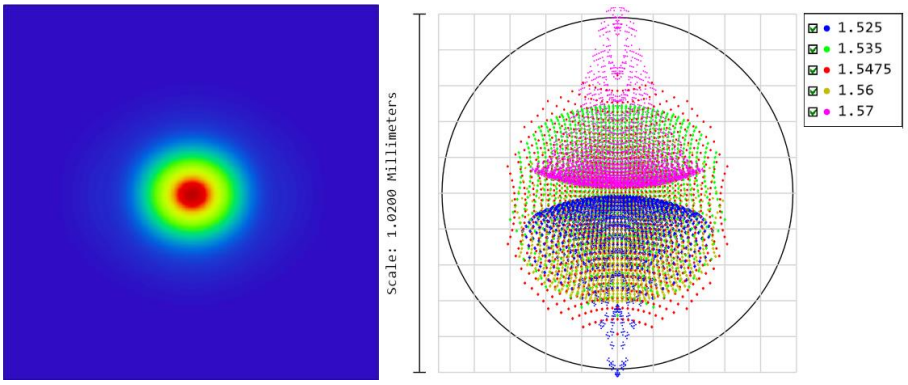

Figure 7.10. (a) left - spot shape on the DMD plane (different color indicates different intensity); (b) right - on the detector plane.

The other advantage of this concept is that it needs a smaller grating area, which potentially may decrease the price. However, due to the relatively high detector spot area (Fig. 7.10(b)), this scheme makes impossible to separate multiple channels at the detector, i.e. simultaneously readout of data from all channels is not possible; channels can be separated only by the DMD, which significantly decreases the speed. The previous retro-reflection concept has both options in terms of the channel separation, and despite potentially higher grating cost was selected for further development.

7.2.2 Design description

As follows from the previous section the retro-reflect scheme with a lens has been selected for further development. In the layout presented in section 7.2.1.2 one singlet lens is used to focus the light on the DMD plane. It allows to achieve 160 pm of optical resolution (in theory). Unfortunately, this was only for the central wavelength of 1547 nm, for other wavelengths (1525 nm, 1535nm, 1560nm and 1570 nm) the resolution was much worse. The reason is that the DMD plane has an angle of 17 degrees to the chief ray. That is needed to reflect the light back by the same optical path, when the mirror is in the ON state. The angle between the ON state mirror and the DMD chip surface is 17 degrees. So by using one singlet lens, it was not possible to have the optical resolution of less than 200 pm for all wavelengths. It has been decided to change the focus lens to an achromatic lens, which is made of two different glasses. This will add 3 extra variables – one surface curvature, extra thickness and a second glass. Zemax can also vary glass material to decrease the lens aberrations and reach the best performance.

On the one hand, the decision to use the electronics from the NIRscan Nano EVM simplified the product development, since one can use ready-made solution, but from the other hand, it makes optical design development more complex since it introduces extra constraints. One must take into account the size and geometry of the boards to avoid potential collisions between lenses and boards. This has been done by upgrading the Merit Function Editor in Zemax, which is used to define, modify, and review the system merit function. The system merit function is used for optimization.

2D layout and overall 3D scheme of the new interrogator (codename I-MON DMD) is shown in Figure 7.11 (a) and 7.11 (b), respectively. The

presented optical scheme is further development of the lens retro-reflect concept with custom designed achromatic lens and improved merit function, as was described above.

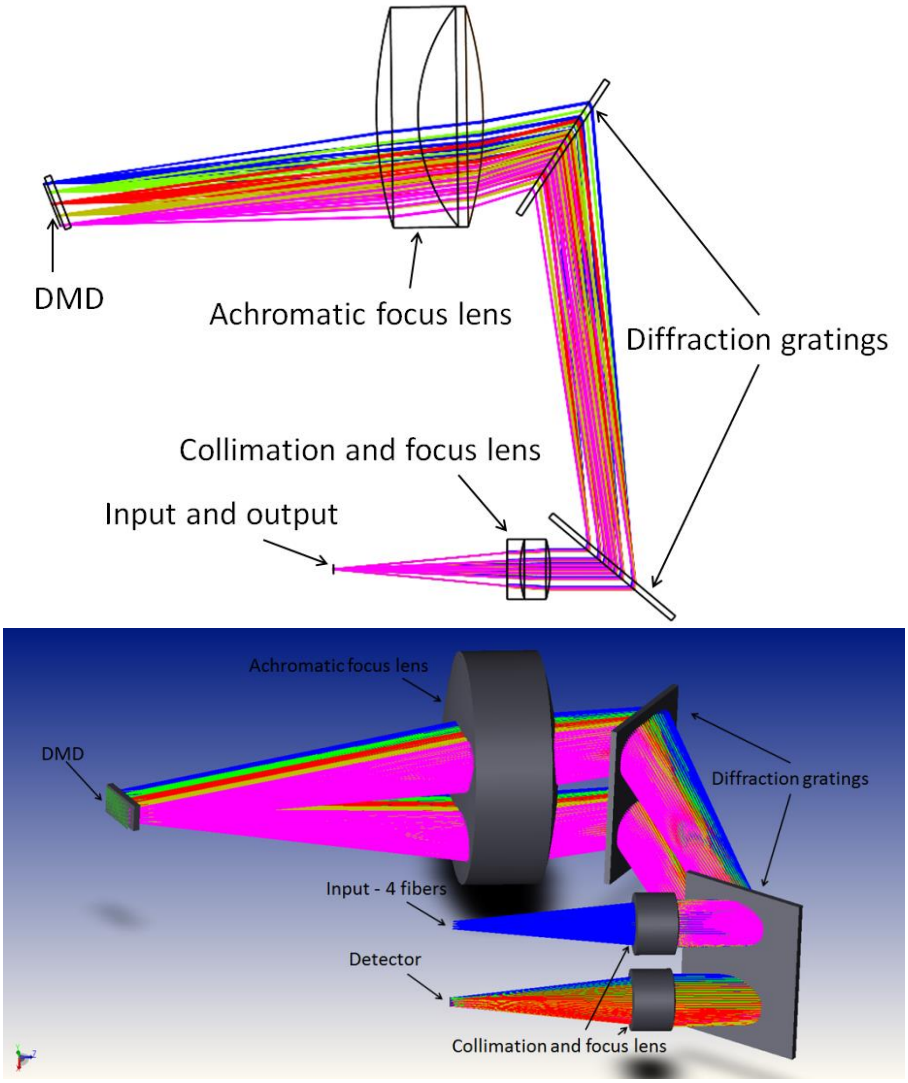

Figure 7.11. (a) top – I-MON DMD 2D layout, (b) bottom – 3D image of the new interrogator.

The presented spectrometer based interrogator has 4 optical fibers as input, where each fiber is a standard telecom single mode SMF-28 fiber. The input wavelength range is from 1525 to 1570 nm. The selected DMD is the DLP2010NIR produced by Texas Instruments [80] with an 854x480 array of

polarization independent aluminum coated micrometer-sized mirrors, in an orthogonal layout with 5.4 um mirror pitch. The chip active array size is 4.61 by 2.59 mm. The optical signal enters the device through one of 4 optical fibers with NA=0.14 and a mode-field diameter=10.4. Fibers are mounted in a commercial available V-groove assembly from Oz Optics, and the distance between the cores is 250 um. The divergent light from the fibers is collimated by an achromatic lens made by Edmund optics (Stock No. #45-786). Two identical highly efficient diffraction gratings are used to disperse the light. For the first grating, all wavelengths have the same angle of incidence (AOI) of 49.9°, for the second the AOI depends on the wavelength, as the long wavelengths are dispersed more than the short in the first grating (1525nm: 51.8°, 1545nm: 50.2°, 1570nm: 48.2°). The gratings period is 1035 nm, which corresponds to 966 lines per mm. The gratings are optimized to work for both the TE and TM polarization mode, i.e. they are polarization independent gratings. After the gratings the various wavelengths are focused onto the DMD surface by a custom designed achromatic lens with a back focal length of 34.66 mm.

When the DMD mirror is in the ON state the light is reflected and sent through the same components back, where it is focused onto a single-element detector by a focusing lens. The output focusing lens is the same as the collimation lens. In this scheme, the output is an image of the input without using complicated and expensive optics. The detector is 1-mm non-cooled Hamamatsu G12180-010A InGaAs photodiode.

The optical resolution is defined as the spectral width measured by the instrument of a spectrum with zero width. It is typically specified in full-width half-max (FWHM), defined as the width of the spectral peak when its height is 50% of the peak value. It is commonly quoted in units of nanometers or wave numbers. This definition is convenient, as it also describes the minimum distance required between two zero width input wavelengths of the same amplitude before an instrument can detect two distinct peaks instead of one broad peak To calculate the optical resolution in the DMD plane Extended Diffraction Image Analysis (EDIA) in Zemax has been made for 5 wavelengths uniformly spread across the 1525-1570 nm spectrum and including the outer wavelengths. It is necessary to use the EDIA here since the system is diffraction limited, therefore it is the only

solution for showing combined aberrations and diffraction limit. The analysis has also been made for all 4 channels. An input fiber with mode field diameter of 10.4um and NA (1%) = 0.14 is used (see SM-28 optical specifications). The y-direction is along the length of the DMD, i.e. in the wavelength dispersion direction. The x-direction is perpendicular to y in the DMD plane.

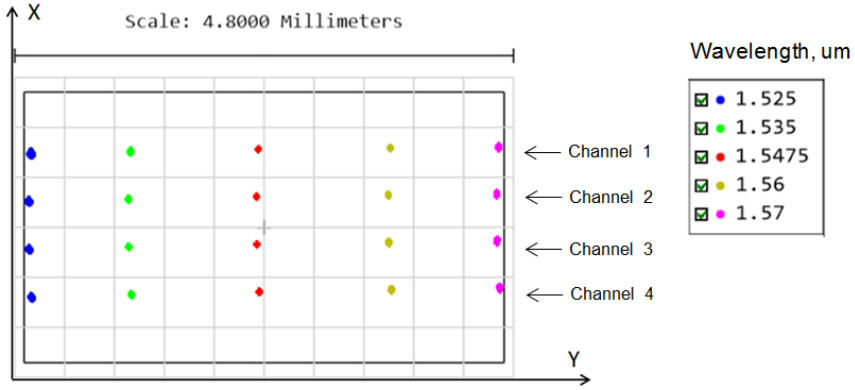

Figure 7.12. Footprint of 5 wavelengths and 4 channels in the DMD plane (image from Zemax).

As can be seen from figure 7.12, different wavelengths are dispersed on the DMD chip along the horizontal axis and the different channels are separated along the vertical axis. The optical resolution (FWHM) on the DMD plane is shown in Fig. 7.13.

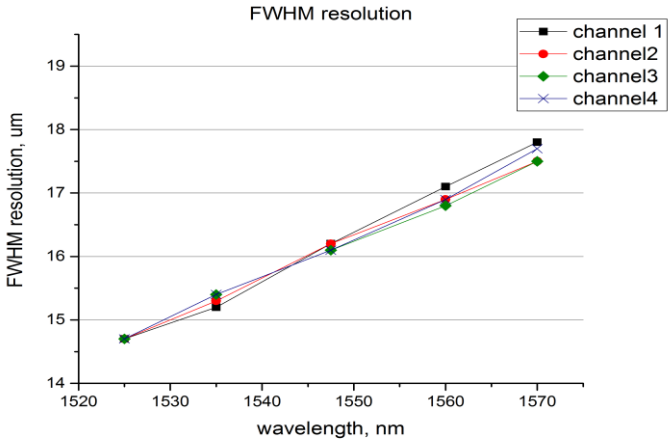

Figure 7.13. FWHM resolution for all 4 channels.

The average channel resolution in um and in nm is also shown in Table 7.1:

Wavelength, nm	Avg. channel spot FWHM, um	Avg. channel spot FWHM, pix	Avg. channel spot FWHM, pm
1525	14.7	2.7	155
1535	15.3	2.8	157
1547.5	16.2	3	164
1560	16.9	3.1	165
1570	17.6	3.3	172

As can be seen from Table 7.1 the theoretical optical resolution varies from 156 to 172 pm, which corresponds to ~15-17.6 um spot size. The DMD mirror pitch is 5.4 um, thus it gives from 2.7 to 3.3 pixels per spot. These numbers are higher than 2.8 pixels/spot almost for all wavelengths and it means potentially low undersampling noise (see discussion in Chapter 6.1.2).

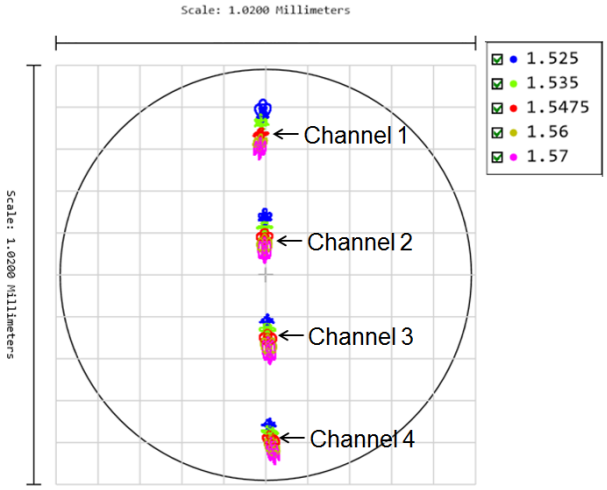

Figure 7.14. Footprint diagram on the detector, when all mirrors are in the ON state (image from Zemax).

The image on the detector is shown in Figure 7.14. Despite the fact that light passes through the diffraction gratings in the output pass, the image still has some wavelength in-homogeneity. On Figure 7.14 it can be seen that for each channel different colors are focused on slightly different places,

however, the deviation is not so big. For a 4 channel system, it is not so important, the outputs can be separated if it needs. The reason of this phenomena is that distortion and aberrations occur in the DMD focus lens and also that the focus achromatic lens is off-axis. This effect can be significantly decreased by changing one focus lens to two separate lenses, however, this may lead to a more complicated and expensive construction.

The design has been made in such a way to avoid channel cross talk caused due to a spatial overlap (Figure 7.12). Here we use the 2D digital nature of the DMD chip and scan each channel one by one. Figure 7.14 shows that all 4 channels are also clearly separated in the detector plane. In the current design this feature is not used, the most important that there is no signal cut-off. But it potentially allows to improve current scheme by replacing one single-chip detector by a detector per channel to perform parallel channel readout.

The presented optical design is quite flexible – it allows to add extra channels just by replacing the input fiber V-groove array. Figure 7.15 shows footprint diagrams on the DMD and detector planes for 8 channels configuration. Only input V-groove array was replaced, all other components are the same as for the 4 channel system.

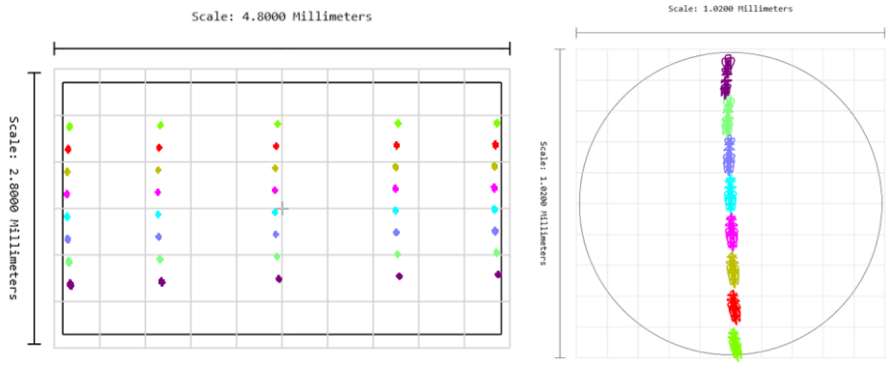

Figure 7.15. (a) left – footprint of 8 channels in the DMD plane (image from Zemax), (b) right - footprint diagram on the detector, when all mirrors are in the ON state (image from Zemax). Here different colors indicate different channels.

Even for 8 fibers configuration, all 8 channels are greatly separated on both DMD and detectors planes. It makes the proposed design extremely cost effective regarding the price per channel. My calculation shows that with the

current design the maximum number of channels, which can be separated on the DMD plane is 22, however, in this case it will require a custom made V-groove array and alignment procedure will be more complex.

7.2.3 DMD angle tolerance

Each micromirror from the DMD array can be placed in one of 3 states: ON, Off and Zero. The most important is the ON-State where the light is sent back and focused on the detector. When the mirror is in the ON-State, the angle between the mirror and the plane formed by the overall micromirror array is 17 degrees (see Fig. 7.3(a)). Despite the fact that the deflection angle is very repeatable, some uncertainty may also occur. When the micromirror in the ON-State has angle variation relative to the nominal landed position, the reflected light optical path is also tilted relative to the nominal one and some part of the light may not hit the detector. The intensity of the measured signal reflected from the given mirror is lower than it should be. Since this uncertainty in the tilt angle is unpredictable and different for different mirrors, it may lead to significant distortion in the measured spectrum, which leads to errors in the fitted wavelength.

Figure 7.16 shows how the efficiency of each channel depends on the deviation from the nominal On-State position. The efficiency is the ratio of the measured power on the detector to the total power launched into the system. The detector is a circle with 1 mm in diameter (Fig. 7.14). The top image shows the case when additional angle about X axis is introduced. The nominal rotation angle about X axis is 17 degrees in the On-State (Fig. 7.3(a)). As can be seen from Figure 7.14(a) when the angle deviation is less than 1 degree (-1<deviation<1), the efficiency is higher than 99%, thus losses are less than 1%. The bottom image shows the case when additional angle about Y-axis is introduced. The nominal rotation angle about Y-axis is 0 degree in the On-State. As can be seen, the efficiency is channel-dependable and the top flat area, when there is no influence from the angle tilt is shifted for different channels. Only when the tilt angle variation is from -0.6 to 0.6 the efficiency for all channels is more than 99%. In the DMD specifications [81] micromirror tilt angle tolerance is specified to be from -1 to +1 degree and this value represents the landed tilt angle variation relative to the nominal landed tilt angle, which is the case shown in Fig. 7.16 top.

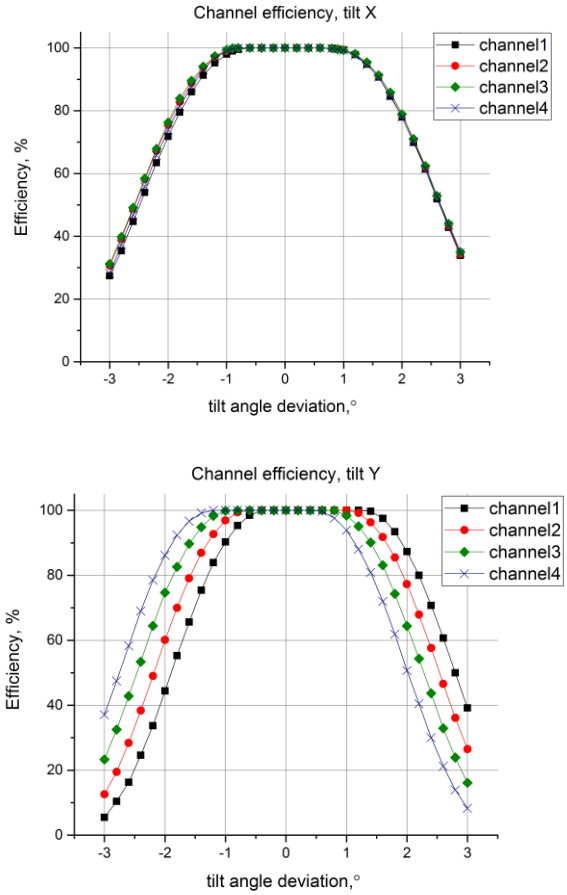

Figure 7.16. Channel efficiency vs tilt angle deviation when the mirrors are tilt about X (top) and about Y(bottom) axes.

This analysis shows that the micromirror angle deviation has no big influence on the intensity of the measured signal. Practical evaluation will be done in the next chapter.

7.2.4 Stray light consideration

There are several possible contributions to stray light, which need to be covered. The stray light ghost analysis has been done in Zemax in order to investigate and estimate multiple reflections between lenses, gratings and other surfaces. It has been found that only reflections between the DMD glass window surfaces and the DMD plane surface can be noticed.

7.2.4.1 DMD window

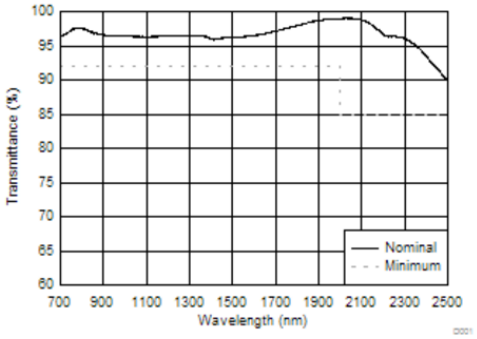

Figure 7.17. DLP2010NIR DMD Window transmittance (image from [81]).

The DMD is supplied with a thick glass window, with the AR coating shown in Fig. 7.17. There can be expected some multiple reflections (as can be seen from the stray light ghost analysis). How these behave is a very complex issue, depending and changing with DMD mirror settings, and it has not been possible to simulate this well in Zemax. Fig. 7.17 shows that transmission between 1525 and 1570 nm is around 97%, which means very low potential multiple reflections.

7.2.4.2 Unwanted orders from gratings

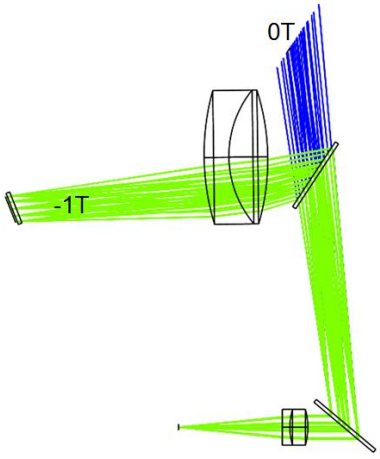

Figure 7.18. 0T (blue) and -1T(green) from the second grating, Y-Z geometry

With given angles of incidence around 49.9° for the first grating and from 48.2° to 51.8° (depends on the wavelength) for the second grating, grating

period and central wavelength according to the grating equation only two diffractive orders can exist: 0T and -1T. The distance between the gratings are around 40 mm, zero order from the first grating will not interact with the next grating and will not affect the performance. The second grating is positioned close to the focusing lens, which potentially may cause unwanted interaction between the 0T diffractive order and the lens.

Fig. 7.18 shows 0T and -1T from the second grating. It can be seen that the distance between the second grating and the lens is sufficient and 0T doesn't hit the lens aperture, which means that the 0T can be screened and trapped completely off.

7.2.4.3 Zero state reflections from the DMD

The DMD zero state has all mirrors parallel to the global plane of the DMD. The DMD only has mirrors in its zero state if it has no power, and is not very interesting. But as many of the micro-mechanical surfaces around and behind the mirrors are parallel to the global DMD plane, it is expected that even with all mirrors in on/off state, there still might be some light reflected in the zero state direction. The return beam path of the zero state is shown below (Figure 7.19), where it is also seen that it does not hit the focusing lens, and therefore cannot be focused onto the detector. However, this reflection will be partly diffused and some of it will hit the detector as a DC, but it will be subtracted, unfortunately it is not possible to simulate the diffusion on Zemax. A dump can be added to kill most of the zero state light.

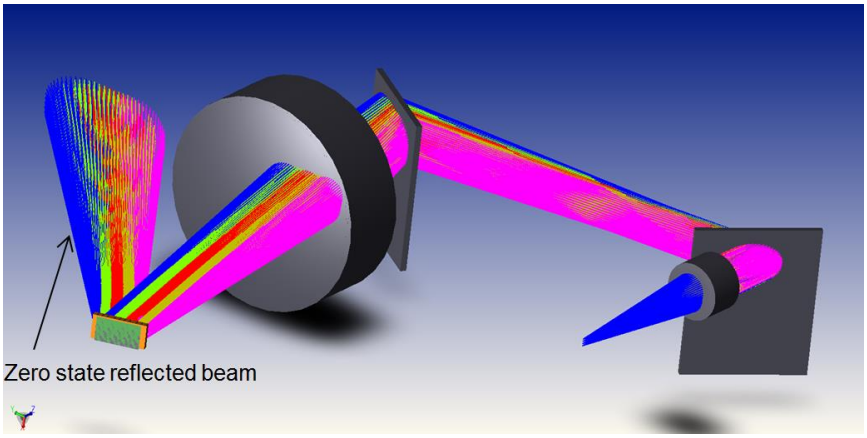

Figure 7.19. All mirrors are in zero state, 3D beam path (image from Zemax).

7.2.4.4 OFF state reflections from the DMD

Most of the time most of the mirrors will be set in the OFF state and it is, therefore, important to analyze where this light terminates. The off state ray trace is shown in Figure 7.20 below, and it is possible to mechanically screen it off with multiple black surfaces or beam dump.

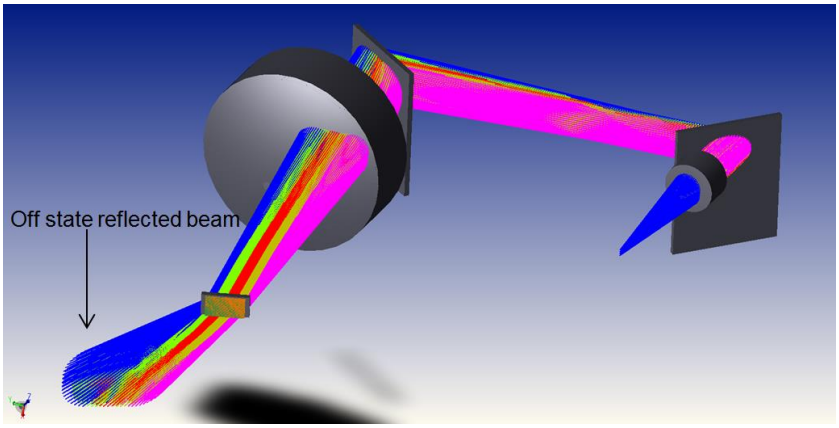

Figure 7.20. All mirrors are in OFF state, 3D beam path (image from Zemax).

7.2.5 Optical design - conclusions

In this section optical design of the new DMD based interrogator has been described in details. Three different concepts based on two different optical schemes with a DMD (retro-reflect and transmission) has been analyzed and compared. The retro-reflect scheme with a lens has been selected and developed. It has been shown an overview of the geometry, expected diffraction limited spot-sizes in the DMD plane (resolution performance), DMD tilt angle tolerance and stray light considerations.

7.3 Mechanical design

Mechanical design has been made in Autodesk Inventor by Ibsen's mechanical engineer and my colleague Poul Hansen. Figure 7.21 shows the final version of the design. The input 4 fibers in V-groove are fixed by a top screw to the input holder (white color), which can be adjusted in 2 directions for optimum position. The collimation lens can be adjusted by a tool with an eccentrically placed tap and a groove in the adapter and then fixed by a screw. Gratings are glued to the grating holders by using epoxy glue. The

DMD focus lens is fixed by a ring holder and cannot be adjusted. The DMD with the DMD board is fixed by screws to the holder and the base plate, respectively. The DMD angle can be slightly varied to find the optimum position. The detector (single chip InGaAs) and the detector board are connected to the holder (blue color), which can also be adjusted in two directions for optimum position. Figure 7.21 shows that the interrogator is compact, the size is 14.6 cm x 11.6cm x 5.5 cm.

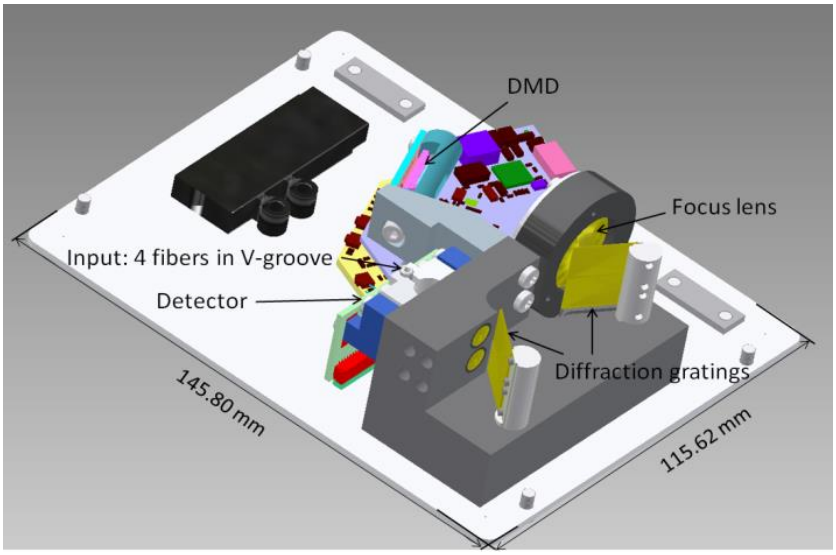

Figure 7.21. Interrogator mechanical design – 3D image from Autodesk.

When the optical and mechanical design was finished all components have been ordered and the device was assembled, aligned and tested.

7.4 Software

As was mentioned before, the Nano EVM electronics can be controlled by the main software by sending USB commands. Texas Instruments provides also Windows software called NIRscan Nano GUI, which can run a scan and interpret measured data. However, due to the limited functionality of the NIRscan Nano GUI, it has been decided to build own software.

The new software has been written using LabView 2012, Installer and application have also been created, which allows to run the software on any PC with Windows OS. The DLP NIRscan Nano electronics communicates using USB 1.1 human interface device (HID) protocol to exchange commands

and data with a host (PC). The USB commands are variable length data packets that are sent with the least significant byte first. Hidapi.dll has been used to send USB commands from LabView interface to the electronics and also to receive the raw data. All data interpretation has been made in the LabView software. The full list of supported commands can be found in [80].

7.4.1 Main screen and configuration

Figure 7.22 shows the main screen, which appears after the software start-up. There are 5 tabs – 4 tabs contain a spectrum graph and a wavelength graph per each channel (Fig. 7.22 shows graphs arrangement for Channel 1). The fifth tab contains control soft keys and displays that allow the user to setup and optimize the measurement for the user's needs.

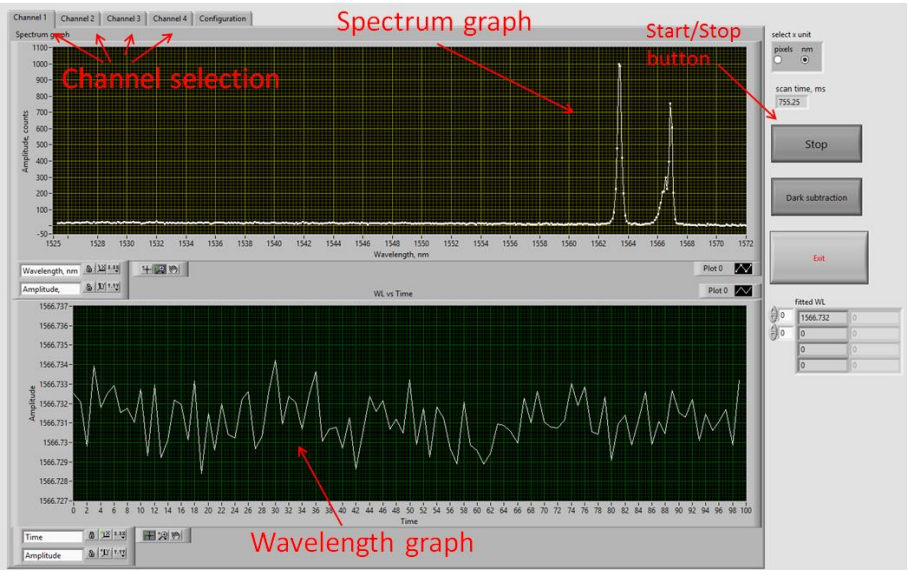

Figure 7.22. I-MON DMD software – the main screen.

To start a measurement "Start" button must be pushed. The spectrum graph shows the wavelength spectrum of the measured signal, i.e., it shows the power measured by the InGaAs detector when the certain mirror (column of mirrors) is in the ON state. Figure 7.22 shows the reflected response from two fiber Bragg gratings. The x-axis can be displayed in either pixels or directly on calibrated wavelength units (nm) as in Fig. 7.22. If displaying the x-axis as wavelength in [nm], the 5th-degree polynomial

coefficients giving the relation between the pixel number and the wavelength are utilized:

$$\lambda[nm] = A + B_1 pix + B_2 pix^2 + B_3 pix^3 + B_4 pix^4 + B_5 pix^5. \qquad (7.1)$$

The wavelength calibration coefficients are saved in a text file and are created during factory calibration process. Each channel has its own set of calibration coefficients.

The wavelength graph (see Fig. 7.22) shows the calculated center wavelengths of the FBG peak(s) versus time. To calculate the Bragg wavelength one of 5 fitting algorithms can be used: Center of Gravity (COG), Gaussian fitting, Dual-Weighted averaged COG (DWA), Linear Phase operator (LPO) [57] and Dynamic Gate algorithm (DGA), which was described in details in chapter 4.

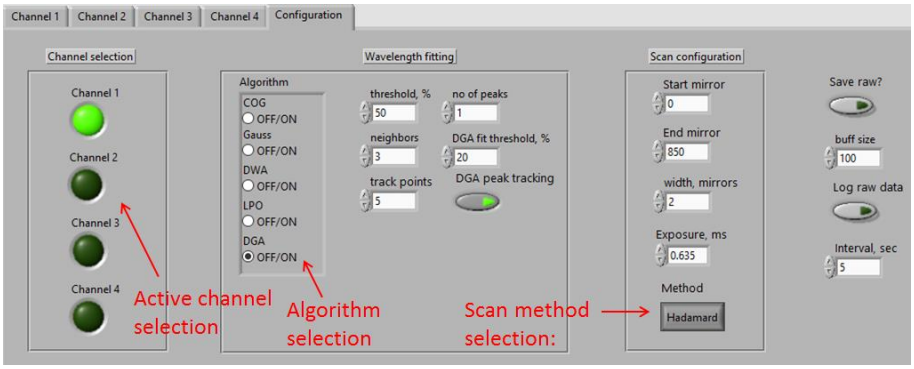

Figure 7.23. I-MON DMD software – configuration tab.

The configuration tab, shown in Figure 7.23, includes controls for optimizing measurements. One can select the active channel(s) by clicking on green buttons on the left. The algorithm can be selected from the Algorithm selection window, 5 algorithms are available. When the DGA is selected the Peak tracking feature, which was described in Chapter 4, can be used to track peaks. One can also select "pixel width" – how many mirrors are turned ON simultaneously. For instance, if Width=2 it means that 1 pixel is equal to 2 mirrors, this will decrease the sampling and may affect the resolution, but can increase the speed of scanning and also the intensity of the measured signal. This can be used when the broad FBGs are measured and good sampling is not required. It should also worth to mention that due to hardware limitations the DLPC150 controller can stream maximum 628

patterns to the DMD. The DMD has 480 by 854 mirrors. Thus, it is not possible to scan the whole DMD (854 mirrors) with the highest sampling, when the pixel width is 1 mirror. The whole DMD can be scanned with Width=2. One can also change Start and End mirrors, all mirrors to the left of the Start and to the right of the End will not be used. By doing this one can select area of interest on the scanned spectrum and use only mirrors within this area. This can also increase the scan time.

Raw data, which is unprocessed spectra, can be saved by clicking on Save Raw button. The raw data can be then post-processed by special Raw Calculation software, which has also been written in LabView. The Raw Calculation software can post-process raw data saved with the new interrogator and also with current I-MON interrogators and is widely used by my colleagues from the TRIPOD project.

Finally, one can select one of two scan methods: Column or Hadamard. Column scan selects one "pixel" (mirror) at a time. Hadamard scan creates a set with several mirrors multiplexed at a time and then decodes the measured spectrum. The Hadamard scan collects much more light and offers greater SNR than column scan.

7.4.2 Scan method: Column and Hadamard

The simplest sweep column scan scheme of measuring a spectrum using the DMD is detecting one wavelength at the time by turning on micromirror columns one by one through the whole spectrum. Let us consider a simple DMD with only 7 columns (or rectangular mirrors). In the sweep column scan method mirrors are turned ON one after another, so r_1 is the measured value by the detector when the first column is in the ON state. The measured spectrum, in this case, is set of readings $r_1, r_2, r_3 \ldots r_n$. Taking into account that each reading r_i also contains error e_i, the measured values can be written as:

$$\begin{aligned} r_1 &= I_1 + e_1, \\ r_2 &= I_2 + e_2, \\ &\ldots \\ r_7 &= I_7 + e_7, \end{aligned} \tag{7.2}$$

where I_i is the actual value of intensity.

Another scheme to acquire a spectrum is Hadamard spectroscopy [87]. The main advantage of this method is the improved SNR compared to the standard scheme. The digital nature of the DMD allows to efficiently implement this method. The idea of the Hadamard scan is to use special patterns, which can be generated from the Hadamard matrices. Let consider the same DMD with 7 columns, which is now scanned with Hadamard scan method:

$$\begin{aligned} r_1 &= I_1 + I_3 + I_5 + I_7 + e_1, \\ r_2 &= I_1 + I_2 + I_5 + I_6 + e_2, \\ &\dots \\ r_7 &= I_2 + I_3 + I_4 + I_5 + e_7. \end{aligned} \tag{7.3}$$

Now the first reading r_1 is the sum of intensities (signals) reflected from the first, third, fifth and seventh column and, of course, error e_1. The next patterns contain different sets of columns in the ON state, but always half of the columns are in the ON state. (To be precise, the S-matrices contain odd number of row and columns (n x n), so usually (n+1)/2 mirrors are in the ON state). Since half of the mirrors are in the ON state, it makes the intensity of the detected signal r_i higher and random noise lower compared to the standard sweep column scan. The SNR increases $\sqrt{n}/2$ times compared to the SNR achievable in the sweep column scan method [86], where n is the number of mirrors used. The output spectrum is calculated by multiplying the measured values by the inverse S-matrix:

$$I_n = S_n^{-1} r_n, \tag{7.4}$$

where I_n is the vector of unknowns, S_n^{-1} the inverse S-matrix and r_n is the vector of the measured values. An S-matrix S_n is constructed by taking a Hadamard matrix H_n and deleting the first row and column. All 1's are then replaced by 0's and all -1's replaced by 1's. The Hadamard matrix can be constructed using the Paley construction method [87]. The result matrix is then used to stream patterns to the DMD in such a way so that the first pattern is the first line, second pattern – the second line of the matrix, etc. The matrix generation and pattern construction algorithm has been implemented by Texas Instruments in the Nano EVM electronics and is performed by the Tiva TM4C1297 microprocessor. The decoding algorithm

has been done by calling a custom build dll file from the described LabView software.

The practical evaluation of the Hadamard scan method and comparison it with the standard sweep column scan method will be done in the next chapter.

7.5 Scanning speed

There are few factors, which limits the scanning speed. The first parameter is the micromirror switching time, which means how much time it takes to be set in the ON/OFF state. For the DLP2010NIR the micromirror switching time is 6 microseconds. It means that it requires 854*0.006ms=5.124 ms to scan the whole DMD. In theory, it gives 1000/5.124=195 Hz of the scanning speed. However, the maximum number of pattern, which can be sent to the DLP2010NIR, is 628, which covers 74% of the whole surface, in this case the theoretical scanning speed is 1000/(628*0.006)=265 Hz. One should note that the scanning speed is inversely proportional to the number of active mirrors, which can be decreased. For instance, one can select an active area with 50 pixels, which gives 1000/(50*0.006)=3.3 kHz of the theoretical scanning speed and this value is comparable to a typical speed of conventional CCD-based interrogators.

However, there is another very important parameter, which contributes the most to the scanning speed – the exposure time of the detector. The presented interrogator is based on the Nano EVM electronics, which uses Hamamatsu G12180-010A InGaAs photodiode. The shortest exposure time is 0.635 ms and this value is ~100 times bigger compared to 0.006 ms of the mirror switching time. It means that in the case of scanning the whole DMD by streaming 400 patterns with mirror width=2, the scanning speed is 1000/(400*(0.635+0.006))=3.9 Hz. In the case of selected area of 50 pixels, the scanning speed is about 31 Hz. These values are far from the theoretical values. The scanning speed can be further improved by developing a new electronics and using another detector, which lead to the decrease of the exposure time. The theoretical limit is constrained by the micromirror switching time and it looks quite competitive.

7.6 Conclusions

In this chapter we described the architecture of a novel type of multichannel DMD based interrogator, where the linear detector is replaced with a commercially available Digital Micromirror Device (DMD). The DMD is typically cheaper and has better pixel sampling than an InGaAs detector used in the 1550 nm range, which may lead to cost reduction and better performance. Three different concepts have been presented and compared. Original optical design, which utilizes advantages of the retro-reflect scheme, has been developed in Zemax. Due to the fact that the DMD is a 2D array, multichannel systems has been implemented without any additional optical components, which makes the proposed interrogator highly cost-effective, in particular when used in multi-channel systems. To operate the interrogator LabView software has been written. The software supports the presented in Chapter 4 new Dynamic Gate algorithm (DGA). Two methods of scanning - sweep column scan and Hadamard scan, which are fully supported by the software, have been described.

Chapter 8

New DMD-based interrogator: practical evaluation

This Chapter along with graphs, tables and images is partly based on the following publication: "Compact multichannel high-resolution MEMS-based interrogator for FBG sensing" [88].

In the previous chapter architecture of the new DMD based FBG interrogator has been described. In this chapter we present a practical evaluation of the new interrogator. The chapter is divided into two parts. In the first part we show in-lab tests and measurements, which include measurements of the most important properties and characteristics of each interrogator: optical resolution, wavelength fit resolution, accuracy, temperature, and polarization wavelength shift. It continues in the second part with strain and temperature measurements of real FBG sensors, including FBGs in multimode fibers.

The presented spectrometer based interrogator has 4 optical fibers as input, where each fiber is a standard telecom single mode SMF-28 fiber. The input wavelength range is from 1525 to 1570 nm. Figure 8.1

shows the assembled prototype of the interrogator without (a) and with the lid (b).

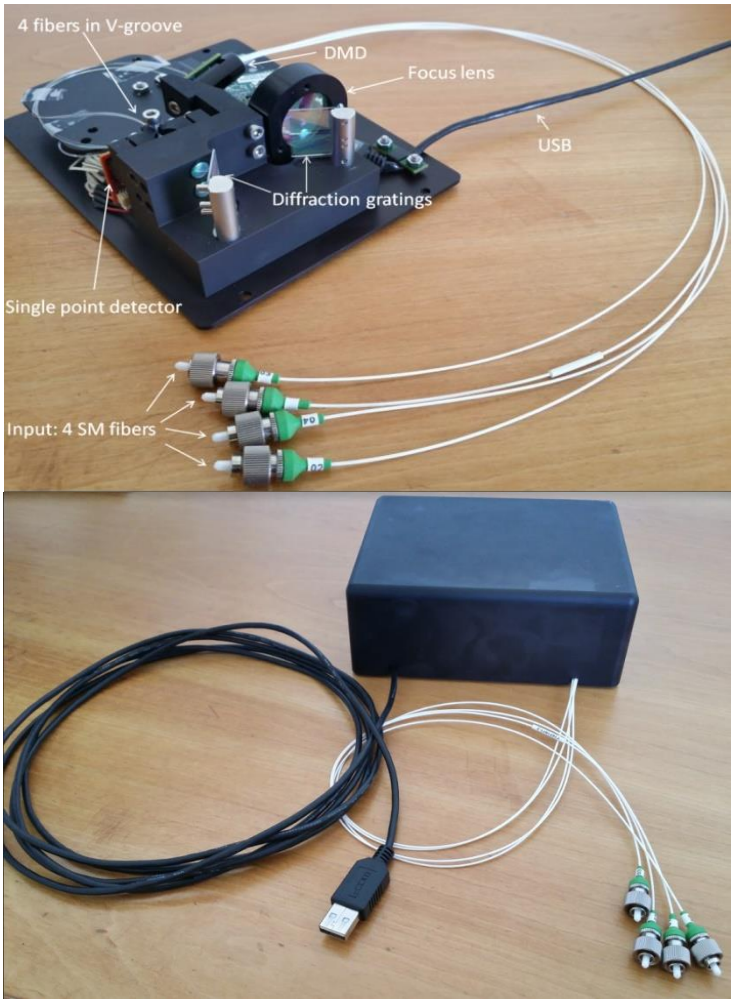

Figure 8.1. The assembled prototype of the new interrogator (a) top – without the lid and (b) bottom – with the lid.

8.1 In-Lab tests

8.1.1 Channel separation

The design, describe in the previous chapter, has been made in such a way to avoid channel cross talk caused due to a spatial overlap (see

Figure 7.12). Here the 2D digital nature of the DMD chip is used. Each channel is scanned separately one by one.

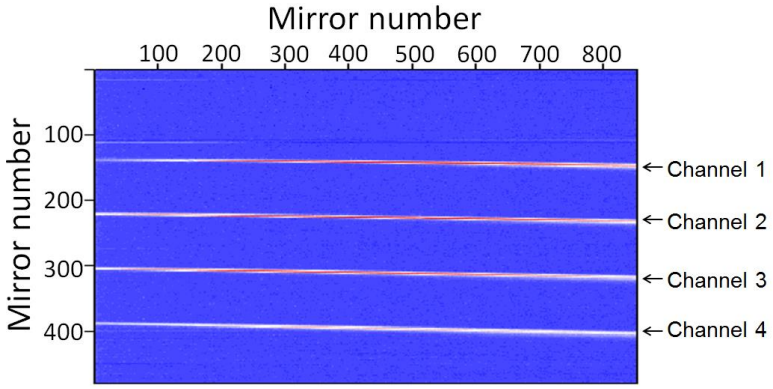

Figure 8.2. Measured distribution and channel separation in the DMD plane.

Figure 8.2 shows the measured distribution of the signal in the DMD plane when a broadband light source was connected to all 4 inputs. To obtain this image we scanned the whole area of the DMD by consequently turning each pixel of the DMD one after the other. Figure 8.2 proves the initial concept and signal distribution simulated in Zemax.

8.1.2 Optical resolution

One of the most important characteristics of each spectrometer is the optical resolution, which is usually is defined as the spectral width measured by the instrument of a spectrum with zero width. It is typically specified in full-width half-max (FWHM), defined as the width of the spectral peak when its height is 50% of the peak value. To measure the optical resolution we used a tunable laser source (JDS SWS 17101) with a line width of 100 MHz, which is ~0.8 pm in 1550 nm. It means that the signal peak width is almost zero compared to the theoretical optical resolution, calculated in Chapter 7.

Figure 8.3 shows the optical resolution of the new interrogator vs input wavelength. Laser spectrum has been measured by the interrogator and then the Gaussian fitting has been used to obtain the FWHM of the peak. Due to the imperfection of the optical components, the FWHM slightly varies from 120 pm for Channel 1 to 165 pm for Channel 4.

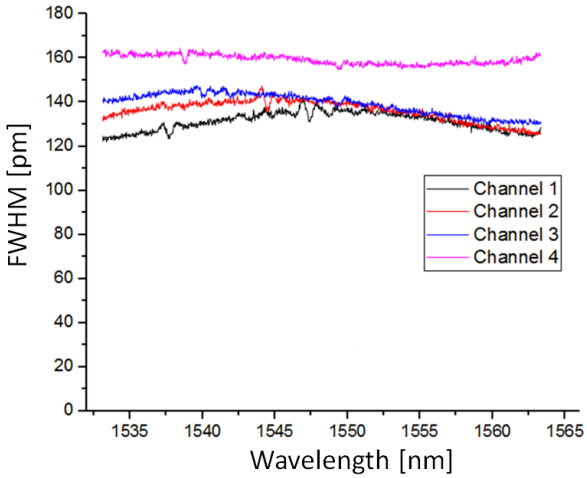

Figure 8.3. Measured optical resolution (FWHM) of the new interrogator.

The optical resolution corresponds well with the theoretically calculated values from section 7.2.2 (Table 7.1). Of course, those theoretical values have been calculated for the perfectly aligned system with perfect components (lenses, gratings, fibers), so it is not surprising that there are some deviations with the real assembled system. In terms of sampling, the FWHM varies from 2.2 to 3.1 pixels per spot. That means that we should not expect significant undersampling noise. The presented values show that the optical resolution is good enough to clearly resolve even very sharp single-mode FBG peaks with 200 pm width. The new interrogator has an optical resolution more than 2 times better that the current state-of-the-art spectrometer based interrogator produced by Ibsen Photonics (I-MON USB), which has the optical resolution of ~330 pm. Thanks to a higher sampling of the DMD compared to the InGaAs detectors.

8.1.3 Wavelength fit resolution

The basic principle of FBG sensing is to track the FBG peak position. The resolution in the detected FBG peak position is often called Wavelength Fit Resolution (WFR) and mainly depends on 3 parameters [54]: (a) the signal-to-noise ratio (SNR) of the input signal; (b) the peak shape of the measured signal; (c) the selection of the

fitting algorithm. The WFR is one of the most important characteristics of each interrogator.

The most important parameter is the SNR of the measured signal. To investigate this dependence and exclude the other factors as input we used a tunable laser source (JDS SWS 17101) with Gaussian shaped peak, where wavelength was fixed. The output power has been varied from -7 to -65 dBm with a step of 1 dB.

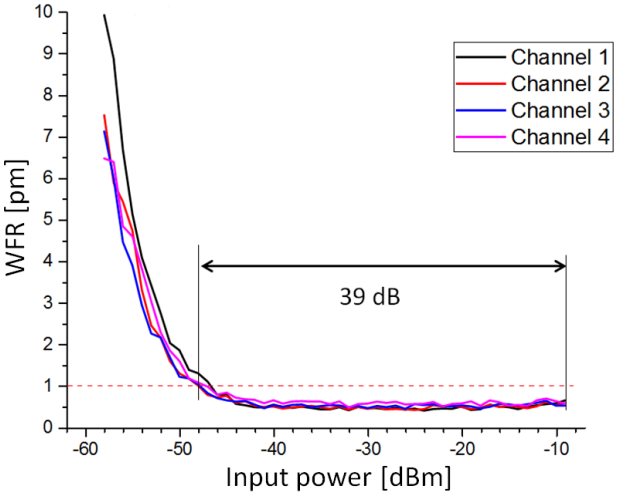

Figure 8.4. Wavelength fit resolution vs. input power.

The WFR was calculated as the standard deviation over 100 measurements per each value of the output laser power:

$$WFR = \sqrt{\frac{1}{N}\sum_{i=1}^{N}(x_i - \mu)^2}, \tag{8.1}$$

where $\mu = \frac{1}{N}\sum_{i=1}^{N} x_i$ and x_i is the calculated peak position at the ith repetition, ***N***=100 here. The integration time was constant during the whole experiment. Figure 8.4 shows the WFR vs. input power calculated for all channels. A typical value of the WFR is ~0.5 pm, which means that if the FBG peak shifts more than 0.5 pm it can be detected by the presented interrogator. Despite the slightly different optical resolution, the fit resolution is the same for all 4 channels. The dynamic range, where the WFR is less than 1 pm, is 39 dB.

8.1.4 Accuracy

Linear array detectors have successfully proven themselves in conventional spectroscopy. They measure dispersed light and represent a spectrum with high accuracy, even though they have some intrinsic problems like photo response non-uniformity (PRNU) and pixel cross-talk (discussed in Chapter 6), which lead to spectral distortion. Compared with this the DMDs are more uniform, but they also have micromirror tilt angle tolerance, which represents the tilt angle variation and the variation that can occur between any two individual micromirrors. These uncertainties can dramatically affect the measured spectra. In the previous chapter tolerance analysis has been done, where we showed that in the current design micromirror tilt angle error should not have a big influence on the measured spectrum. In order to prove this statement and we carried out an experiment, where we compared the measured wavelength with the reference. We used the same laser source as in the previous sections. The laser wavelength was varied from 1534 nm to 1567 nm with a step of 25 pm. The output from the laser was split into two paths, one path was connected to the spectrometer and the second one was connected to a high precision multi-wavelength meter (Hewlett Packard 86120B). Spectra were measured by the spectrometer and then Gaussian fitting (since the laser output is Gaussian shaped) was applied.

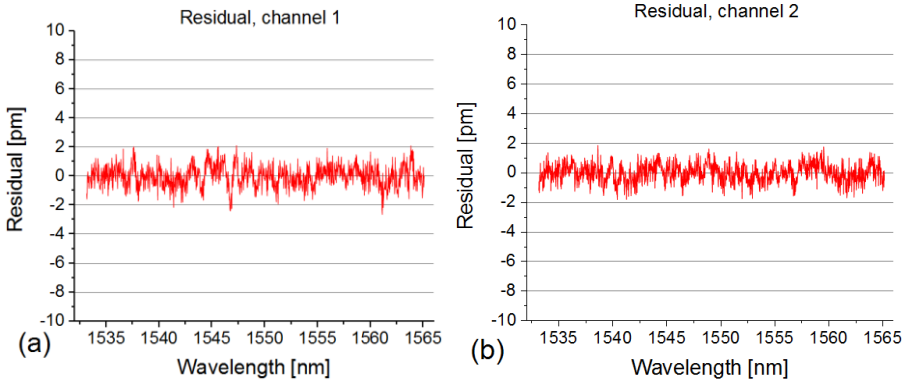

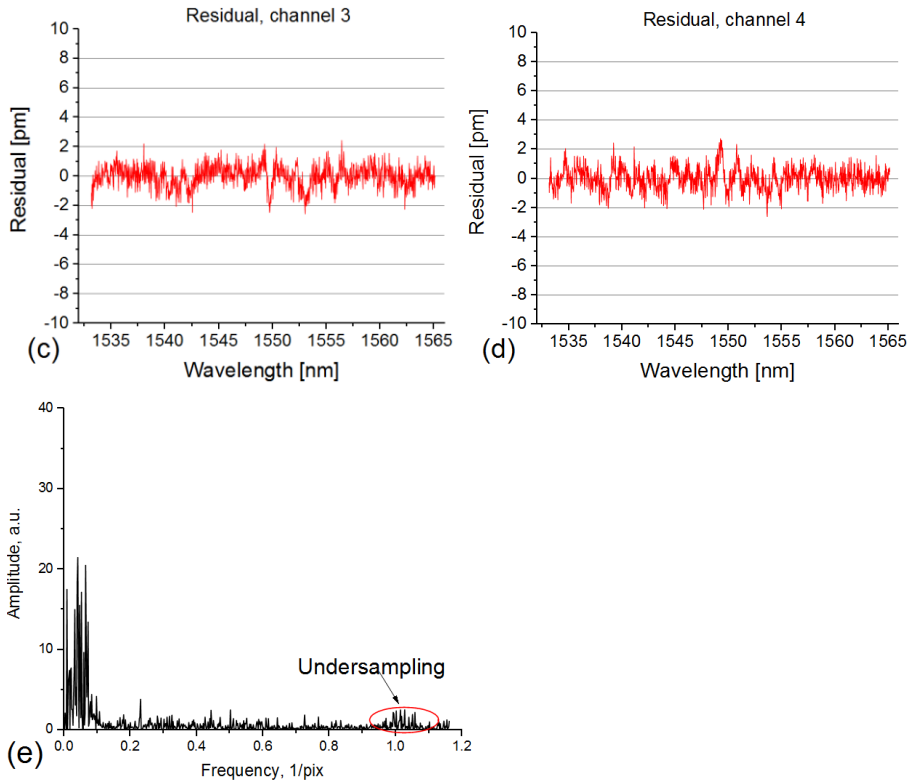

Figure 8.5. Spectrometer accuracy – difference between the measured and reference wavelength for all 4 channels (a,b,c,d) and (e) FFT of the residual of the 1st channel

Figure 8.5 shows the wavelength dependence of the residual of the difference between the wavelength measured by the interrogator and the wavelength, measured by the wavemeter for (a) Channel 1, (b) Channel 2, (c) Channel 3 and (d) Channel 4. As can be seen, the difference is less than 2 pm (typically ±1 pm), which includes laser noise (around ±1 pm according to the specifications), electronics readout noise, wavemeter errors. Figure 8.5 (e) shows the FFT image of the residual of the Channel 1, which has the highest resolution and therefore the highest potential undersampling. One can notice very small undersampling noise with frequency around 1/pix. However, the amplitude is very small and the noise is barely visible. One can also notice that the FFT has no clear frequencies from gratings caused by

the grating internal reflection (discussed in Section 6.1.1). It means that the new method of internal reflection suppression is very efficient.

Figure 8.5 shows that the DMDs can be used in high-resolution spectroscopy and in FBG interrogation field, where FBG peak position should be determined with very high precision and accuracy. However, one should add that the micromirror angle tolerance should be taken into consideration during optical design development.

8.1.5 Hadamard scan method

In the previous chapter the Hadamard scan method has been presented and described. The main advantage of this method is the improved SNR compared to the standard scheme. The SNR increases $\sqrt{n}/2$ times compared to the SNR achievable in the sweep column scan method [86], where n is the number of mirrors used. The output spectrum is calculated by multiplying the measured values by the inverse Hadamard matrix. According to the theory, for n=600 the SNR increases 12.2 times, which is 10.9 dB.

Figure 8.6 (a) shows an improvement of 9 dB in the SNR between the Hadamard and column scan methods, which is close to the theoretically predicted value of 10.9 dB. The SNR was measured as:

$$SNR = 10\log_{10}\frac{A_{sig}}{A_{noise}}, \tag{8.2}$$

where $\boldsymbol{A_{sig}}$ and $\boldsymbol{A_{noise}}$ are amplitudes of the signal and noise measured at the same point. Here we used the same laser source as in the previous sections with wavelength fixed to 1550 nm and intensity varied from -70 to -8 dBm.

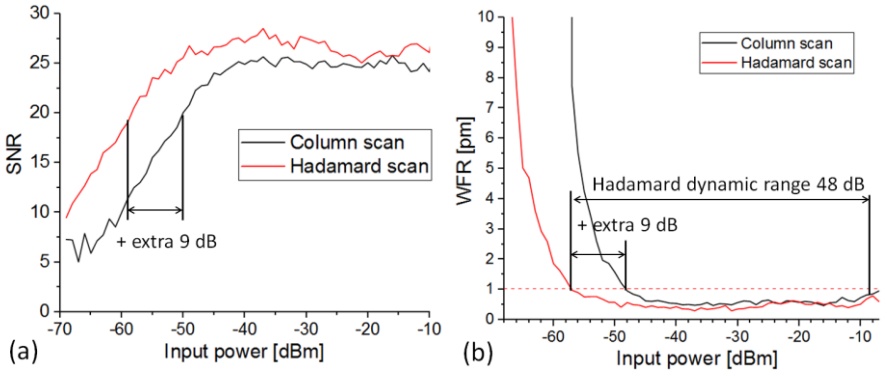

Figure 8.6. Comparison between the Hadamard and standard sweep scan methods: (a) SNR; (b) Wavelength fit resolution.

When the signal is weak (from -70 to -45 dBm) the detector noise, which includes dark noise, readout noise and digitization noise, dominates and the Hadamard method shows much higher SNR. When the signal becomes strong (-45 dBm and higher) the photon noise dominates and the SNR for the Hadamard and sweep column scan methods are almost similar [89]. Figure 8.6 (b) confirms the fact that the WFR strongly depends on the SNR – the increase of the dynamic range is also 9 dB when the Hadamard method is selected. The dynamic range equals a spectacular 48 dB for the Hadamard scan method.

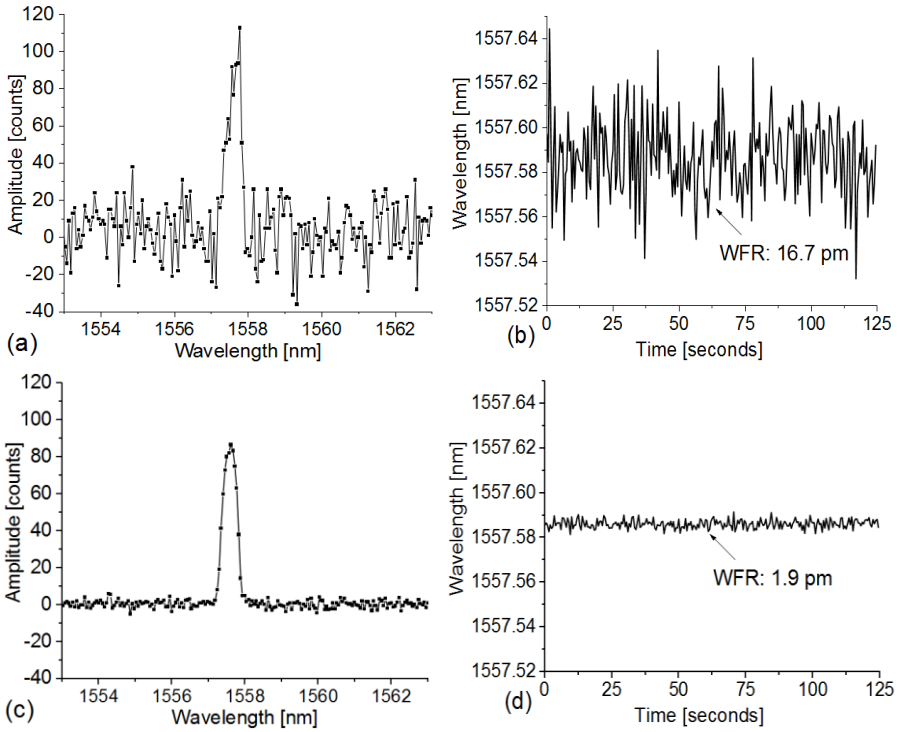

Figure 8.7. Column scan method: (a) FBG reflection spectrum; (b) tracked WL vs time; Hadamard technique: (c) FBG reflection spectrum; (d) tracked WL vs time.

Figure 8.7 shows the reflected spectrum of single-mode FBGs measured by the interrogator using the standard sweep column scan

(a) and the Hadamard technique (c). As can be easily noticed, on the top left image the FBG peak is barely visible and the noise is very high. The WFR is around 16.7 pm (Fig. 8.7 (b)). When the Hadamard method was used to interrogate the same FBG, the WFR was improved up to 1.9 pm (Fig. 8.7 (d)) and the spectrum contains less noise and the FBG peak can be clearly distinguished (see Fig. 8.7 (c)). These results show that the Hadamard scanning method greatly expands the dynamic range. For weak signal, when the detector noise dominates, it improves the SNR and, more importantly, the wavelength fit resolution of the interrogator.

8.1.6 Repeatability and Polarization Stability

Having an interrogator, or spectrometer, with great performance is very attractive but another important parameter is how stable this performance is. In this section we investigate how changes in polarization of the input light affect the performance. In these experiments the polarization of the input light was rotated 360 degrees. The polarization-dependent wavelength shift (PDW) is defined as the peak-to-peak variation of the measured wavelength over 100 measurements. Figure 8.8 (a) shows that the PDW typically equals to 3 pm and compared to the noise. It means that changing the polarization of the input light doesn't significantly affect the device performance.

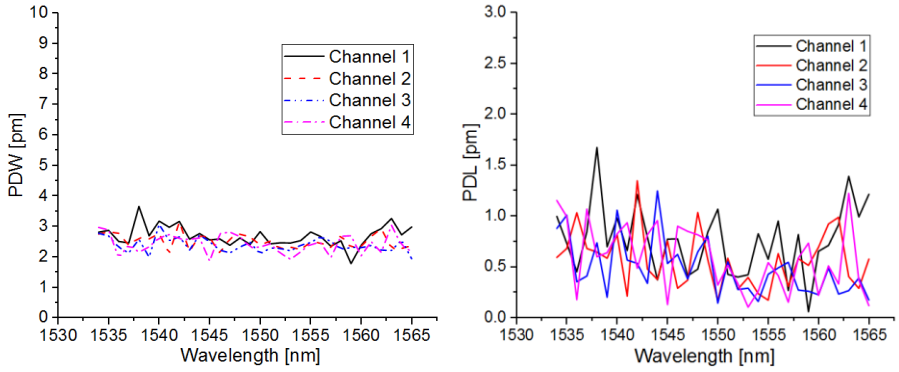

Figure 8.8. (a) left - Wavelength shift induced by polarization change, (b) – right – polarization dependable loss (PDL).

Polarization dependent loss (PDL) is the ratio of the maximum and the minimum intensities of the measured signal with respect to all polarization states. Polarization Dependent Loss, PDL, is defined as:

$$PDL = 10\log_{10}\frac{I_{\max}}{A_{\min}}, \tag{8.3}$$

where I_{max} and I_{mn} are maximum and minimum intensities of the measured signal. Figure 8.8 (b) shows the PDL for all channels of the interrogator. A typical value of the PDL is around 1 dB and it corresponds with the typical PDL of the state-of-the-art spectrometer based interrogators. One can add that PDL is not the most important characteristic of the interrogator.

8.1.7 Thermal behavior and compensation algorithm

Many spectrometers never leave labs and work in almost ideal conditions; however, for compact devices, the application field is much larger and quite often it is not an ideal and stable lab condition. It is very important to investigate how the proposed interrogator behaves under different temperatures.

Change of the environmental temperature can affect the performance of the interrogator. There are three primary factors to consider. First, the index of refraction of glass depends upon both temperature and wavelength; relative indices which are measured with respect to air also change with pressure. Second, glass expands and contracts with temperature, which can change the radius, thickness, or other dimensions of a lens. Third, the distances between lenses changes due to the expansion and contraction of the mounting material. The thermal analysis features provided by Zemax can account for all these effects.

Figure 8.9 (a) shows the thermal shift induced by the temperature change calculated in Zemax using thermal analysis for each wavelength. Thermal shift equals to the difference between the wavelength under changed temperature and the wavelength when the temperature was 25 °C.

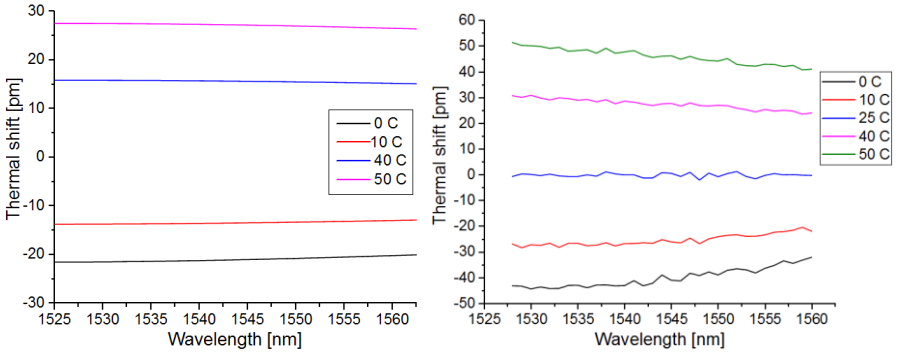

Figure 8.9. (a) left - Temperature drift simulated in Zemax, (b) right - measured thermal shift.

Figure 8.9(b) shows the experimental data. In the experiment the interrogator was cooled down to 0 °C then heated up to 10 °C, 40 °C and 50 °C and then the temperature was cooled down again to 25 °C. The interrogator was calibrated before the experiment. When the temperature reached the selected values (0 °C 10 °C, 40 °C and 50 °C it was kept constant during 2 hours before each measurement to stabilize the temperature inside. Thermal shift equals to the difference between the measured value and the reference value obtained with the same setup as in the previous sections. The maximum shift is around 50 pm for 25 °C change, which gives 2 pm/°C in average. One can notice that curves in Figures 8.9 (a) and (b) are similar, the difference is in the magnitude of the effect. In the real device, the total shift is 1.7 times higher than in the simulations.

The temperature shift can be compensated by using the approach described in Chapter 6 (section 6.4). The main idea is to change the original calibration polynomial by adding polynomial ***D(p)***, which fits a set of thermally induced deviations.

By knowing these polynomials for each temperature the calibration polynomial can be changed and induced thermal shift can be compensated. However, it is almost impossible to obtain a thermally induced curve for each temperature, since a lot of experiments should be carried out and a lot of data have to be saved. It would be much

easier if we could analytically have an equation, which describes the wavelength shift for each wavelength.

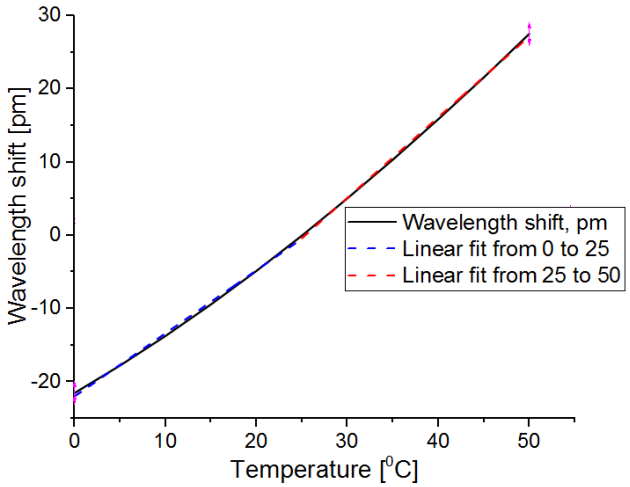

Figure 8.10. Thermal shift for the central wavelength of 1547 nm calculated in Zemax.

We used Zemax to investigate the wavelength shift induced by temperature for fixed wavelength, which is shown in Figure 8.10. Despite the shift is not linear it can be fitted with 2 first-order polynomials (red and blue dashed lines in Figure 8.10) – one linear curve can be used to fit data from 0 °C to 25 °C (blue line) and another to fit data from 25 °C to 50 °C (red line).

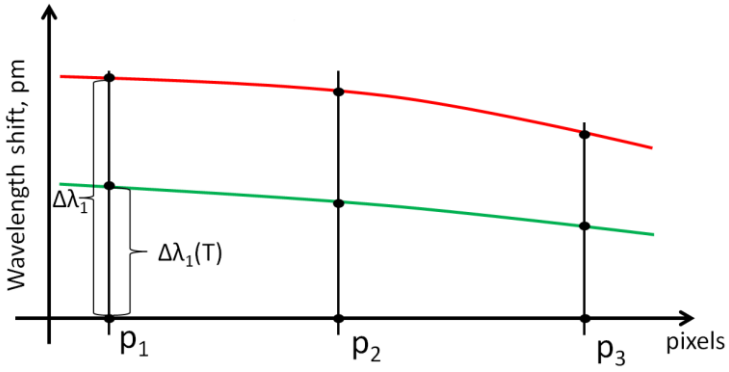

Figure 8.11. Thermal shift polynomial behavior.

Let us consider the interrogator's behavior from 25 °C to 50 °C. Let $\boldsymbol{D_{50}(p)}$ is a polynomial, which fits the wavelength shift points for T=50 °C (red curve in Figure 8.11) with known coefficients, which can be

found experimentally. Here we want to find how these coefficients change when temperature changes between 25 °C and 50 °C. Let consider a polynomial $D_T(p)$, which fits the wavelength shift points induced by arbitrary temperature T (green curve in Figure 8.11) between 25 °C and 50 °C. Since the wavelength shift between 25 °C and 50 °C is linear to temperature change (Fig. 8.10) it means that:

$$\Delta\lambda_1(T) = \Delta\lambda_1(\frac{T}{25} - 1), \tag{8.4}$$

where $\Delta\lambda_1(T)$ and $\Delta\lambda_1$ are the temperature-induced wavelength shift for arbitrary T and for 50 °C and p_1 is the pixel position, which the input light with wavelength λ_1 hits when T=25 °C. Or in other words, $\lambda_1=C(p_1)$, where $C(p)$ is the original calibration polynomial, which is made when T=25 °C. We shall limit ourselves here, for the sake of simplicity, to the consideration of the second order polynomial $D_T(p)= a(T)p^2+b(T)p+c(T)$. As was mentioned before $D_{50}(p)=a_{50}p^2+b_{50}p+c_{50}$, where a_{50}, b_{50} and c_{50} are known coefficients (found experimentally). Equations, similar to Eq. (8.4) can be written for pixels p_2 and p_3. By knowing coordinates of three points of a parabola (x_1,y_1), (x_2,y_2) and (x_3,y_3) one can find its coefficients by the following equations:

$$a = \frac{y_3 - \frac{x_3(y_2 - y_1) + x_2y_1 - x_1y_2}{x_2 - x_1}}{x_3(x_3 - x_1 - x_2) + x_1x_2}, \tag{8.5}$$

$$b = \frac{y_2 - y_1}{x_2 - x_1} - a(x_1 + x_2), \tag{8.6}$$

$$c = \frac{x_2y_1 - x_1y_2}{x_2 - x_1} + ax_1x_2. \tag{8.7}$$

Now substituting expressions for $\Delta\lambda_1(T)$, $\Delta\lambda_2(T)$ and $\Delta\lambda_3(T)$ into equations (8.5-8.7) we can express $a(T)$, $b(T)$ and $c(T)$ in terms of coefficients a_{50}, b_{50}, c_{50} and temperature T:

$$a(T) = a_{50}(\frac{T}{25} - 1), \tag{8.8}$$

$$b(T) = b_{50}(\frac{T}{25} - 1), \tag{8.9}$$

$$c(T) = c_{50}(\frac{T}{25} - 1). \tag{8.10}$$

Equations (8.8)-(8.10) show that the coefficients ***a(T)***, ***b(T)*** and ***c(T)*** has also the linear dependence of temperature. Applying the same reasoning to the case when 0 °C<***T***<25 °C:

$$a(T) = a_0(1 - \frac{T}{25}), \tag{8.11}$$

$$b(T) = b_0(1 - \frac{T}{25}), \tag{8.12}$$

$$c(T) = c_0(1 - \frac{T}{25}), \tag{8.13}$$

where a_0, b_0 and c_0 are known coefficients of the polynomial, which fits the wavelength shift points for ***T***=0 °C.

The temperature compensation algorithm works as follows:

- Measure wavelength shift curves for 0 °C and for 50 °C;
- Fit the curves with second order polynomials and find a_{50}, b_{50}, c_{50} and a_0, b_0, c_0;
- Depending on the environment temperature find ***a(T)***, ***b(T)*** and ***c(T)*** using Eqs. (8.8)-(8.13);
- Correct the original calibration polynomial ***C(p)*** using found coefficients.

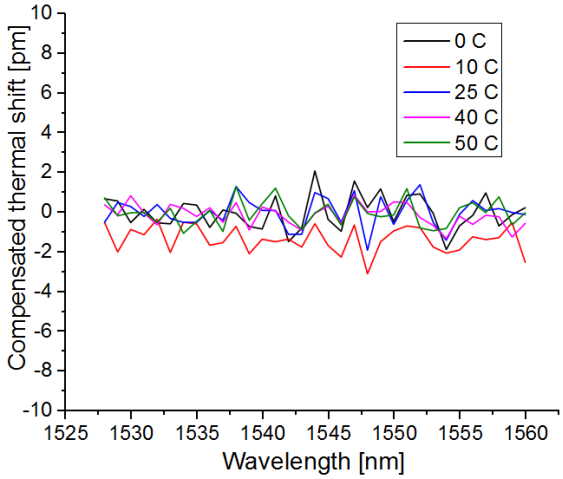

Figure 8.12. Compensated thermal shift.

Figure 8.12 shows the thermal shift compensated by the algorithm described above. The total shift is within ±2 pm. The Nano EVM electronics used in the interrogators contains two temperature sensors

– one on the main board and another on the detector board. These sensors allow to monitor the ambient temperature during measurements and by using the described above algorithm compensate the thermal induced shift.

Another potential problem, which may occur during the change of the ambient temperature, is an increase of the optical resolution, due to defocusing. The main reason of the defocusing is the same - the distances between lenses changes due to the expansion and contraction of the mounting material. We used data captured in the previous experiment and calculated how the optical resolution (FWHM) changes during the temperature change (Figure 8.13). As can be seen, the total increase is 20 pm, which is ~11%. This means that the temperature doesn't significantly affect the optical resolution.

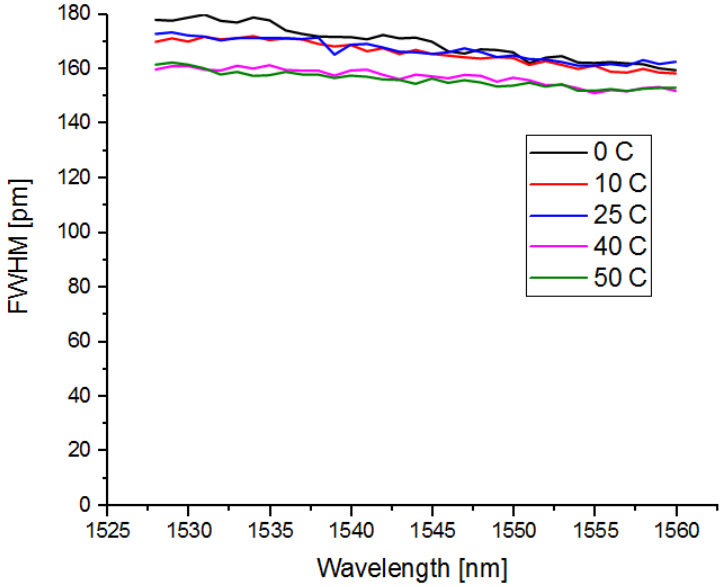

Figure 8.13. FWHM vs input wavelength under different ambient temperature.

Here we investigated theoretically and demonstrated practically how the interrogator behaves under temperature changes and showed that by using the temperature compensated algorithm the total thermal induced wavelength shift is compared to the noise and don't affect the interrogator performance. It means that the presented interrogator is quite robust and suites to field applications.

8.2 FBG measurements

8.2.1 Temperature and humidity measurements

It has been shown that when a silica FBG is embedded into a polymer structure it may change the temperature response of the FBG sensor due to the fact that polymer has much higher thermal expansion coefficient [90]. Our goal was to manufacture 3-D printed structures with 4 different polymers (PET-G, nylon 6, nylon 12 and ABS), then embed silica gratings onto these structures and measure the temperature response of each sensor simultaneously. Figure 8.14 shows the 3D view of the housing structure

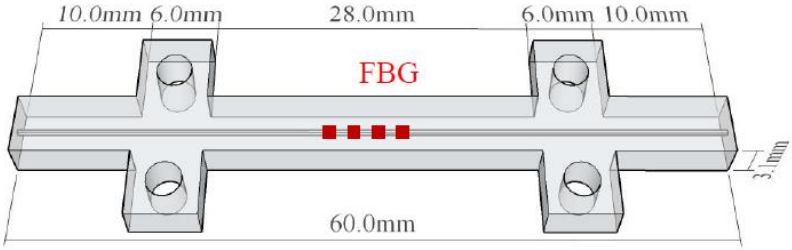

Figure 8.14. 3-D view of the housing structures. Dotted line marks the position in which gratings are embedded.

The polymer sensor manufacturing and embedding have been done together with my colleague Michal Zubel from Aston University in Birmingham, UK. Since polymers are also sensitive to humidity we used a chamber, where humidity can be controlled together with temperature. The FBG sensors along with with a thermocouple were installed and fixed inside the chamber. Before experiments, all 4 sensors have been annealed at 85 °C and 90 % of humidity during 24 hours.

In the first experiment relative humidity (RH) inside the chamber was kept constant and equal to 40%. After 1 hour of waiting under 25 °C, the temperature inside was linearly increasing up to 60 °C during 2 hours, then next 2 hours T was stabilized and equal to 60 °C and then the temperature was linearly decreasing during 2 hours back to 25 °C. Each FBG sensor was connected to separate channel of the described interrogator, thus all 4 sensors were interrogated simultaneously. The

FBG spectra were recorded every 20 s during 7 hours. Figure 8.15 shows the reflected spectra of all 4 sensors before the start of the experiment.

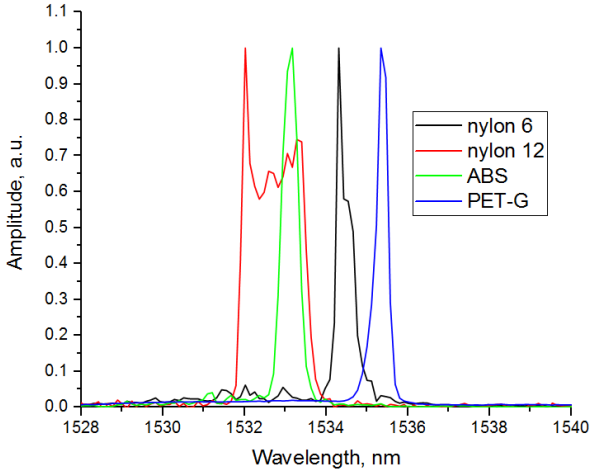

Figure 8.15. Reflected spectra from all 4 FBG sensors before the start of the experiment.

As can be seen, the spectra are partly overlapped, thus cannot be measured with a standard single-channel interrogator. The reflected spectrum from the sensor made of nylon12 (red color) has non-Gaussian double peak broad shape, therefore the DGA was selected to fit all spectra.

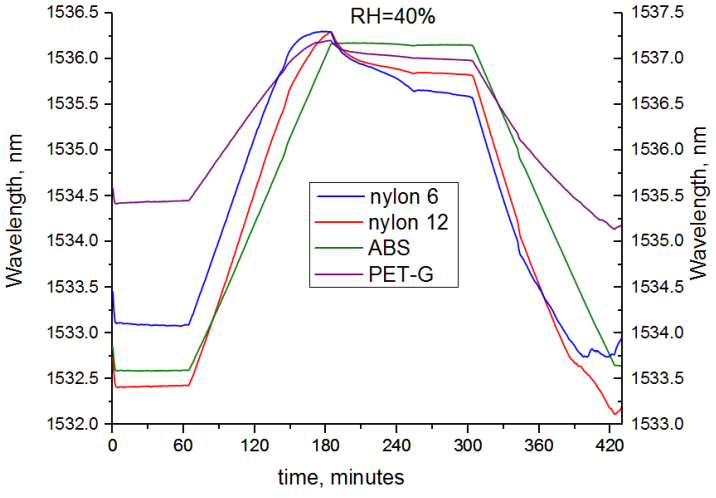

Figure 8.16. 4 sensors response, RH is 40%. The right Y scale is for nylon 6, the left is for the others.

The fitted Bragg wavelength vs time for all 4 sensors is shown in Figure 8.16. Table 8.1 shows a correlation between the coefficient of thermal expansion (CTE) of each material and measured sensitivity.

Table 8.1. Thermal sensitivity.

	ABS	PET-G	Nylon 6	Nylon 12
CTE, 1/K	$73.8*10^{-6}$	$59.4*10^{-6}$	$80*10^{-6}$	$80.5*10^{-6}$
Sensitivity, pm/°C	102.1	63.3	128.1	135.4

As can be seen, temperature sensitivity of the embedded sensors is 10-12 times higher than temperature sensitivity of unembedded silica gratings, which is around 10-12 pm/°C. Such an increase in temperature sensitivity comes probably from the fact that the linear CTE of the used polymers is around 10 times higher than the thermo-optic coefficient of silica, which mostly contributes to pure FBG thermal sensitivity. By using these sensors one can gain the temperature sensitivity by a factor of 10, thereby highly increasing temperature resolution of the FBG sensor system. Three sensors made of ABS, Nylon 6 and Nylon 12 have nearly the same thermal sensitivity, however, two of them (Nylon 6 and 12) show quite big hysteresis, whereas ABS demonstrates very low hysteresis. Figure 8.17 shows the hysteresis of the Nylon 12 and the ABS sensors.

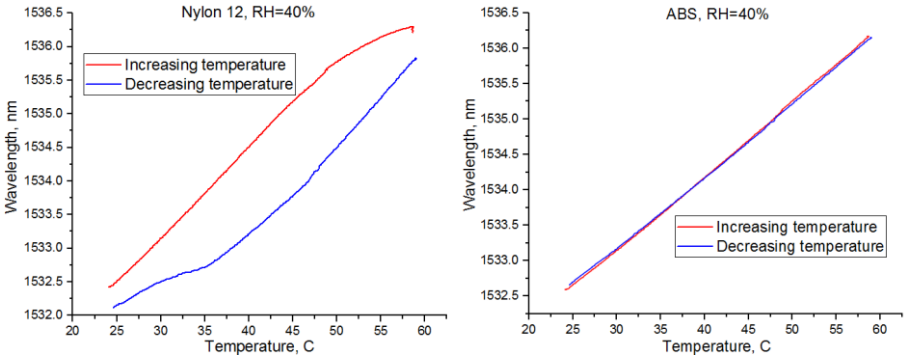

Figure 8.17. Thermal sensitivity of the Nylon 12 (left) and the ABS (right) based sensors.

The ABS based sensor shows the lowest hysteresis among all 4 sensors. Moreover, it also shows the best linearity.

Figure 8.18 shows results when the relative humidity inside the chamber was 60%. The temperature control was the same as in the previous experiment: 1 hour of stabilizing at 25 °C, 2 hours of linear increase from 25 °C to 60 °C, 2 hours of stabilizing at 60 °C and then 2 hours of linear decrease back to 25 °C.

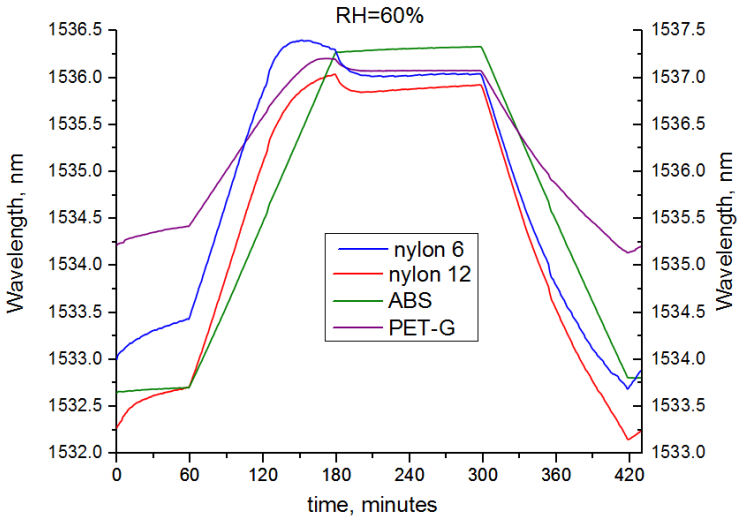

Figure 8.18. 4 sensors response, RH is 60%. The right Y scale is for nylon 6, the left is for the others.

Each sensor demonstrates different response, but the overall picture is the same as in the previous experiment. Table 8.2 compares the thermal sensitivity when RH=40% and when RH-60%.

Table 8.2. Thermal sensitivity.

	ABS	PET-G	Nylon 6	Nylon 12
CTE, 1/K	$73.8*10^{-6}$	$59.4*10^{-6}$	$80*10^{-6}$	$80.5*10^{-6}$
Sensitivity, pm/°C, RH=40%	102.1	63.3	128.1	135.4
Sensitivity, pm/°C, RH=60%	102	67.4	142.2	140.8

The ABS based sensors thermal sensitivity is insensitive to the relative humidity, whereas the other sensors show a small change of the coefficient. The biggest change is shown by the Nylon 6 based sensor – from 128.1 to 142.2 pm/°C, which is ~11%. The ABS based sensor also shows the lowest hysteresis. The results show that using,

for instance, the ABS sensor with the presented interrogator one can measure temperature with 0.005 °C resolution.

In the last experiment we studied how the reflected Bragg wavelength depends on the relative humidity inside the chamber. The temperature was kept constant and equal to 25 °C during the whole experiment. During the first 2 hours RH=40% and then during next 2 hours RH was linearly increased from 40 to 80%. Figure 8.19 shows the reflected Bragg wavelength relative shift.

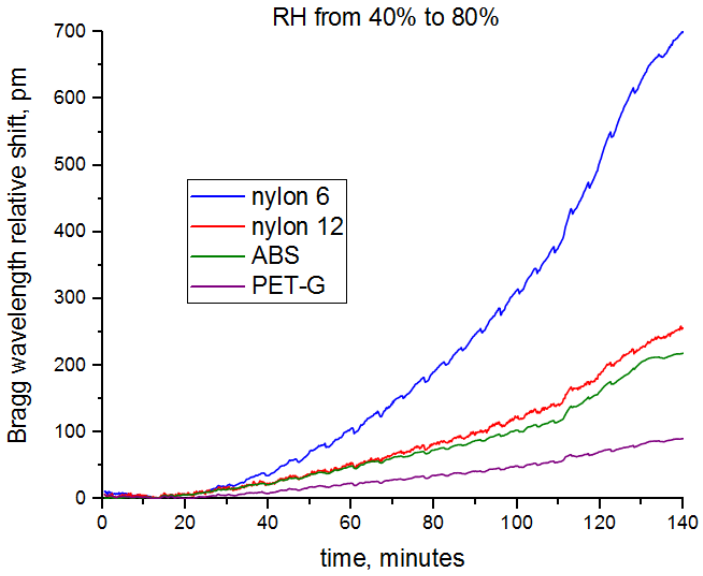

Figure 8.19. 4 sensors response, temperature is 25 °C, RH changes from 40 to 80%. The right Y scale is for nylon 6, the left is for the others.

The biggest sensitivity to the humidity is demonstrated by the Nylon 6 based sensor. This fact partly correlates to the fact that the Nylon 6 sensor shows the biggest change in the thermal sensitivity. The Bragg wavelength shift is not linear to time, however, it doesn't mean that the sensor cannot be used to RH sensing. The humidity control inside the chamber was not checked by an external device, as it was for temperature when the external thermocouple was used. Thus, it is doubtful that the humidity inside the chamber was changed linearly. The average sensitivity to humidity varies from 2.5 pm/% (PET-G) to 17.5 pm/% (Nylon 6), which means that, assuming 0.5 pm wavelength fit resolution, up to 0.03% of RH change can be resolved.

8.2.2 Study of properties of few-mode and multi-mode polymer FBGs

In these experiments we studied properties of few- and multi-mode polymer fiber Bragg gratings. In the first experiment we used a tapered CYTOP fiber with an FBG written by a femtosecond technique. The initial core diameter was 62 um and it was decreased down to 15 um, which means that the fiber can transmit only a few modes. The test setup is shown in Figure 8.20.

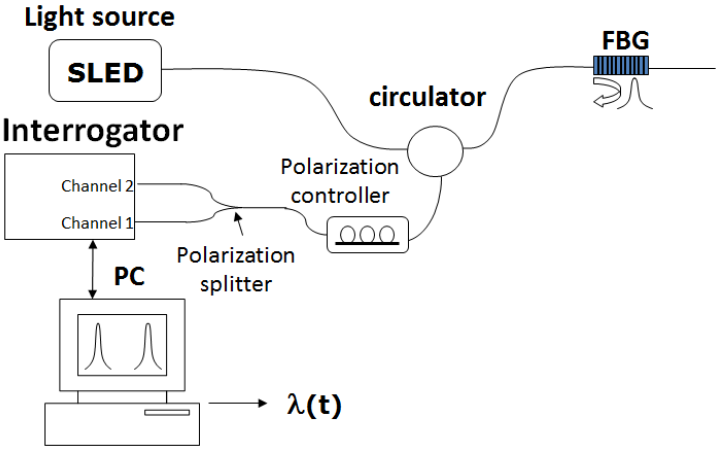

Figure 8.20. Test setup.

The light reflected from the FBGs is passing a manual polarization controller Thorlabs, which allows rotating the polarization, and then is split into 2 arms by the polarization splitter into its orthogonal linear polarizations through 2 fiber outputs, which are connected to the interrogator (Channel 1 and Channel 2).

Figure 8.21 (a) shows the reflected spectrum from the tapered FBG. The signals measured by the Channel 1 and 2 are completely different. Peak 1 and 2 are absent in Channel 2. When the polarization of the reflected light is rotated 90 degrees, spectra measured by Channel 1 and Channel 2 (Figure 8.21 (b)) are significantly changing and one can also notice that Channel 1 (0 state)=Channel 2 (90 degrees) and Channel 2 (0 state)=Channel 1 (90 degrees). This fact shows that the light reflected from the FBG is highly polarized.

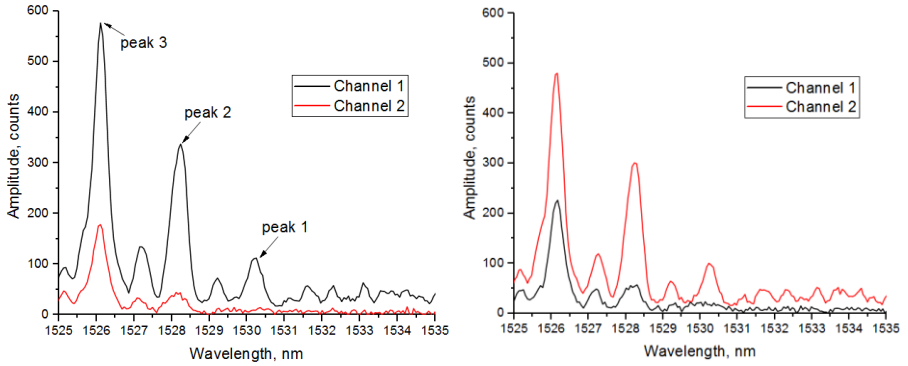

Figure 8.21. FBG reflected spectrum: (a) left - polarization controller on 0 state; (b) right – polarization controller on 90 degree state, polarization is linearly rotated on 90 degrees.

The fiber with the FBG was glued to two XYZ stages and coupled to an SMF28 fiber, which is connected to the new DMD-based interrogator (see Fig. 8.20). The strain was increased manually with a step of 125 με. The Hadamard scan method together with the DGA [54] was used to measure and calculate the FBG response. Figure 8.22 shows the FBG response under applied strain.

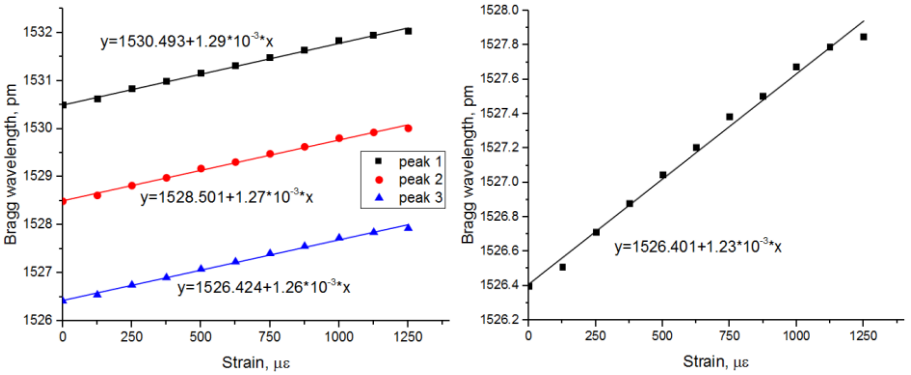

Figure 8.22. FBG strain response measured (a) left – in Channel 1; (b) right – in Channel 2.

Linear fitting was used to fit and calculate the response of each peak. The calculated strain response is 1.29±0.03 pm/με, 1.27±0.03 pm/με and 1.26±0.03 pm/με for peak 1, peak 2 and peak 3, respectively. The difference in the response is within the limits of error. Figure 8.22 (b) shows the response measured in Channel 2, where is only one distinguished peak. The response is 1.23±0.04 pm/με, which is slightly

different. However, the difference is still might be within the limits of error.

In the next experiment we used a highly multimode CYTOP fiber with an FBG. The core diameter is 62 um. We used the same setup as in the previous experiment (Fig. 8.20). Figure 8.23 shows the reflected spectrum split by the polarization splitter and measured simultaneously. In this case the peaks are better separated by the polarization splitter. The highest peak in the Channel 2 (Peak 2) is completely absent in the Channel 1, which means that the polarization of this peak is orthogonal to the Channels 1 polarization. The highest peak in the Channel 1 (peak 1) is partly presented in the Channel 2. It means that, despite these peaks are not fully orthogonal, they are partly separated and their polarizations are not the same. It proves the fact discussed in Chapter 5 – few-mode and multimode FBGs are very sensitive to polarization.

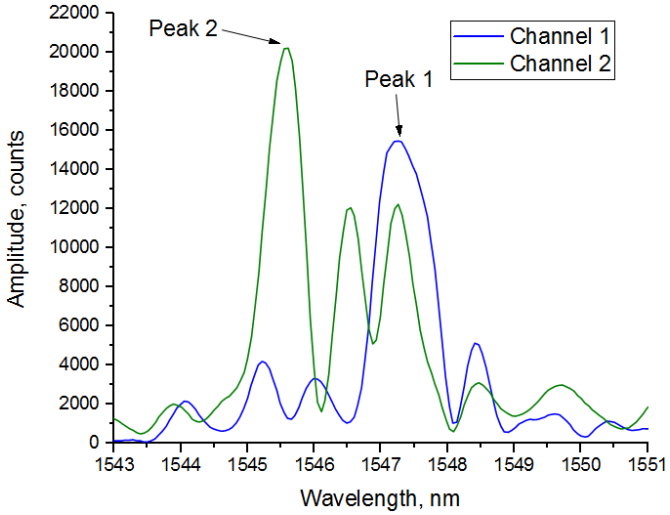

Figure 8.23. Highly multimode FBG reflected spectrum after polarization splitter.

The strain was increased manually with a step of 100 με. Figure 8.24 shows the fitted Bragg wavelength vs time. As can be seen, the response of Peak 1 is slightly different compared to the response of Peak 2. Figure 8.25 shows the Bragg wavelength shift vs applied strain for both peaks. The Bragg shift is the difference between the Bragg wavelength measured under applied strain and the initial value.

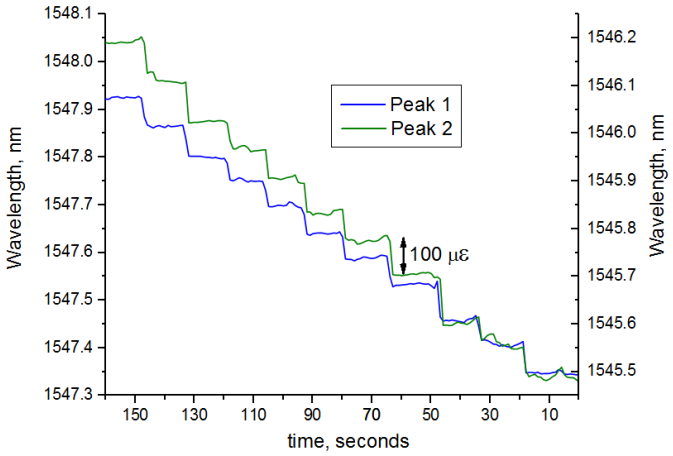

Figure 8.24. FBG reflected wavelength vs time. Left Y-axis is for Peak 1, right Y-axis for Peak 2.

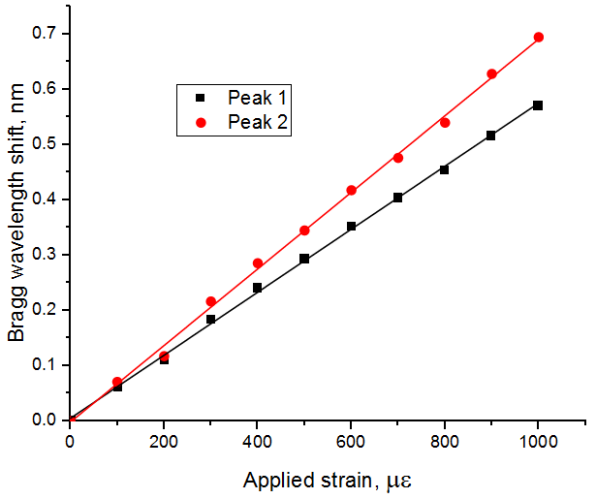

Figure 8.25. FBG strain response.

The calculated strain response is 0.57±0.01 pm/με and 0.69±0.01 pm/με for Peak 1 and peak 2, respectively. The difference is 21% and cannot be explained by the measurements errors, taking into account that they were measured simultaneously. One can clearly see that Peak 2 has a higher wavelength shift (Fig. 8.24 and 8.25). Ideally, when only longitudinal strain is applied all peaks should move in the same direction and with the same shift step. But our experiment shows that the strain response is different for different peaks reflected from the same FBG. This phenomenon needs further investigation.

8.3 Conclusions

In this chapter we presented results of practical evaluation of the new interrogator. In the first part we showed in-lab tests and measurements, which include measurement of the most important properties and characteristics such as optical resolution, wavelength fit resolution, accuracy, temperature and polarization wavelength shift. The measured optical resolution and wavelength fit resolution is typically 150 pm and 0.5 pm, respectively. The measured accuracy shows very small undersampling noise and the total deviation from the reference less than 2 pm. This fact means that DMDs can be used in high-resolution spectroscopy and in the FBG interrogation field, where the FBG peak position has to be determined with very high precision and accuracy. We have studied the thermal behavior of the interrogator. A temperature compensated algorithm has been presented, which makes the total wavelength shift induced by temperature change less than 2 pm. We have also investigated the polarization sensitivity of the device. Our results show that the presented interrogator is stable to temperature and polarization change and can be used in industrial-grade applications. Thanks to the Hadamard scan method one can improve SNR of the measured signal up to 9 dB and increase the wavelength fit resolution for a weak input signal.

In the second part we used the presented interrogator for strain and temperature measurements of real FBG sensors and multimode FBGs. We utilized a multiple channel feature and measured FBGs response simultaneously. We investigated the temperature response of silica FBGs embedded in 4 different polymer 3D-printed structures. We showed that one can increase the thermal sensitivity up to 10-12 times. Humidity sensing is also possible with such kind of sensors. We also investigated polarization properties and strain response of few- and multimode polymer FBGs. We showed that the strain response is different for peaks with different polarization reflected from the same FBG.

Chapter 9

Conclusions

Polymer optical fibers offer some key advantages over silica, however polymer fiber Bragg gratings are not highly commercialized and widely used. The aim of this project has been to improve the current polymer Fibre Bragg Grating (FBG) sensing technology by developing a new, high-quality interrogator for FBG sensor systems, which combines high performance with cost-effectiveness.

In Chapter 2 we described the principles of FBG sensing, starting with a short theory of FBGs and an overview of known interrogation techniques. Chapter 3 was dedicated to polymer FBGs from a historical perspective, FBG inscription techniques and a comparison of polymer FBGs to glass FBGs. We also described the latest progress in the polymer FBG field.

In Chapter 4 we presented an efficient and fast detection algorithm for FBG sensing based on a threshold-determined detection window and a bias-compensated center of gravity (COG) algorithm. This method avoids sudden shifts in the fitted wavelength and improves the wavelength fit resolution. Simulations and experiments demonstrated that the proposed algorithm is highly robust and has significantly improved wavelength fit resolution compared with conventional algorithms. Due to the fast demodulation speed, which is 10 times faster than Gaussian fitting, the proposed algorithm can be used in dynamic sensing systems with high-speed requirements. A new “peak tracking” mode helps to avoid jumps and shifts, which occur due to the peak ascending and descending phenomenon and together with the dynamic gate algorithm (DGA) makes the spectrum processing routine

more robust and stable. It has been shown that the new fitting algorithm together with the "Peak tracking" option can fit and track arbitrary changing multimode peaks in real-time. These properties make the DGA an attractive and suitable method for future implementation in sensing systems based on multimode fiber Bragg gratings.

In Chapter 5 we evaluated how detrimental the influence of higher-order modes is to the polarization stability and linearity of the strain and temperature response of an FBG sensor. We did this by comparing the performance of a few-mode 850nm FBG sensor using a standard 1550nm telecom fiber to a strictly single-mode 850nm FBG sensor system using an 850 nm single-mode fiber. Our results show that the polarization stability and linearity of the response degrade so much due to the presence of the higher-order modes, that in practice the sensor would not be usable for high-precision measurements, in contrast to what have been concluded in several earlier investigations. However, we showed that using the well-known technique of simple coiling of the few-mode fiber one can regain the single-mode performance of the multi-mode sensor system. These experiments, therefore, demonstrate that 850 nm FBG sensor systems can indeed in practice be based on low-cost 1550 nm telecom fibers, despite these being multi-mode at 850 nm.

In Chapter 6 we analyzed and investigated errors and drawbacks, which are typical for spectrometer-based interrogators: undersampling, grating internal reflection, photo response non-uniformity (PRNU), pixel crosstalk and temperature and long term drift. We showed how each of these problems impacts on the interrogator performance, and how to eliminate and improve them. However, some of the issues, like PRNU and pixel crosstalk, are intrinsic for CCD array detectors and therefore cannot be completely eliminated. These can be improved by changing the detector to a Digital Micromirror Device (DMD), which doesn't have these problems and also offers other advantages over conventional CCD detectors.

In Chapter 7 we described the architecture of a novel type of multichannel DMD based interrogator, where the linear detector is replaced with a commercially available Digital Micromirror Device (DMD). The main reason for using the DMD is that it is typically cheaper and has better pixel sampling than an InGaAs detector used in the 1550 nm range, which may lead to cost reduction and better performance. Three different concepts have been presented and compared in this chapter. Original optical design, which utilizes advantages of the retro-reflect scheme, has been developed in Zemax. Due to the fact that the DMD is a 2D array, multichannel systems can be implemented without any additional optical components, which makes the proposed interrogator highly cost-effective, in particular when used in multi-channel systems. To operate the interrogator LabView software has been written. The software supports the presented new Dynamic Gate algorithm (DGA). Two methods of scanning - sweep column scan and Hadamard scan - which are fully supported by the software, have been described and compared. The main drawback of the new interrogator, which is a relatively slow scanning speed, has also been discussed here. However, this parameter can be improved in future. Moreover, a high scanning speed of few kHz is not a necessity for most applications, where the speed of few tens of Hertz seems to be enough.

In Chapter 8 we tested the performance of the presented interrogator. In the first part, we showed in-lab tests and measurements, which include measurement of the most important properties and characteristics such as optical resolution, wavelength fit resolution, accuracy, temperature and polarization wavelength shift. The measured optical resolution and wavelength fit resolution is typically 150 pm and 0.5 pm, respectively. The measured accuracy shows very small undersampling noise and the total deviation from the reference less than 2 pm. This fact means that DMDs can be used in high-resolution spectroscopy and in the FBG interrogation field, where the FBG peak position has to be determined with very high precision and accuracy. We have studied the thermal behavior of the interrogator and presented a temperature compensation algorithm,

which makes the total wavelength shift induced by temperature change less than 2 pm. We have also investigated the polarization sensitivity of the device. Our results show that the presented interrogator is stable to temperature and polarization change and can be used in industrial-grade applications. Thanks to the Hadamard scan method one can improve SNR of the measured signal up to 9 dB and increase the wavelength fit resolution for a weak input signal.

Finally, in the second part of Chapter 8 we used the presented interrogator for strain and temperature measurements of real FBG sensors and multimode FBGs. We used the multiple channel feature and measured the response from 4 FBGs simultaneously. We investigated the temperature response of silica FBGs embedded in 4 different polymer 3D-printed structures. We showed that one can increase the thermal sensitivity up to 10-12 times by embedding FBGs into polymer 3D printed structures. Humidity sensing is also possible with such kind of sensors. We also investigated polarization properties and strain response of few-mode and multimode polymer FBGs. We showed that the strain response is different for peaks with different polarization reflected from the same FBG and needs further investigation. By using the new interrogator we measured the strain response of a few-mode and a highly multimode FBG in a polymer fiber.

9.1 Outlook

The presented interrogator has demonstrated high performance during numerous experiments. It has successfully passed all the tests, which are performed for commercially available interrogators at Ibsen Photonics. The device has also been presented at conferences and symposiums (POF2015, TI symposium), arousing the interest of visitors, and will be presented in April 2017 at the biggest conference in the optical fiber sensing field – OFS 25 in South Korea. The scanning speed is relatively slow, but can be improved in the future. This will make the presented interrogator very attractive for potential customers as a final product.

Acronyms

AOI – angle of Incidence

AOTF - Acousto-Optic Tunable Filter

AR – Anti Reflection

ASE - Amplified Spontaneous Emission

CCD – Charge-Coupled Device

COG – center of Gravity

CTE – Coefficient of Thermal Expansion

CW – Constant Wavelength

DGA – Dynamic Gate Algorithm

DMD – Digital Micromirror Device

DLP – Digital Light Processing

EDIA – Extended Diffraction Image Analysis

EDF - Erbium-Doped Fiber

EDFA - Erbium-Doped Fiber Amplifier

FBG – Fiber Bragg Grating

FFT – Fast Fourier Transform

FPF - Fabry–Perot Filter

FWHM – Full Width on Half Maximum

HOM – High Order Modes

LPO – Linear Phase Operator

MMF – Multi Mode Fiber

MOEMS – Micro-Opto-Electromechanical System

mPOF –Microstructured polymer optical Fiber

MZI - Mach-Zehnder Interferometer

OSA – Optical Spectrum Analyzer

PC –Polycarbonate

PDL – Polarization Dependable Loss

PDW – Polarization Dependable Wavelength shift

PM – Phase-Mask

PMMA - Polymethyl Methacrylate

POF – Polymer Optical Fiber

POFBG – Polymer Optical Fiber Bragg Grating

PRNU – Photo Response non-Uniformity

PZT –Piezo Transducer

RF – Radio Frequency

RH – Relative Humidity

SMF- Single Mode Fiber

SNR - Signal-to-Noise Ratio

UV – UltraViolet

WFR – Wavelength Fit Resolution

References

1. A. D. Kersey, M. A. Davis, H. J. Patrick, M. LeBlanc, K. P. Koo, C. G. Askins, M. A. Putnam, and F. J. Friebele, "Fiber grating sensors," J. Lightwave Technol. 15, 1442–1463 (1997).
2. K. T. V. Grattan and B. T. Meggitt, eds., "Optical Fiber Sensor Technology," Vol. 2, Chapman & Hall, London, (1998).
3. D. J. Webb and K. Kalli, "Polymer fiber Bragg gratings in Fiber Bragg Grating Sensors: Recent Advancements, Industrial Applications and Market Exploitation," A. Cusano, A. Cutolo, and J. Albert Eds. Oak Park, IL: Bentham eBooks, pp. 292–312 (2011).
4. H. Dobb, K. Carroll, D. J. Webb, K. Kalli, M. Komodromos, C. Themistos, G. D. Peng, A. Argyros, M. C. J. Large, M. A. van Eijkelenborg, Q. Fang, and I. W. Boyd, "Grating based devices in polymer optical fibre," Proc. SPIE 618901 (2006).
5. K. O. Hill, Y. Fujii, D. C. Johnson, B. S. Kawasaki, "Photosensitivity in optical fiber waveguides: Application to reflection filter fabrication," Appl. Phys. Lett., 32(10): 647-9 (1978).
6. G. Meltz, W. W. Morey, W. H. Glenn, "Formation of Bragg gratings in optical fibers by a transverse holographic method," Opt. Lett., 14(15): 823-5 (1989).
7. K. O. Hill, B. Malo, F. Bilodeau, D. C. Johnson, J. Albert, "Bragg gratings fabricated in monomode photosensitive optical fiber by UV exposure through a phase mask," Appl. Phys. Lett., 62(10) (1993).
8. P. J. Lemaire, R. M. Atkins, V. Mizrahi, W. A. Reed, "High pressure H2 loading as a technique for achieving ultrahigh UV photosensitivity and thermal sensitivity in GeO2 doped optical fibres," Electron. Lett., 29(13): 1191-3 (1993).

9. G. Meltz , W. W. Morey, “Bragg grating formation and germanosilicate fiber photosensitivity,” International Workshop on Photoinduced Self-Organization Effects in Optical Fiber, 185 (1991).

10. G. W. Yoffe, Peter A. Krug, F. Ouellette, and D. A. Thorncraft, ”Passive temperature compensating package for optical fiber graqtings,” Applied Optics, Vol. 34, Issue 30, pp. 6859-6861 (1995).

11. M. G. Xu, J. L. Archambault, L. Reekie, J. P. Dakin, “Thermally-compensated bending gauge using surface-mounted fiber gratings,” International Journal of Optoelectronics, Vol. 9, Issue 3, pp. 281-283 (1994).

12. M. G. Xu et al., “Temperature-independent strain sensor using a chirped Bragg grating in a tapered optical fiber,” Electronics Letters, Vol. 31, pp. 823-825 (1995).

13. T. Huang, S. Fu, C. Ke, P. P. Shum, and D. Liu, “Characterization of fiber Bragg grating inscribed in few-mode silica-germanate fiber,” IEEE Photon. Technol. Lett. 26(19), 1908-1911 (2014).

14. D. Song et al., “A simultaneous strain and temperature sensing module based on FBG-in-SMS,” Measurement Sciens and Technology, Vol. 25 (2014).

15. M. G. Xu, J. L. Archambault, L. Reekie, J. P. Dakin, “Discrimination between strain and temperature effects using dual-wavelength fibre grating sensors,” Electronics Letters, Vol. 30, Issue 13, pp. 1085-7 (1994).

16. J. Albert, L.-Y. Shao and C. Caucheteur, “Tilted fiber Bragg grating sensors,” Laser Photonics Rev. 7(1), 83-108 (2013).

17. M. G. Xu et al., “Optical in-fibre grating high pressure sensor,” Electronics Letters, Vol. 29, pp. 389-399 (1993).

18. S. M. Melle, K. Liu and R. M. Measures, “A passive wavelength demodulation system for guided-wave Bragg grating sensors,” IEEE Photonics Technol. Lett., Vol. 4, Issue 5, pp. 516–518 (1992).

19. M. A. Davis and A. D. Kersey, “All-fibre Bragg grating strain-sensor demodulation technique using a wavelength division coupler,” Electronics Lett., 30, 1, pp. 75–77 (1994).

20. S. C. Kang, H. Yoon, S. B. Lee, S. S. Choi, and B. Lee, “Real-time measurement for static and dynamic strain using a fiber Bragg grating

and the ASE profile of EDFA," Proc. 13th Int. Conf. Optical Fiber Sensors (OFS-13), Kyongju, Korea, SPIE, 3746, pp. 530–533 (1999).

21. A. D. Kersey, T. A. Berkoff, and W. W. Morey, "Multiplexed fiber Bragg grating strain-sensor system with a fiber Fabry–Perot wavelength filter," Optics Lett., 18, pp. 1370–1372 (1993).

22. G. A. Ball, W. W. Morey, and P. K. Cheo, "Fiber laser source=analyzer for Bragg grating sensor array interrogation," J. Lightwave Technol., 12, pp. 700–703 (1994).

23. H. Geiger, M. G. Xu, N. C. Eaton, and J. P. Dakin, "Electronic tracking system for multiplexed fibre grating sensors," Electronics Lett., 32, pp. 1006– 1007 (1995).

24. A. D. Kersey, T. A. Berkoff, and W. W. Morey, "High-resolution fibre-grating based strain sensor with interferometric wavelength-shift detection," Electronics Lett., 28, 3, pp. 236–238 (1992).

25. R. S. Weis, A. D. Kersey, and T. A. Berkoff, "A four-element fiber grating sensor array with phase-sensitive detection," IEEE Photonics Technol. Lett., 6, 12, pp. 1469–1472, (1994).

26. M. A. Putnam, M. L. Dennis, J. U. Kang, T.-E. Tsai, I. N. Duling, and I. E. J. Friebele, "Sensor grating array demodulation using a passively modelocked fiber laser," Technical Digest Optical Fiber Commun. Conf., Dallas, TX, Paper WJ4, pp. 156–157 (1997).

27. G. D. Peng, Z. Xiong, and P. L. Chu, "Photosensitivity and gratings in dye-doped polymer optical fibers," Optical Fiber Technology, vol. 5, pp. 242-251 (1999).

28. H. Y. Liu, G. D. Peng, and P. L. Chu, "Polymer fiber Bragg gratings with 28-dB transmission rejection," Photonics Technology Letters, Vol. 14, pp. 935-937 (2002).

29. H. Dobb, D. J. Webb, K. Kalli, A. Argyros, M. C. J. Large, and M. A. van Eijkelenborg, "Continuous wave ultraviolet light-induced fiber Bragg gratings in few- and single-mode microstructured polymer optical fibers," Optics Letters, vol. 30, pp. 3296-3298 (2005).

30. K. Peters, "Polymer optical fiber sensors—a review," Smart Mater. Struct. 20(1), 013002 (2011).

31. H. Y. Liu, G. D. Peng, and P. L. Chu, "Thermal tuning of polymer optical fiber Bragg gratings," IEEE Photonics Technology Letters, vol. 13, pp. 824-826 (2001).

32. N. G. Harbach, "Fiber bragg gratings in polymer optical fibers," PhD, EPFL, Lausanne (2008).

33. W. Yuan, L. Khan, D. J. Webb, K. Kalli, H. K. Rasmussen, A. Stefani, et al., "Humidity insensitive TOPAS polymer fiber Bragg grating sensor," Optics Express, vol. 19, pp. 19731-19739 (2011).

34. A. Fasano et al, "Production and characterization of polycarbonate microstructured polymer optical fibre Bragg grating sensor," Proceedings of the 24th International Conference on Plastic Optical Fibers, pp. 64-67 (2015).

35. G. W. Kaye and T. H. Laby, "Tables of physical and chemical constants," 16th ed.: Longmann (1995).

36. J. Brandrup, "Polymer Handbook" vol. 1&2: Wiley (1999).

37. K. Krebber, P. Lenke, S. Liehr, N. Noether, M. Wendt, and A. Wosniok, "Distributed fiber optic sensors embedded in technical textiles for structural health monitoring," in Fourth European Workshop on Optical Fibre Sensors, J. L. Santos, B. Culshaw, J. M. López-Higuera, and W. N. MacPherson, eds., Vol. 7653, p. 76530A–76530A–12 (2010).

38. A. Stefani, S. Andresen, W. Yuan, N. Herholdt-Rasmussen, and O. Bang, "High Sensitivity Polymer Optical Fiber-Bragg-Grating-Based Accelerometer," IEEE Photonics Technology Letters, vol. 24, pp. 763-765 (2012).

39. M. Aressy, "Manufacturing optimisation and mechanical properties of polymer optical fibre," MPhil, Birmingham University, Birmingham (2006).

40. P. Stajanca, O. Cetinkaya, M. Schukar, P. Mergo, D. J. Webb, K. Krebber, "Molecular alignment relaxation in polymer optical fibers for sensing applications," Optical Fiber Technology 28 (2016).

41. C. R. Kurkjan, J. T. Krause, and M. J. Matthewson, "Strength and Fatigue of Silica Optical Fibers," Journal of Lightwave Technology, vol. 7, pp. 1360-1370 (1989).

42. A. Abang and D. J. Webb, "Effects of annealing, pre-tension and mounting on the hysteresis of polymer strain sensors," Meas. Sci. Technol. 25(1), 015102 (2014).

43. S. Yuan, A. Stefani, M. Bache, T. Jacobsen, B. Rose, N. Herholdt-Rasmussen, et al., "Improved thermal and strain performance of annealed polymer optical fiber Bragg gratings," Optics Communications, vol. 284, pp. 176-182 (2011).

44. G. Woyessa et al, "Temperature insensitive hysteresis free highly sensitive polymer optical fiber Bragg grating humidity sensor", Optics Express (submitted November 2015) Optics Express Vol. 24, No 2, pp. 1206-1213 (2016).

45. G. Woyessa, A. Fasano, A. Stefani, C. Markos, K. Nielsen, H. K. Rasmussen, O. Bang, "Single mode step-index polymer optical fiber for humidity insensitive high temperature fiber Bragg grating sensors," Optical Express; Vol. 24, No. 2, pp 1253-60 (2016).

46. D. Sáez-Rodríguez, K. Nielsen, H. K. Rasmussen, O. Bang, and D. J. Webb, "Highly photosensitive polymethyl methacrylate microstructured polymer optical fiber with doped core," Opt. Lett. 38(19), 3769–72 (2013).

47. K. E. Carroll, C. Zhang, D. J. Webb, K. Kalli, A. Argyros, and M. C. Large, "Thermal response of Bragg gratings in PMMA microstructured optical fibers," Opt. Express 15(14), 8844–8850 (2007).

48. A. Fasano, G. Woyessa, P. Stajanca, et al, "Fabrication and characterization of polycarbonate microstructured polymer optical fibers for high-temperature-resistant fiber Bragg grating strain sensors", Optics Material Express, Vol. 6, Issue 2, pp. 649-659 (2016).

49. G. Meltz, W. W. Money and W. H. Glenn, "Formation of Bragg gratings in optical fibres by a transverse holographic method," Optics Letters, Vol. 14, pp. 823-825 (1989).

50. Z. Xiong, G. D. Peng, B. Wu, P. L. Chu, "Highly tunable Bragg gratings in single-mode polymer optical fibers," IEEE Photon Technol Lett 11 (1999).

51. I.-L. Bundalo, K. Nielsen, C. Markos, and O. Bang, "Bragg grating writing in PMMA microstructured polymer optical fibers in less than 7 minutes," Opt. Express 22(5), 5270–6 (2014).

52. T. Geernaert et al., “Point-by-point fiber Bragg grating inscription in free-standing step-index and photonic crystal fibers using near- IR femtosecond laser,” Opt. Lett., vol. 35, no. 10, pp. 1647–1649 (2010).

53. A. Lacraz et al., 'Femtosecond laser inscribed Bragg gratings in low loss CYTOP polymer optical fibre' IEEE Photonics Technology Letters, Vol. 27, NO. 7, p693-696 (2015).

54. D. Ganziy, O. Jespersen. G. Woyessa, B. Rose, O. Bang, “Dynamic gate algorithm for multimode fiber Bragg grating sensor systems”, Applied Optics 54(18), 5657-5661 (2015).

55. C. G. Atkins, M. A. Putnam, and E. J. Friebele, “Instrumentation for interrogating many-element fiber Bragg grating arrays,” Proc. SPIE 2444, 257–267 (1995).

56. S. D. Dyer, P. A. Williams, R. J. Espejo, J. D. Kofler, and S. M. Etzel, “Fundamental limits in fiber Bragg grating peak wavelength measurements,” (Invited Paper) Proc. SPIE 5855, 88–93 (2005).

57. T. Zeh, H. Schweiser, A. Meixner, A. Purde, and A. W. Koch “Enhancement of detection accuracy of fiber Bragg grating sensors,” Proc. SPIE 5502, 540–543 (2004).

58. M. J. Schmid and M. S. Muller, “Measuring Bragg gratings in multimode optical fibers,” Opt. Express 23, 8087–8094 (2015).

59. D. Ganziy, B. Rose, O Bang, “Performance of low-cost few-mode FBG sensor systems: polarization sensitivity and linearity of temperature and strain response”, Applied Optics 55(23), 6156-6161 (2016).

60. W. Zhao and R. O. Claus, “Optical fiber grating sensors in multimode fibers,” Smart Mater. Struct. 9, 212–214 (2000).

61. C. Lu and Y. Cui, “Fiber Bragg grating spectra in multimode optical fibers,” J. Lightwave Technol. 24, 4828–4837 (2006).

62. A. Sun and Z. Wu, “Multimode interference in single mode-multimode FBG for simultaneous measurement of strain and bending,” IEEE Sens. J. 15, 3390–3394 (2015).

63. R. H. Stolen, V. Ramaswamy, P. Kaiser, and W. Pleibel, “Linear polarization in birefringent single-mode fibers,” Appl. Phys. Lett. 33, 699–701 (1978).

64. A. M. Vengsarkar, Q. Zhong, D. Inniss, W. A. Reed, P. J. Lemaire, and S. G. Kosinski, “Birefringence reduction in side-written photoinduced

fiber devices by a dual-exposure method," Opt. Lett. 19, 1260–1262 (1994).

65. K. Dossou, S. LaRochelle, and M. Fontaine, "Numerical analysis of the contribution of the transverse asymmetry in the photo-induced index change profile to the birefringence of optical fiber," J. Lightwave Technol. 20, 1463–1470 (2002).

66. X. C. Hu, D. Saez-Rodriguez, C. Marques, O. Bang, D. J. Webb, P. Megret, and C. Caucheteur, "Polarization effects in polymer FBGs: study and use for transverse force sensing," Opt. Express 23, 4581–4590 (2015).

67. B. E. A. Saleh and M. C. Teich, "Fiber optics," in Fundamentals of Photonics, 2nd ed., Wiley, pp. 333–334 (2014).

68. A. W. Snyder and J. D. Love, "Waveguides with exact solutions," in Optical Waveguide Theory, 1st ed. Springer, pp. 252–255 (1983).

69. C. Winkler, J. D. Love, and A. K. Ghatak, "Loss calculations in bent multimode optical waveguides," Opt. Quantum Electron. 11, 173–183 (1979).

70. C. K. Asawa and H. F. Taylor, "Propagation of light trapped within a set of lowest-order modes of graded-index multimode fiber undergoing bending," Appl. Opt. 39, 2029–2037 (2000).

71. S. Acco, Y. Sintov, Y. Glick, O. Katz, Y. Nafcha, and R. Lavi, "Bendloss control of multi-mode fiber power amplifiers producing singlemode operation," in Advanced Solid-State Photonics, Technical Digest, Optical Society of America, p. 565 (2005).

72. A. Stefani, S. Andresen, W. Yuan, and O. Bang, "Dynamic characterization of polymer optical fibers," IEEE Sens. J. 12, 3047–3053 (2012).

73. J. Li, Q. P. Yang, B. E. Jones, and P. R. Jackson, "Strain and temperature sensors using multimode optical fiber Bragg gratings and correlation signal processing," IEEE Trans. Instrum. Meas. 51, 622–627 (2002).

74. K. Chance, T. P. Kurosu, C. E. Sioris, "Undersampling correction for array detector-based satellite spectrometers," Applied Optics Vol. 44 No. 7 (2005)

75. K. W. Kho, P. R. Stoddart, G. Rosman, M. Harris, and A. Mazzolini, “Reduction of polarization-induced artifacts in grating-based spectrometers,” Appl. Opt. 44, 6123–6130 (2005).

76. M. R. Webb and G. M. Hieftje, “Improved Monochromatic Imaging Spectrometer,” Applied Spectroscopy, Vol. 60, pp 57-60 (2006).

77. S. Remund, A. Bossen, L. Wang, L. Zhang, B. Považay, C. Meier, “Fiber- optically integrated cost-effective spectrometer for optical coherence tomography,” Proc. SPIE 9129, Biophotonics: Photonic Solutions for Better Health Care IV (2014).

78. Texas Instruments White Paper, “Texas Instruments DLP® Technology for Spectroscopy,” DLPA048 (2014).

79. Z. Zhihaia, M. Xiangxia, G. Yuanjuna, W. Weia, “A Novel MOEMS NIR Spectrometer,” International Conference on Optics in Precision Engineering and Nanotechnology (2011).

80. Texas Instruments Data Sheet “DLP2010NIR 0.2 WVGA Near-Infrared DMD” (2015)

81. V. Vasile, D. Damian, F. Coltuc, C. Garoi, C. Udrea, “Implementation of Hadamard Spectroscopy using MOEMS as a coded aperture,” Proc. of SPIE Vol. 9258 (2015).

82. D. J. Heath, M. Feinaeugle, J. A. Grant-Jacob, B. Mills, R. W. Eason, "Dynamic spatial pulse shaping via a digital micromirror device for patterned laser-induced forward transfer of solid polymer films". Optical Materials Express (2015).

83. Texas Instruments White Paper, “Introduction to Digital Micromirror Device (DMD) Technology,” DLPA008A (2013).

84. Texas Instruments manual, “DLP NIRscan Nano EVM User’s Guide,” DLPU030F (2016).

85. B. Rose, M. Rasmussen, N. Herholdt-Rasmussen, O. Jespersen, “Programmable Spectroscopy Enabled by DLP,” Proc. of SPIE Vol. 9376 (2015).

86. M. Harwit, and N. J. A. Sloane, “Hadamard transform optics,” Academic Press, USA, New York, chapter 2 (1979).

87. R. E. A. C. Paley, "On orthogonal matrices". Journal of Mathematics and Physics. 12: 311–320 (1933).

88. D. Ganziy, B. Rose, O Bang, “Compact multichannel high resolution MEMS based interrogator for FBG sensing”, Submitted to Applied Optics (2017).

89. J. Yue, J. Han, Y. Zhang, and L. Bai, “Denoising analysis of Hadamard transform spectrometry,” Optics Letters, Vol. 39 (2014).

90. M. Zubel, K. Sugden, D. J. Webb, D. Saez-Rodriguez, K. Nielsen and O. Bang, “Embedding silica and polymer fibre Bragg gratings (FBG) in plastic 3D-printed sensing patches,” Micro-Structured and Specialty Optical Fibres IV, Proc. of SPIE Vol. 9886 (2016).

DENIS GANZIY was born in Ukraine in 1985. He received the B.Sc. and M.Sc. degree in Applied Mathematics and Physics from Moscow Institute of Physics and Technology, Russia, in 2008 and 2010. He is currently pursuing the Ph.D. degree in Photonics from Technical University of Denmark.